DISSERTATION

DEVELOPMENT OF FLUIDIC DEVICES TO FACILITATE MORE ACCESSIBLE MONITORING OF HUMAN HEALTH

Submitted by

Amanda E. Cherwin

School of Biomedical Engineering

In partial fulfillment of the requirements

For the Degree of Doctor of Philosophy

Colorado State University

Fort Collins, Colorado

Summer 2024

Doctoral Committee:

Advisor: Charles S. Henry
Co-Advisor: Stuart A. Tobet

Christopher Snow
Zaid Abdo

ABSTRACT

DEVELOPMENT OF FLUIDIC DEVICES TO FACILITATE MORE ACCESSIBLE MONITORING OF HUMAN HEALTH

In December of 2023, the World Health Organization (WHO) Director-General Tedros Adhanom Ghebreyesus outlined the 'Five P's' of global health priorities: Promoting health, Providing health, Protecting health, Powering health, and Performing for health. Despite the mantra of 'prevention is better than cure,' many countries still prioritize treating the sick over proactive health promotion, leading to inadequate prevention of non-communicable diseases (NCDs). Access to healthcare services poses a significant barrier to early recognition and treatment of health issues, particularly in low-income communities. To address these challenges, harnessing the power of science and technology becomes imperative.

Powering health involves leveraging scientific research and collaboration to understand disease mechanisms better. Physiologically relevant models, such as microfluidic systems, offer insights into disease progression. Microfluidics, especially when combined with 2D and 3D culture systems, enhances functionality by mimicking physiological conditions. These devices provide cost-effective solutions for diagnostic challenges, bridging the gap between in vitro and in vivo studies.

Protecting health requires a deeper understanding of organ systems. Chapter 2 examines a microfluidic model of the gut, an organ that plays a critical role in maintaining overall health. Two devices are discussed, an organotypic device for maintaining ex vivo gut tissue explants, and an electrochemical sensor module for monitoring relevant molecules such as oxygen or hydrogen

peroxide within the tissue media. Dysbiosis in the gut microbiome has been linked to various pathologies, emphasizing the need for accurate models for studying gut barrier integrity. Ex vivo models using microfluidic devices offer promising avenues for studying disease mechanisms. The devices described in Chapter 2 serve as an effective model of the intestinal barrier that can be closely monitored in real-time.

Providing health involves making effective healthcare solutions universally accessible. Point-of-care (POC) diagnostics, facilitated by microfluidics, enable rapid and cost-effective disease detection. Capillary-driven flow microfluidic devices enhance accessibility by eliminating the need for bulky external pumps, making POC testing feasible even in resource-limited settings. Combining the concepts of Powering and Providing health leads to the development of innovative diagnostic devices. Capillary-driven flow microfluidics enables the development of portable devices for diagnosing conditions from viscous sample matrices like blood and saliva. These devices offer less invasive and more accessible alternatives to traditional diagnostic methods, potentially revolutionizing healthcare delivery.

Chapter 3 describes a capillary flow device used to quantify levels of two salivary biomarkers (Galectin-3 and S100A7) correlated to Heart Failure (HF) outcomes. This rapid, noninvasive, accessible POC test can drastically improve the quality of life for HF patients, particularly in rural and resource-limited areas. Using an electrochemical detection method, we demonstrate successful multiplexed detection of both biomarkers in spiked buffer solutions.

Chapter 4 focuses on microfluidic devices probing rheological properties of whole blood related to Sickle Cell Disease (SCD) and clotting using capillary flow. For the SCD device, our goal was to develop a low-cost Point-of-Care (POC) multiplexed device for rapid and accurate identification of SCD phenotypes using three key reagents tied to altered sickle cell blood

rheology: calcium chloride, sodium metabisulfite, and adenosine diphosphate. We developed an integrated device where whole blood reacts with reagent pads, enabling rapid assessment of a patient's SCD phenotype to inform appropriate treatment. We also introduced the Paper-based Clotting Analysis Test (PCAT) for efficient, low-cost analysis of primary hemostasis. Current methods for monitoring hemostasis are expensive and slow. Our capillary flow device uses whole blood moving at high flow rates for sustained durations to induce thrombus formation.

This dissertation bridges the gap between effective health monitoring and accessibility through fluidic devices using either pump-driven or capillary-driven flow. Chapters detail the development of microfluidic systems for monitoring intestinal barrier function, detecting biomarkers in saliva for Heart Failure prognosis, and processing blood samples for Sickle Cell Disease phenotyping and clotting analysis. Ultimately, these devices hold the potential to transform healthcare management, particularly in underserved communities.

ACKNOWLEDGEMENTS

First, I would like to thank my advisors, Dr. Chuck Henry and Dr. Stu Tobet. I spent most of my time with Dr. Henry, and his patience and guidance over the last five years have shaped me into the researcher and person I am today. My advisors taught me valuable lessons in all aspects of life and as a scientist, and I will carry the lessons I learned from them with me for the rest of my life. I am grateful for the examples they set in building a strong team, and leaning on the expertise of your peers to bolster the quality of work you can produce. I would also like to thank my committee members, Dr. Chris Snow and Dr. Zaid Abdo, for always challenging me to raise the caliber of my work and ask deeper, more meaningful questions to guide my research.

Next, I would like to thank my fellow group members in the Henry and Tobet Groups for being pillars of support and friendship for me. Their creative ideas, hilarious quotes, and daily acts of kindness meant more to mean than I can properly express. I would especially like to thank Dr. Thaísa Baldo for being an unbelievably brilliant and strong woman that I look up to and for teaching me how to always find something to smile about on even the hardest days.

I am grateful to Applied Medical Resources Corporation for their support of the gut microfluidic device project. Nick, Darci, and Andrew helped support the design and development of the device, as well as providing me with the injection molded devices that were used for our tissue experiments.

I also need to thank all my friends and family members for their unwavering support throughout this experience. To my mom, Margie, who has always been my loudest cheerleader and the only person who didn't call me crazy for wanting to get a PhD, know that every success of mine is a reflection and a result of the love and support you give me. To my dad, Randy, who

definitely called me crazy for wanting to get a PhD, your weekly phone calls were a welcome distraction when I was struggling and feeling overwhelmed. To my siblings Stephanie, Trevor, and Max, I'm grateful for every meme, snapchat, text, or phone call that helped me feel like home wasn't so far away after all. To the North Gate Disc Golf Club, I can't thank you enough for always reminding me to take a break and soak up some sunshine, all the while encouraging me to chase my dreams. Finally, I can't forget to acknowledge my cats, Thor and Loki, for being the best coworkers when I was working from home and for the endless love you give to everyone you meet.

TABLE OF CONTENTS

Chapter 1: Introduction

In December of 2023 the World Health Organization (WHO) Director-General Tedros Adhanom Ghebreyesus gave a keynote address on global health priorities, where he outlined the "Five P's" of global health for the coming years: **P**romoting health, **P**roviding health, **P**rotecting health, **P**owering health, and **P**erforming for health.[1] He reminded us of a mantra from Hippocrates, that "prevention is better than cure." Obvious as that statement may seem, we are still failing to effectively prevent many non-communicable diseases (NCDs) even today. We need to actively work to shift the paradigm of where health "starts." Health starts in homes, in schools, and in workplaces; it does not start at the clinic or the hospital when one is already sick or hurting.

Too many countries focus their approach to health on treating the sick rather than proactively promoting health and preventing disease. Unfortunately, treatment can only go so far, and is highly dependent on when a diagnosis occurs relative to the progression of the disease. Early recognition of health issues leads to better clinical outcomes[2, 3] and allows patients to have a higher quality of life. One of the largest barriers to early recognition is access to healthcare and essential health services—this is where the priority to **P**rovide health comes in. Most gold standard methods for diagnosis and prognosis of disease require expensive equipment, centralized facilities, and trained personnel; this is often cost-prohibitive in lower income and resource-limited communities.[4-6]

1.1 Fluidic Devices for Biomedical Applications

Powering health means harnessing the power of science, research and development, and collaborations to maximize the impact toward improving health. To ensure that the treatment approach is truly aiming to correct the root of the problem and not just treat the symptoms of it, we must first understand how the disease or condition is affecting the patient's body. Scientists

have worked extensively to create physiologically-relevant models of numerous NCDs, using a variety of model systems from cultured cells, to tissues, to full organisms.[7-9] Static culture systems (i.e., in vitro) experience completely different environmental cues compared to natural tissues within a complex three-dimensional (3D) extracellular matrix (ECM, i.e., in vivo), and this significantly affects how the cells grow and function.[10]

Microfluidics is the study and manipulation of fluids in small volumes (10^{-9}-10^{-18} L) in channels ranging from tens to hundreds of micrometers in size.[11, 12] Manipulation of fluids at this scale provides higher control over spatiotemporal dynamics compared to larger systems,[11, 13] and requires considerably less volumes of samples and reagents (reducing costs). The incorporation of microfluidics with 2D culture systems greatly increases in vitro systems' functionality by allowing for the inclusion of physical forces such as fluid shear stress, cyclic strain, and mechanical compression.[14] Fluidic and microfluidic devices have greatly expanded the toolbox for analytical measurements in countless fields. These devices have been used broadly for applications[11] including single molecule detection,[15] immunoassays,[16] environmental analysis,[17] and organ-on-chip (OOC) devices.[14] Microscale chemistry allows for better sensitivity and faster operations while requiring a smaller sample—thereby lowering sample and reagent costs. Ex vivo methods, such as incorporating intact tissue explants within a microfluidic device, bridge the gap between simple, easy to maintain in vitro systems and highly complex in vivo systems. This allows for more accurate study of the mechanisms underlying disease states than current in vitro models, without the challenges inherent to in vivo studies.

When considering how flow is generated within these fluidic devices, the first decision is either active (i.e., mechanical, pump-driven) or passive (non-mechanical) flow control.[11] I have worked to develop devices with both systems and have gained experience with advantages and

disadvantages of each. The most common method for active pumping, and the one I used, is a syringe pump. This type of pump dispenses an accurate volume of liquid by pushing on the syringe's plunger, using a stepper motor to drive the nut connected to the piece that pushes the syringe.[11] This type of pump is very accurate and allows the operator to control the exact flow rate as well as when flow starts and stops, but the equipment itself is bulky and expensive relative to passive pumping systems.[11, 18] I also worked to develop microfluidic devices that use capillary action to drive flow without the need for external pumping equipment. Capillary flow drives fluid through the channels based on surface tension, geometry, and wetting properties of the channel in addition to the viscosity and other properties of the fluid.[5, 11, 19] Capillary flow is continuous once initiated, and will continue until the channel is filled, but this type of system is nearly impossible to designate an exact flow rate at which your fluid will move through the device,[11] a challenge I had to address in the development of some of my devices.

1.2 Using Microfluidics to Generate a Functional Model of the Gut Barrier

When considering how to proactively **P**rotect health, we must consider which organ(s) play a pivotal role in maintenance of overall health. With recent observations of its involvement in disease progression and human health,[20-24] the importance of the intestinal barrier has become increasingly obvious. To ensure survival, the gut must maintain a barrier that retains the ability to digest and absorb nutrients while protecting the body from harmful substances.[21, 22] Fundamentally, the intestines act to absorb nutrients and other compounds from our diet to aid in survival;[21, 25, 26] however, the gut also plays a critical defensive role as a barrier against harmful compounds as well.[27-29] The gut is unique in its three-dimensional (3D) structure as well as its diverse cellular makeup.[30, 31] Its population of epithelial, neuronal, immune, stem, and other cell types facilitate numerous different functions. This cellular diversity leads to complex biochemistry in terms of

products that can be produced by these cells;[32] these products can lead to downstream effects in a variety of other organ systems such as within the brain and the lungs.[33-35]

The microbial population that exists within the gut, the microbiome, is a diverse population of bacterial species that plays an essential role in how the gut functions;[36] the microbiome even varies in composition between the different segments of the gut. A dysbiosis or imbalance in the microbiome has been directly implicated in many pathologies, including obesity,[37, 38] type 2 diabetes,[39] Irritable Bowel Disease (IBD),[40-44] rheumatoid arthritis,[45] Parkinson's Disease,[34, 46] multiple sclerosis,[47] and colorectal cancer,[38] among others. The microbiome and metabolites generated by it are integral to the inter-organ communications that maintain homeostasis within the body.

It has become even clearer in recent decades that there exists a need for a more comprehensive understanding of how the gut functions, and how poor gut health can contribute to worsening systemic health. Dysfunction of the epithelial monolayer linked by tight junctions can lead to alterations in paracellular permeability that may be called a "leaky gut."[21] Leaky gut can precede and even predict the onset of Crohn's disease, and it also contributes to progressive tissue damage that can culminate in clinical IBD.[40-44] Additionally, disruption of the gut barrier has been associated with the pathogenesis of conditions such as autoimmune diseases such as celiac disease,[21] neurodegenerative disorders such as Lewy body dementias like Alzheimer's and Parkinson's Disease,[34, 48, 49] and neurodevelopment disorders such as autism spectrum disorder.[50] There is a need for an accurate model of the gut that maintains the complexity of intestinal anatomy, microenvironment, and barrier to better understand how alterations in barrier integrity may contribute to disease states.

Generation of an intestinal model that maintains the complexity of intestinal anatomy, microenvironment, and barrier is necessary to better understand how alterations in barrier integrity may contribute to disease states. I have worked to develop an ex vivo model using intestinal explants within a microfluidic device to serve as an effective model of the intestines. This project used pump-driven flow to precisely control the delivery of media to the tissue at specified flow rates. The device has demonstrated success in early experiments: the tissue explant maintains native cell populations, and using microfluidics allows for control over the microenvironment within the device. Long-term goals for this device include using patient tissue explants to guide a customized, highly effective treatment approach.

1.3 Point-of-Care Microfluidic Devices for Viscous Sample Matrices

Combining the ideas of **P**owering and **P**roviding health means making more effective and efficient means of improving global health more universally accessible. "Most global health challenges are not challenges of science or medicine. They are challenges of inequality and inequity: poverty, marginalization, disadvantage, remoteness."[1] A common approach to diagnostics in recent years[51-54] is the development of devices that can be deployed at the Point-of-Care (POC). POC tests can be performed at or near the site of patient care, rather than in a central laboratory, thus allowing for more rapid test results. Although the development of POC testing seems commonly aimed for remote settings and communicable diseases, developed countries would benefit from portable diagnostics for NCDs as well. Faster diagnosis can lead to early treatment of an illness, thus decreasing the morbidity rate and treatment costs.[55] Additionally, portable and/or POC diagnostics can give patients the ability to self-diagnose, increasing preventative and personalized medicine and contributing to improved global health care.[56] Many POC testing devices can be made from relatively inexpensive materials,[5, 19, 57, 58] considerably

reducing the overall cost to the patient. While most POC devices are cheap, portable, and easy-to-use, some suffer from a lack of sensitivity and an inability to handle complex biological samples (e.g., blood or saliva).[3, 59, 60]

Microfluidics has played a key role in the development of POC diagnostics by requiring smaller sample volumes and combining multiple sample-processing steps into a single device.[61] Capillary-driven flow microfluidics has further revolutionized POC device development because it allows for movement of fluids within capillaries or microchannels without requiring an expensive, bulky external pump,[19, 61] greatly increasing the accessibility of these tests while also reducing costs. In many cases, POC devices using capillary-driven flow provide results within minutes,[57] allowing diagnostic decisions to be made at the clinic the same day the patient comes in for a check-up.

I have worked on the development of several capillary-driven flow microfluidic devices for uses in diagnosis and prognosis of disease states using viscous sample matrices such as blood and saliva. These devices are fabricated from low-cost materials including double-sided adhesive (DSA), transparency film, and paper. A capillary-driven microfluidic device that I have worked to develop uses a less invasive sample to collect: saliva. This device uses modified electrodes to detect two distinct biomarkers associated with Heart Failure (HF) in a patient's saliva. According to the Centers for Disease Control and Prevention (CDC), in 2018 HF was cited on 13.4% of death certificates in the United States. HF continues to be a growing problem, particularly in rural and underrepresented communities where current HF diagnostic and prognostic methods are less accessible due to cost and resource demands.[62-64] The current gold standard diagnostic for HF is a blood-based test to detect the biomarker B-type natriuretic peptide (BNP), a hormone secreted from cardiac ventricular myocytes.[65] The BNP test is a fluorescent immunoassay that

quantitatively measures BNP levels in blood; while this assay has high sensitivity and specificity, it requires sophisticated equipment and trained personnel to perform properly.[66, 67] Additionally, the results from a single BNP test is less meaningful in providing information about HF risk and likelihood of an impending cardiac event than tracking and comparing a patient's BNP trajectory over time.[68] This means that a patient has to repeatedly travel to a facility where this test can take place and have blood drawn several times over the course of months or years before a clear picture of their risk of HF can be understood. This inadequacy has led researchers to investigate alternative biomarkers related to HF. Several biomarkers have been identified in serum[69] of HF patients, and many have later been confirmed to be present in their saliva as well.[70-72] Galectin-3 (Gal-3) and S100A7 are novel salivary HF biomarkers for which our collaborators in the Punyadeera Group of Griffith University in Australia quantified in saliva of healthy patients as well as those experiencing systolic HF. They identified a clinically relevant concentration range for each HF biomarker in saliva as well as a critical value above which the patient's survival rate was significantly decreased. The POC care device I worked to develop is capable of processing a saliva sample and quantifying the amount of Gal-3 and S100A7 in the sample via a multiplexed electrochemical immunoassay. This device provides a less invasive and more accessible means of monitoring the prognosis of HF for a patient over time, as saliva samples can be collected and tested often.

Two other capillary flow devices I developed are designed to process whole blood, and therefore require a small volume of a blood sample from a patient. Viscosity, hematocrit, and red blood cell (RBC) deformability and aggregation determine much of the flow characteristics of whole blood.[73] One device is used to identify the phenotype of a Sickle Cell Disease (SCD) patient's blood; SCD is the most prevalent genetic disease worldwide.[74] SCD is known to present as a wide variety of symptoms, and a one-size-fits-all treatment approach is not always effective

in treating the root cause of the patient's pain.[75-77] The device utilizes multiple microchannels to expose the blood to several reagents, and the visual output of blood flow into a nitrocellulose membrane (NCM) can provide insight into the most effective treatment approach for that patient's SCD.

Another device, called the Paper-based Clotting Analysis Test or PCAT, is used to assess the capability of a patient's blood to form a clot. Inhibition of coagulation using anticoagulants such as heparin or warfarin,[78] is required to reduce the risk for stroke, pulmonary embolism, heart attack, and other life-threatening cardiovascular diseases. Constant monitoring of long-term anticoagulation efficacy is critical for these patients.[78, 79] Unfortunately, monitoring anticoagulation is usually performed by trained specialists in a hospital or laboratory setting, resulting in expensive tests and long waiting times to get results.[79] The device I worked to develop aims to recreate the process of primary hemostasis or blood clotting within a low-cost, capillary flow device. The device flows whole blood through at relatively high flow rates (~50 μL/min) for sustained durations (~5-10 min) to cause thrombus formation at the site of a stenosis within the device.

1.4 My Contributions

The work described in this dissertation bridges the gap between effective means of monitoring human health and access to these methods by harnessing the power of fluidics. The microfluidic devices I am working to develop will serve as accessible ways to rapidly obtain pertinent health information so that more meaningful treatment approaches for each individual patient can be made. Chapter 2 discusses the first system, comprised of two devices that both use pump-driven flow: the first device uses gut tissue explants to generate a physiologically relevant model of the intestinal barrier, and the second houses electrochemical sensors to monitor relevant

molecules within the media as it exits the first device. This data was published in *Lab on a Chip,*[80] *ChemRxiv*,[81] and has been accepted for publication in *Electroanalysis.*

Chapter 3 describes a POC capillary flow microfluidic device for processing patient saliva and measuring levels of two HF biomarkers using an electrochemical detection method. Preliminary work done by my colleague Trey Pittman was published in *Sensors and Actuators B:Chemical*[82] and *Theranostics*.[2] The current work was presented at CSU Demo Days in April 2024 and is in progress to be submitted for publication.

Chapter 4 discusses two separate devices for processing patient blood samples. The first is a collaboration with the Lam Lab at Emory University, and it is used to identify the phenotype of a SCD patient's blood so proper treatment can be administered. The second device is a collaboration with the Bark lab at Washington University in St. Louis, and it is a Paper-based Clotting Analysis Test (PCAT). The PCAT is used to assess if a patient's blood can properly form a clot via a primary hemostasis pathway. This device still requires significant development and data collection before a publication can be submitted.

Overall, this dissertation aims to develop a series of fluidic devices that facilitate sensitive and accurate methods for monitoring of human health, and finding ways to increase their accessibility so that they can be offered to patients in low income and resource-limited communities. The devices described within this dissertation have the power and the potential to be truly life-changing for millions of people.

References

1. T. A. Ghebreyesus, *Journal*, 2023.
2. T. W. Pittman, D. B. Decsi, C. Punyadeera and C. S. Henry, *Theranostics*, 2023, **13**, 1091-1108.
3. S.-M. Yang, S. Lv, W. Zhang and Y. Cui, *Sensors (Basel)*, 2022, **22**.
4. A. S. Tan, S. N. Nerurkar, W. C. C. Tan, D. Goh, C. P. T. Lai and J. P. S. Yeong, *SLAS Technology*, 2020, **25**, 522-544.
5. S.-u. Hassan, A. Tariq, Z. Noreen, A. Donia, S. Z. J. Zaidi, H. Bokhari and X. Zhang, *Diagnostics (Basel, Switzerland)*, 2020, **10**.
6. D. Xu, X. Huang, J. Guo and X. Ma, *Biosensors & Bioelectronics*, 2018, **110**, 78-88.
7. S. K. Srivastava, G. W. Foo, N. Aggarwal and M. W. Chang, *Biotechnology Notes*, 2024, **5**, 8-12.
8. C. M. Leung, P. d. Haan, K. Ronaldson-Bouchard, G.-A. Kim, J. Ko, H. S. Rho, Z. Chen, P. Habibovic, N. L. Jeon, S. Takayama, M. L. Shuler, G. Vunjak-Novakovic, O. Frey, E. Verpoorte and Y.-C. Toh, *Nature Reviews Methods Primers*, 2022, **2**.
9. Y. S. Zhang, J. Aleman, S. R. Shin, T. Kilic, D. Kim, S. A. Mousavi Shaegh, S. Massa, R. Riahi, S. Chae, N. Hu, H. Avci, W. Zhang, A. Silvestri, A. Sanati Nezhad, A. Manbohi, F. De Ferrari, A. Polini, G. Calzone, N. Shaikh, P. Alerasool, E. Budina, J. Kang, N. Bhise, J. Ribas, A. Pourmand, A. Skardal, T. Shupe, C. E. Bishop, M. R. Dokmeci, A. Atala and A. Khademhosseini, *Proc Natl Acad Sci U S A*, 2017, **114**, E2293-E2302.
10. K. W. Oh, *Micromachines*, 2020, **11**, 370.
11. A. P. Iakovlev, A. S. Erofeev and P. V. Gorelkin, *Biosensors (Basel)*, 2022, **12**.
12. M. A. Kenari, E. R. Ghomi, A. A. Kenari, S. M. S. Arabi, J. Deylami and S. Ramakrishna, *Polymers Advanced Technologies*, 2022, **33**, 3920-3934.
13. L. Dong, D.-W. Chen, S.-J. Liu and W. Du, *Scientific Reports*, 2016, **6**.
14. S. N. Bhatia and D. E. Ingber, *Nature Biotechnology*, 2014, **32**, 760-772.
15. C. Liu, Y. Qu, Y. Luo and N. Fang, *ELECTROPHORESIS*, 2011, **32**, 3308-3318.
16. A. H. C. Ng, U. Uddayasankar and A. R. Wheeler, *Analytical and Bioanalytical Chemistry*, 2010, **397**, 991-1007.
17. T. Ozer, C. McMahon and C. S. Henry, *Annual Review of Analytical Chemistry (Palo Alto, Calif.)*, 2020, **13**, 85-109.
18. J. R. Lake, K. C. Heyde and W. C. Ruder, *PLoS One*, 2017, **12**.
19. I. Jang, H. Kang, S. Song, D. S. Dandy, B. J. Geiss and C. S. Henry, *Analyst*, 2021, **146**.
20. C. Stolfi, C. Maresca, G. Monteleone and F. Laudisi, *Biomedicines*, 2022, **10**, 289.
21. A. S. Stewart, S. Pratt-Phillips and L. M. Gonzalez, *Journal of Equine Veterinary Science*, 2017, **52**, 10-22.
22. M. Vancamelbeke and S. Vermeire, *Expert Review of Gastroenterology & Hepatology*, 2017, **11**, 821-834.
23. W. M. Miner-Williams and P. J. Moughan, *Nutrition Research Reviews*, 2016, **29**, 40-59.
24. S. S. Ghosh, J. Wang, P. J. Yannie and S. Ghosh, *Journal of the Endocrine Society*, 2020, **4**.
25. R. Krajmalnik-Brown, Z.-E. Ilhan, D.-W. Kang and J. K. DiBaise, *Nutrition in Clinical Practice*, 2012, **27**, 201-214.
26. K. Oliphant and E. Allen-Vercoe, *Microbiome*, 2019, **7**, 91.
27. Y. Goto and H. Kiyono, *Immunological Reviews*, 2011, **245**, 147-163.

28. M. E. M. Obrenovich, *Microorganisms*, 2018, **6**.
29. S. Iacob, D. G. Iacob and L. M. Luminos, *Frontiers in Microbiology*, 2018, **9**.
30. J. M. Wells, O. Rossi, M. Meijerink and P. v. Baarlen, *PNAS*, 2010, **108**, 4607-4614.
31. Y. Guo, X. Chen, P. Gong, G. Li, W. Yao and W. Yang, *International Journal of Molecular Sciences*, 2023, **24**, 4089.
32. B. Martinez, L. A. Schwerdtfeger, A. Richardson, S. A. Tobet and C. S. Henry, *Anal Chem*, 2022, **94**, 9987-9992.
33. X. T. Qing Liu, Daisuke Maruyama, Mehrdad Arjomandi, and Arun Prakash, *American Journal of Lung Cellular and Molecular Physiology*, 2021, **321**, L65-L78.
34. X. Yang, P. Ai, X. He, C. Mo, Y. Zhang, S. Xu, Y. Lai, Y. Qian and Q. Xiao, *Movement Disorders*, 2022, DOI: 10.1002/mds.29063.
35. S. Aishwarya and K. Gunasekaran, *Letters in Applied Microbiology*, 2022, **75**, 1293-1306.
36. I. Sharon, N. M. Quijada, E. Pasolli, M. Fabbrini, F. Vitali, V. Agamennone, A. Dötsch, E. Selberherr, J. H. Grau, M. Meixner, K. Liere, D. Ercolini, C. d. Filippo, G. Caderni, P. Brigidi and S. Turroni, *Nutrients*, 2022, **14**, 2872.
37. E. L. Chatelier, T. Nielsen, J. Qin, E. Prifti, F. Hildebrand, G. Falony, M. Almeida, M. Arumugam, J.-M. Batto, S. Kennedy, P. Leonard, J. Li, K. Burgdorf, N. Grarup, T. Jørgensen, I. Brandslund, H. B. Nielsen, A. S. Juncker, M. Bertalan, F. Levenez, N. Pons, S. Rasmussen, S. Sunagawa, J. Tap, S. Tims, E. G. Zoetendal, S. Brunak, K. Clément, J. Doré, M. Kleerebezem, K. Kristiansen, P. Renault, T. Sicheritz-Ponten, W. M. d. Vos, J.-D. Zucker, J. Raes, T. Hansen, M. consortium, P. Bork, J. Wang, S. D. Ehrlich and O. Pedersen, *Nature*, 2013, **500**, 541-546.
38. S. Singh, P. Sharma, D. K. Sarma, M. Kumawat, R. Tiwari, V. Verma, R. Nagpal and M. Kumar, *Cancers*, 2023, **15**, 1913.
39. J. Qin, Y. Li, Z. Cai, S. Li, J. Zhu, F. Zhang, S. Liang, W. Zhang, Y. Guan, D. Shen, Y. Peng, D. Zhang, Z. Jie, W. Wu, Y. Qin, W. Xue, J. Li, L. Han, D. Lu, P. Wu, Y. Dai, X. Sun, Z. Li, A. Tang, S. Zhong, X. Li, W. Chen, R. Xu, M. Wang, Q. Feng, M. Gong, J. Yu, Y. Zhang, M. Zhang, T. Hansen, G. Sanchez, J. Raes, G. Falony, S. Okuda, M. Almeida, E. LeChatelier, P. Renault, N. Pons, J.-M. Batto, Z. Zhang, H. Chen, R. Yang, W. Zheng, S. Li, H. Yang, J. Wang, S. D. Ehrlich, R. Nielsen, O. Pedersen, K. Kristiansen and J. Wang, *Nature*, 2012, **490**, 55-60.
40. W. Turpin, S.-H. Lee, J. A. R. Garay, K. L. Madsen, J. B. Meddings, L. Bedrani, N. Power, O. Espin-Garcia, W. Xu, M. I. Smith, A. M. Griffiths, P. Moayyedi, D. Turner, E. G. Seidman, A. H. Steinhart, J. K. Marshall, K. Jacobson, D. Mack, H. Huynh, C. N. Bernstein and A. D. Paterson, *Gastroenterology*, 2020, **159**, 2092-2100.
41. J. Torres, F. Petralia, T. Sato, P. Wang, S. E. Telesco, R. S. Choung, R. Strauss, X.-J. Li, R. M. Laird, R. L. Gutierrez, C. K. Porter, S. Plevy, F. Princen, J. A. Murray, M. S. Riddle and J.-F. Colombel, *Gastroenterology*, 2020, **159**, 96-104.
42. A. Michielan and R. D'Incà, *Mediators of Inflammation*, 2015, DOI: 10.1155/2015/628157.
43. L. Antoni, S. Nuding, J. Wehkamp and E. F. Stange, *World Journal of Gastroenterology*, 2014, **20**, 1165-1179.
44. S. Jäger, E. F. Stange and J. Wehkamp, *Langenbeck's Archives of Surgery*, 2013, **398**, 1-12.

45. A. Picchianti-Diamanti, M. M. Rosado and R. D'Amelio, *Frontiers in Microbiology*, 2018, **8**.
46. G. M. Mawe, K. N. Browning, F. P. Manfredsson, M. Camilleri, F. A. Hamilton, J. A. Hollander, B.-A. Sieber, P. Greenwel, T. Shea-Donohue and J. W. Wiley, *Gastroenterology*, 2022, **162**, 1574-1582.
47. S. N. Freedman, S. K. Shahi and A. K. Mangalam, *Neurotherapeutics*, 2018, **15**, 109-125.
48. M.C. Houser and M. G. Tansey, *NPJ Parkinson's Dis*, 2017, DOI: 10.1038/s41531-016-0002-0.
49. S. Ryman, A. A. Vakhtin, S. P. Richardson and H. C. Lin, *Journal of Neurology*, 2023, **270**, 746-758.
50. S. Min, N. Than, Y. C. Shin, G. Hu, W. Shin, Y. M. Ambrosini and H. J. Kim, *Scientific Reports*, 2022, **12**.
51. S. K. Vashist, *Biosensors*, 2017, **7**, 62.
52. E. Farnesi, S. Rinaldi, C. Liu, J. Ballmaier, O. Guntinas-Lichius, M. Schmitt, D. Cialla-May and J. Popp, *Sensors*, 2023, **23**.
53. K. Sun, Y. Liu, W. Zhao, B. Ma, M. Zhang, X. Yu and Z. Ye, *International Journal of Molecular Sciences*, 2023, **24**.
54. I. C. Samper, C. J. McMahon, M. S. Schenkel, K. M. Clark, W. Khamcharoen, L. B. R. Anderson, J. S. Terry, E. N. Gallichotte, G. D. Ebel, B. J. Geiss, D. S. Dandy and C. S. Henry, *Analytical Chemistry*, 2022, **94**, 4712-4719.
55. P. M. Carrera, H. M. Kantarjian and V. S. Blinder, *CA Cancer J Clin*, 2018, **68**, 153-165.
56. L. H. Goetz and N. J. Schork, *Fertil Steril*, 2018, **109**, 952-963.
57. K. M. Clark, M. S. Schenkel, T. W. Pittman, I. C. Samper, L. B. R. Anderson, W. Khamcharoen, S. Elmegerhi, R. Perera, W. Siangproh, A. J. Kennan, B. J. Geiss, D. S. Dandy and C. S. Henry, *ACS Measurement Science Au*, 2022, **2**, 584-594.
58. F. Li, M. You, S. Li, J. Hu, C. Liu, Y. Gong, H. Yang and F. Xu, *Biotechnol Adv*, 2020, **39**, 107442.
59. P. B. Luppa, C. Müller and A. Schlichtiger, *Trends in Analytical Chemistry*, 2011, **30**, 887-898.
60. L. Roy, P. Buragohain and V. Borse, *Biosensors and Bioelectronics: X*, 2022, **10**.
61. A. S. John and C. P. Price, *The Clinical Biochemist Reviews*, 2014, **35**, 155-167.
62. K. A. A. Clark, S. W. Reinhardt, F. Chouairi, P. E. Miller, B. Kay, M. Fuery, A. Guha, T. Ahmad and N. R. Desai, *Journal of Cardiac Failure*, 2022, **28**, 171-180.
63. A. S. Bhatt, K. S. Jering, M. Vaduganathan, B. L. Claggett, J. W. Cunningham, N. Rosenthal, J. Signorovitch, J. J. Thune, O. Vardeny and S. D. Solomon, *JACC Heart Failure*, 2021, **9**, 65-73.
64. M. King, J. Kingery and B. Casey, *American Family Physician*, 2012, **85**, 1161-1168.
65. A. Koratala and A. Kazory, *Disease Markers*, 2017, **2017**, 1454986.
66. M. R. Cowie, A. D. Struthers, D. A. Wood, A. J. Coats, S. G. Thompson, P. A. Poole-Wilson and G. C. Sutton, *Lancet*, 1997, **350**, 1349-1353.
67. D. D. Mayo, J. E. Colletti and D. C. Kuo, *J Emerg Med*, 2006, **31**, 201-210.
68. G. S. Francis, G. M. Felker and W. H. Tang, *J Am Coll Cardiol*, 2016, **67**, 330-337.
69. B. Zaborska, M. Sikora-Frąc, K. Smarż, E. Pilichowska-Paszkiet, A. Budaj, D. Sitkiewicz and G. Sygitowicz, *International Journal of Molecular Sciences*, 2023, **24**.
70. X. Zhang, Y. Wan, R. Chata, A. Brazzale, J. J. Atherton, K. Kostner, G. Dimeski and C. Punyadeera, *Journal of Clinical Pathology*, 2016, **69**, 1100-1104.

71. X. Zhang, T. Walsh, J. J. Atherton, K. Kostner, B. Schulz and C. Punyadeera, *Theranostics*, 2017, **7**, 4350-4358.
72. X. Zhang, D. Broszczak, K. Kostner, K. B. Guppy-Coles, J. J. Atherton and C. Punyadeera, *Biomolecules*, 2019, **9**.
73. E. Nader, S. Skinner, M. Romana, R. Fort, N. Lemonne, N. Guillot, A. Gauthier, S. Antoine-Jonville, C. Renoux, M.-D. Hardy-Dessources, E. Stauffer, P. Joly, Y. Bertrand and P. Connes, *Frontiers in Physiology*, 2019, **10**.
74. F. B. Piel, A. P. Patil, R. E. Howes, O. A. Nyangiri, P. W. Gething, T. N. Williams, D. J. Weatherall and S. I. Hay, *Nature Communications*, 2010, **1**.
75. M. Samir K. Ballas, P. Susan Lieff, M. Lennette J. Benjamin, M. Carlton D. Dampier, M. Matthew M. Heeney, M. Carolyn Hoppe, M. Cage S. Johnson, M. Zora R. Rogers, M. Kim Smith-Whitley, M. Winfred C. Wang and M. Marilyn J. Telen, *Am J Hematol*, 2010, **85**, 6-13.
76. Y. Alapan, A. Fraiwan, E. Kucukal, M. N. Hasan, R. Ung, M. Kim, I. Odame, J. A. Little and U. A. Gurkan, *Expert Review of Medical Devices*, 2016, **13**, 1073-1093.
77. M. J. Telen, P. Malik and G. M. Vercellotti, *Nature Reviews, Drug Discovery*, 2019, **18**, 139-158.
78. J. A. Johnson and L. H. Cavallari, *Trends in Cardiovascular Medicine*, 2015, **25**, 33-41.
79. H. Li, D. Han, G. M. Paulettib and A. J. Steckl, *Lab on a Chip*, 2014, **14**.
80. A. E. Cherwin, H. N. Templeton, A. T. Ehrlich, B. H. Patlin, C. S. Henry and S. A. Tobet, *Lab on a Chip*, 2023, **23**, 4126-4133.
81. A. Roley, K. Clark, A. Richardson, B. Martinez, S. Tobet and C. Henry, *ChemRxiv*, 2021, **1**.

Chapter 2 – Enhancing Understanding of Intestinal Barrier Integrity Through Microfluidic Devices and Electrochemical Sensing

2.1 Overview

The goal of this chapter is to describe the development of an ex vivo microfluidic device model of the intestines, as well as a separate microfluidic sensor module device that can incorporate sensors for on-line monitoring of components related to tissue health within the first device. The work presented in this chapter was completed in collaboration with Dr. Stuart Tobet at Colorado State University, and Tobet Lab members Hayley Templeton, Brielle Patlin, and Alexis Ehrlich as well as Henry lab members Kaylee Clark, Brandaise Martinez, Jason Boes, Matt Russo, and Alec Richardson. This work was a collaboration between CSU and Applied Medical Resources Corporation, who provided the injection molded devices used for tissue experiments. Parts of the data shown here have been published in *Lab on a Chip*[1] and *ChemRxiv*,[2] and has been accepted for publication in *Electroanalysis*. Supporting information can be found in Appendix A.

2.2 Introduction

The importance of the intestinal barrier has become more obvious with recent observations of its involvement in disease progression and human health.[3-7] To ensure survival, the gut must maintain a barrier that retains the ability to digest and absorb nutrients while protecting the body from harmful substances.[4, 5] The diverse functions of the intestinal barrier are mediated by complex biochemistry and anatomy including epithelial, immune, neural, and bacterial interactions.[8, 9] Epithelial cells of the gut physically separate luminal contents from the underlying lamina

propria through apical transmembrane mucins and tight junctions. Together with the epithelial barrier, a mucosal barrier prevents unregulated passage of luminal contents into underlying tissue.[10] Disruptions to the epithelial and mucosal layers can lead to alterations in paracellular and transcellular permeability in what is termed as "leaky gut."[4] Leaky gut has been associated with the pathogenesis of conditions such as inflammatory bowel diseases (IBD),[11-13] autoimmune diseases such as celiac disease,[4] neurodegenerative disorders such as Alzheimer's and Parkinson's Disease,[14, 15] and neurodevelopmental disorders such as autism spectrum disorder.[16] Generation of an intestinal model that maintains the complexity of intestinal anatomy, microenvironment, and barrier is necessary to better understand how alterations in barrier integrity may contribute to disease states.

Fluidic and microfluidic devices have greatly expanded the toolbox for analytical measurements in countless fields. These devices have been used broadly for applications including single molecule detection,[17] immunoassays,[18] environmental analysis,[19] and organ-on-chip (OOC) devices.[20] An attractive method for microfluidic device fabrication is three-dimensional (3D) printing because it enables rapid prototyping of different designs in one step, and in some cases, multi-material parts with varying mechanical properties.[21, 22] Channel clogging, a common issue when printing internal microchannels, can be circumvented by 3D printing open-faced microfluidic devices and reversibly or irreversibly sealing the printed parts to various substrates.[23-26] Reversibly sealed microfluidic devices are especially desirable for OOC applications because they can be disassembled, sterilized, and reused for subsequent experiments.[27]

There are currently many approaches to study organ function that each have strengths and weaknesses.[28, 29] In vivo studies have the benefit of maintaining communication across organ systems. The gut is difficult to access in vivo, and probes inserted to monitor changes could disrupt

the natural environment. Using an alternative approach such as an ex vivo system can have significant benefits. Ex vivo models using tissue explants represent reasonable physiological similarity to tissue in vivo in terms of 3D structure and biological complexity.[30] They offer a powerful tool for studying cell-cell interactions, cellular responses, and extracellular matrix (ECM) remodeling processes.[31, 32] However, tissue explant models are limited by shortened lifespan of the tissues and challenges in recreating the microenvironment.[31] Simplified approaches to modeling these organs have been done by using in vitro models with two-dimensional (2D)[33-35] monolayer or 3D[36, 37] cell culture systems (e.g., using cell lines or primary progenitor cells) to mimic the gastrointestinal (GI) tract. The incorporation of microfluidics with 2D culture systems greatly increased these in vitro systems functionality by allowing for the inclusion of physical forces such as fluid shear stress, cyclic strain, and mechanical compression.[20] These OOC models offer utility in high throughput screening approaches for pharmaceutical, industrial, and toxicological research.[31] However, they fail to model the GI tract as they don't capture the complexity of either the microbiome or the cellular composition of the intestinal wall. Since these models do not have all the components which comprise the barrier, they can only provide partial modeling for conditions such as leaky gut.

To create a paradigm for intestinal microphysiological systems, several approaches[38-40] have incorporated microfluidics, but these models are still missing valuable components for gut health. Models such as the GOFlowChip[39] recapitulate some of the cellular diversity by using host cells that are derived from stem cells combined with inter- and extraluminal flow to carry nutrients and remove waste. However, there is no native microbial population so microbes must be injected into the organoid to have functionality and to study host-microbe interactions.[30] Even when systems include added bacteria, many of these systems do not consider the oxygen gradient that

exists within the GI tract. Our previous work showed that low oxygen is required for better preservation of microbiota ex vivo.[41] These systems lacking a microbiome or lacking an appropriate environment for a microbiome are missing a vital component of the cellular ecosystem of the host relevant for studying diseases like leaky gut. Alternatively, organotypic devices which utilized whole tissue explants have a variety of advantages including maintenance of local microbiome and cell diversity.[30, 40, 42] For example, the Intestinal Explant Barrier Chip[40] measured the functionality of porcine and human gut explants in terms of its ability to perform transcellular and paracellular transport of drug compounds over 24 h. Although, questions remain about the integrity of the tissue given that hemotoxylin and eosin staining indicated significant tissue disruption and specific cellular elements were not examined. While these approaches provide valuable information to the study of intestinal physiological processes, they fail to recapitulate important aspects of the complex environment of the intestines.

Electrochemical sensors are well suited for integration into fluidic devices because they are highly sensitive and selective, cost-effective, can be readily fabricated at micro scales, and exhibit fast response times.[43] While some OOC devices feature on-chip electrochemical or optical biosensors to monitor changes in environmental parameters (e.g. O_2, pH, CO_2)[41, 44, 45] and metabolic products (e.g. H_2O_2, glucose, lactate)[46, 47] in real-time, they often lack reusability and simple integration. In many devices, fractions collectors or off-chip assays are used, which lack the capability to measure changes in analytes with high time resolution and can require large working volumes. Monitoring dissolved O_2 is important in various biochemical and physiological processes,[48] but is hard to detect electrochemically.[48-51] H_2O_2 also plays an important role as a signaling molecule in regulating diverse biological processes such as immune cell activation and is also a product from reactions with oxidase enzymes such as glucose oxidase (GOx), lactate

oxidase (LOx), and cholesterol oxidase (ChoOx).[52] Similarly to O_2, detection of H_2O_2 typically requires expensive, complex, or time-consuming modifiers such as metal hexacyanoferrates, heme proteins, carbon nanotubes and graphene, metals and metal oxides, and metallophthalocyanines.[52-54]

Recently, thermoplastic electrodes (TPEs) have been introduced as easily moldable carbon composites with excellent conductivity and electron transfer kinetics.[55-62] A variety of thermoplastic binders have been used for TPEs including polymethyl methacrylate (PMMA),[55, 59] polycaprolactone (PCL),[56, 59, 63] cyclic olefin copolymer (COC),[57-59] polystyrene (PS),[61, 62] and Ecoflex®;[64] carbon composite binder choice must be carefully considered for all applications as it contributes greatly to the mechanical and electrochemical properties of the electrode platform.[65, 66] PCL and PS are of particular interest to this work as they can be pressed into templates without the need for inorganic solvent.[56, 59, 61-63] PCL has a low melting point and is FDA approved for medical applications because of its biocompatibility.[67-69] Prior to use as a TPE binder, PCL was not commonly use in electrochemical sensors. PS has also been used in many biomedical applications and, alternatively to PCL, has been reported more in electrochemical sensors.[70, 71] PS electrodes have been applied to biological[70, 72-80] and environmental[75, 81-84] applications. PS-based TPEs have been shown to have enhanced electrode kinetics compared to other reported techniques using PS.[61]

For devices that have integrated sensors, in many previously reported devices, if the sensor fails, both the device and the sensor require replacement.[85] This process can be expensive and time-consuming, particularly for OOC devices, in which integrated sensors are desirable for monitoring of tissue-specific biochemical processes.[86] Sensor module designs featuring plug-and-play architectures are advantageous because individual sensors can be swapped when failures in

occur, and microfluidic platforms can be reused in separate experiments requiring different sensors.[85] Examples of plug-and-play sensor modules include 3D-printed microfluidic devices that accommodate electrochemical sensors housed in finger-tight fittings[87] or custom holders,[21] as well as a 3D-printed flow cells that accommodate off-the-shelf optical components.[86]

The intestinal model system I have worked to develop serves as a bridge between 2D and in vivo systems currently in use and provides a layer of complexity that aids in investigating the gut barrier—which is necessary to understand conditions such as leaky gut. I have worked to expand the utilization of an ex vivo dual flow microfluidic device to create a model of leaky gut using bacterial collagenase. Bacterial collagenases are enzymes produced by endogenous gut bacteria that have the natural ability to digest collagen, thus contributing to the degradation of the extracellular matrices (ECM).[88] Here, we introduced bacterial collagenase into the luminal flow of the device to disrupt the epithelial and mucosal barriers of the gut, resulting in a leaky gut-like phenotype. We observed changes to gut permeability, collagen type 1 within the ECM, and epithelial cell (goblet cell) morphologies as a result of collagenase exposure. Using an enzyme that can be secreted by commensal bacteria provides a model for future studies of leaky gut. This device was to create a model of leaky gut that recreates physiological hallmarks of the disorder enabling future investigation into causative mechanisms.

Concurrent work was done to develop an electrochemical sensor module that can later be incorporated downstream of the tissue chip; this device makes use of magnetic closures to create a sealed device that can operate at relatively high pressures. This auxiliary sensor module device was developed as two versions: V1, with removable, plug-and-play sensors made with PCL TPEs, and V2, with built-in PS TPE sensors. In V2, the reversible seal also allows for the TPE surface to

be sanded and renewed, or the entire sensor part can be removed and remade for a different set of electrodes that are optimized for different analytes. The reported sensor modules use magnets to allow for a simple, reversible seal.

2.3 Materials and Methods

2.3.1 Microfluidic Device Design

The gut microfluidic device (Figure 1) was designed in SolidWorks (Dassault Systémes, Vélizy-Villacoublay, France) and manufactured via injection molding (Applied Medical, Rancho Santa Margarita, CA) and consisted of three COC (TOPAS Grade 8007) layers separated by polyurethane gaskets (PORON AquaPro, Rogers Corporation, Chandler, AZ). Details on device design can be found in a previous publication.[41] A video demonstrating device assembly can be found in Appendix A. Briefly, each gasket made individual fluidic channels and tissue was placed in the middle layer where luminal and serosal sides have separate channels. The tissue was placed in the device such that the luminal side of the tissue was facing up when it was placed inside. A 50μm pore Nitex mesh (Genesee Scientific, San Diego, CA) was secured at the bottom of the middle layer with quick-setting epoxy (J-B Weld, Marietta, Georgia, USA) to support the tissue. The luminal side of the tissue had an additional piece of mesh glued onto it so that the full perimeter of the tissue was securely held in place. This mesh had a 2mm diameter hole in the center to allow the media to reach the tissue that wasn't in contact with any glue (Figure 1(A)). This modification was made to eliminate the use of nicardipine, a calcium channel blocker. Nicardipine was previously used in the media to keep the tissue flat in the device by decreasing intestinal muscle contractions.[41] The use of mesh and epoxy ensured the tissue remained flat in the device even when contractions were occurring. The top mesh piece and the tissue were secured around the edge using cyanoacrylate glue (Loctite Super Glue, Henkel Corporation, Bridgewater, NJ) to help prevent

leakage. The top piece of the device had integrated snap-fit fasteners that allowed for quick assembly to decrease the time tissue was without media.

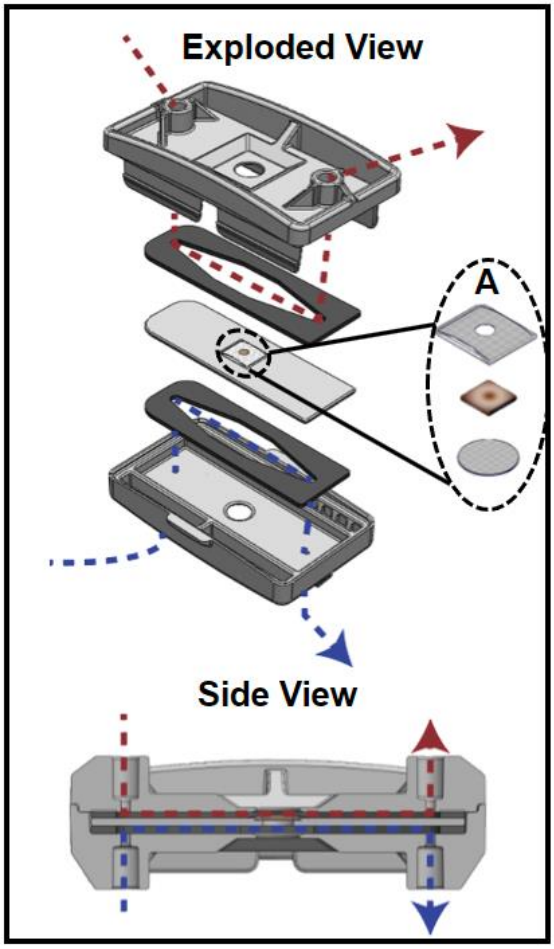

Figure 2.1. The organotypic microfluidic device. Exploded view of the device with the tissue piece between two gaskets that define flow paths for luminal (above, red) and serosal (below, blue) media flows, respectively. **(A)** shows the components held within the middle piece of the device; two mesh pieces provide support above and below the tissue. Below shows a side view of the assembled device, with the flow paths for luminal (above, red) and serosal (below, blue) media flows.

The sensor module devices (Figure 2) were designed in SolidWorks CAD software (Dassault Systems, Waltham, MA) and the top and bottom layers were 3D-printed with a Form 3 SLA printer (Formlabs, Somerville, MA) using Clear V4 resin. After printing, the devices were soaked in isopropyl alcohol for 20 minutes to remove uncured resin and subsequently post-cured

according to Formlabs recommendations. The middle layer consists of a 20A durometer silicone gasket (McMaster-Carr, Elmhurst, IL) cut with an Epilog Zing laser cutter to define the microfluidic channel (1 mm width, 200 μm height, 33 mm length). N42 Neodymium bar magnets (K&J Magnets Inc., Pipersville, PA) were installed in slots on the inner surface of each 3D-printed layer using cyanoacrylate glue (Krazy Glue, Elmers Products, High Point, NC). The device was intentionally designed such that opposing magnets are nearly in contact after device assembly to maximize the attractive force between magnets. Because the magnets dictate the alignment, the sensor module can be assembled correctly in under 5 s while maintaining high quality seals, even by untrained users.

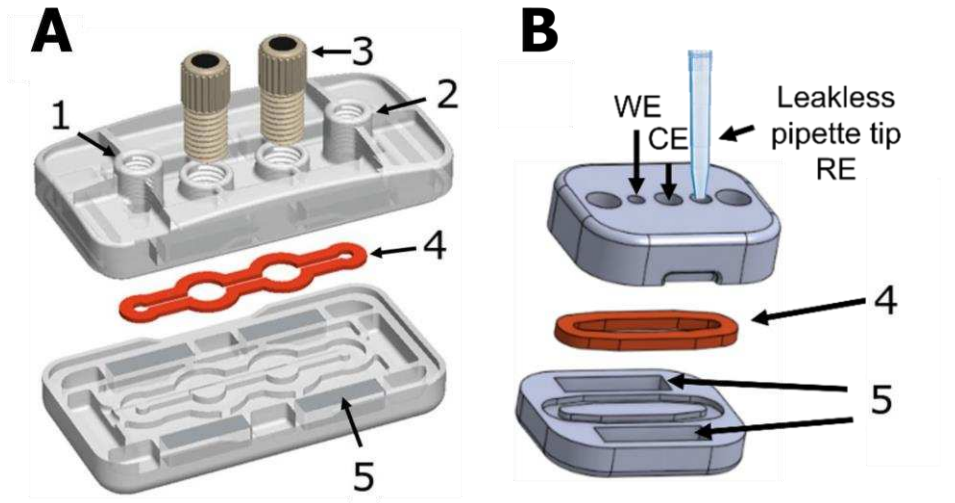

Figure 2.2. The sensor module microfluidic devices. **(A)** shows an exploded view of the first version of the device (V1), with the middle laser-cut gasket to define the flow paths of liquid within the device and removable sensors. **(B)** shows an exploded view of an update version of the device (V2) with incorporated sensors and built-in counter and reference electrodes. **1-5** indicate the fluid inlet, fluid outlet, electrochemical sensors, gasket, and magnets, respectively. WE = working electrode, CE = counter electrode, RE = reference electrode.

In the first version of the device (V1, Figure 2(A)) the top 3D-printed layer contained threaded inlet/outlet ports and two sensor ports that accommodate 10-32 and 1⁄4-28 fingertight fittings (IDEX Health and Science, LLC, Oak Harbor, WA), respectively. The bottom 3D printed

layer of V1 featured notches aligned with the sensor ports to prevent installed sensors from occluding the microfluidic channel, and rubber O-rings (McMaster-Carr, Los Angeles, CA) were installed at the base of the inlet/outlet ports to ensure leak-free connections.

Unfortunately, the V1 design was not easily translatable for PS-based TPEs. The increased temperature required for TPE fabrication with PS melted and deformed the fingertight fittings. In V2 of the sensor module, the TPEs are printed directly into the 3D printed top layer of the device. 3D printing is an attractive method for device fabrication is because it allows all features of the electrode system template and fluidic channels to be fabricated at once and also enables rapid prototyping of different designs in one step.[21, 22] After the TPEs are integrated, a previously reported leakless Ag|AgCl reference electrode[89] was inserted into the module. Many reference electrodes require storage in a chloride solution when not in use, which would be inconvenient and potentially alter the surface of the other electrodes in the sensor module. The leakless reference used here does need storage solution and the solution needed for the electrode to function (described above in the experimental section) does not contact the flow channels or other electrodes. A TPE carbon pseudo-reference electrode could also be used but Ag|AgCl is more stable.[90]

2.3.2 Intestinal Modeling - Animals, tissue collection, and gut device loading

Male C57BL/6 background mice aged 3-4 months were used in all experiments. Animal protocols were approved by the Institutional Animal Care and Use Committee (IACUC) at Colorado State University. Mice were kept on a 12-h light/dark cycle with access to standard chow and water *ad libitum*.

To prepare for tissue collection, mice were deeply anesthetized with isoflurane and terminated via decapitation. The intestines were removed from stomach to colon and immediately

placed in 4°C 1x Krebs buffer (in mM: 2.5 KCl, 2.5 $CaCl_2$, 126 NaCl, 1.2 $MgCl_2$, 1.2 NaH_2PO_4) containing 1µl/1mL nicardipine (Sigma Aldrich, St. Louis, MO), an L-type calcium ion channel blocker, to prevent contractions during dissection. Proximal colon was then dissected to remove any remaining mesentery. Using angled vascular scissors, the tissue was cut longitudinally to form a flat piece of tissue which was then cut into ~5mm sections (Figure 1(A)). Using a small strainer spoon, tissue sections were gently scooped up and transferred to the device. This method allowed the tissue section to remain flat and promoted a smooth transfer to the device. Only a small corner of the tissue needed to be touched with forceps to move the tissue to the device's middle piece. This significantly decreased tissue stretch, which was previously associated with tissue damage.[91] Once the tissue was placed inside the device, the top layer of Nitex mesh was gently placed on top and cyanoacrylate glue was placed around the edges of the mesh. Careful attention was paid to not allow glue to contact the tissue beyond the perimeter. To cure the glue, 1x Krebs buffer was applied. A video demonstrating the loading of a tissue section into the middle piece of the device is included in the Supplemental Information (Appendix A.V.1). The device was immediately snapped closed and transferred to a 37°C incubator where the media inlets were connected. The syringe pumps were run at a purge setting for ~10s to fill the device so the tissue was in contact with media in less than 60s after it was removed from the Krebs solution.

2.3.3 Electrode Fabrication

TPE fabrication has been previously described.[92] Briefly, the thermoplastic was solvated and combined with graphite. This mixture was mixed until it dried (typically under 10 minutes) and then heat-pressed into the 3D-printed electrode template. Finally, excess material was sanded away. For the plug-and-play electrodes (sensor module V1), electrochemical sensors were made by heat-pressing the TPE material into 1⁄4-28 PEEK fingertight fittings. To fabricate the removable

sensors, PCL pellets were first dissolved in dichloromethane followed by the addition of graphite at a 3:1 (w/w) graphite-to-PCL ratio. Once homogenized, the mixture was poured onto a silicon wafer to allow the solvent to evaporate. The dried PCL composite was then molded into fingertight fittings using a hydraulic heat press set to 75°C. Next, the ends of the fittings were sanded to remove excess material and exfoliate the carbon. Prior to electrochemical experiments, fingertight fittings were wrapped with Teflon tape to prevent leakage. In V2, the dried PS composite was molded directly into the device's top layer using the heat press set to 85°C. Each electrode's resistance was measured with a two-point probe (Fluke 187 multimeter, accuracy of 0.01 Ω) for quality control purposes. Electrical connections were established using electrical wire and silver paint, and epoxy was applied over the connections for mechanical reinforcement.

2.3.4 Media Preparation and Experimental Flow

Adult Neurobasal CTS culture media with 2% B27 supplement (Thermo Fisher Scientific, Waltham, WA) and 3% 1 M HEPES buffer (Sigma Aldrich, St. Louis, MO) was used. Experiments to investigate tight junctions and the mucus layer were done with the same media except for lower glucose (4mM versus 25mM) and the omission of phenol red in the culture media. Luminal media contained 0.5 M sodium sulfite (oxygen scavenger) to decrease oxygen levels.[41] Media was loaded in sterile 10 mL syringes and placed in a 37°C incubator to equilibrate and remove air bubbles before experiments. Experiments to analyze barrier permeability after collagenase exposure included luminal media with 0.1% 10kDa dextran fluorescein (Thermo Fisher Scientific, Waltham, WA) for only the last 2 h of the experiment.

Each device had two 10 mL syringes filled with media connected to NE-300 pumps (New Era Pump Systems Inc., Farmingdale, NY) that continually flowed media across both luminal and serosal sides of the tissue. For the first 24 h of the experiment, control media was used to allow

the tissue to stabilize and to establish a baseline of device performance with an intact, healthy barrier. The flow rate on the luminal side was 250 µL/h, and on the serosal side it was 200 µL/h. The flow rates were optimized using computational fluid dynamics simulations to identify appropriate levels of shear stresses to the tissue surface. After 24 h, the media for the luminal side of the tissue was replaced with collagenase-containing media—control (0 U), low ($5.80*10^{-2}$ U), or high ($1.16*10^{-1}$ U) collagenase (Worthington Biochemical Corporation, Lakewood, NJ) concentrations. These concentrations were chosen after performing a dosage curve to determine levels of collagenase that showed measurable disruption of the tissue over 48 h without complete destruction. Working stocks of bacterial collagenase were diluted in water and because media is composed mainly of water; control media did not utilize the addition of water as a vehicle.

Following collagenase addition, the device ran for an additional 48 h. After a total of 72 h, the tissue was removed from the device and placed in a small weigh boat. A solution containing 0.5% cetyl pyridium chloride (CPC) in 4% paraformaldehyde (PFA) was then gently pipetted onto the luminal surface of the tissue. After approximately 5 min the tissue was removed from the weigh boat and stored in 0.5% CPC in 4% PFA at 4°C for 24 h. Tissue was then stored in 0.05 M phosphate buffered saline (PBS) at 4°C for sectioning.

2.3.5 Electrochemical Reagents and Experimental Flow

Solutions for electrochemical experiments were prepared using 18.2 MΩ · cm water purified using a Milli-Q system (MilliporeSigma, USA). Graphite (Grade 3569) was purchased from Asbury Graphite Mills, INC. (Asbury, NJ). Graphite (MG-1599, size ~15 µm) was purchased from Great Lakes Graphite, Inc. (Toronto, Canada). Polycaprolactone (PCL) was purchased from ThermoMorph® (Toledo, OH) and polystyrene m.w. 45,000 (45K PS) was purchased from Sigma Aldrich (Saint Louis, MO). ACS grade dichloromethane, potassium nitrate, and 30% hydrogen

peroxide were purchased from Sigma-Aldrich (Saint Louis, MO). Dichloromethane and potassium nitrate (cryst./certified ACS) were purchased from Fisher Chemical (Waltham, MA). Potassium ferricyanide(III) was purchased from Sigma-Aldrich (Saint Louis, MO). Dopamine hydrochloride (99%) was purchased from Alfa Aesar (Haverhill, MA). Ferrocenylmethyl trimethylammonium ($FcTMA^+$) was synthesized in house using a previously reported method.[93]

FcTMA+ and dopamine redox probes were used to assess the performance of the different electrode materials, and cyclic voltammograms (CVs) of sanded and heat-pressed PCL- and PS-based TPEs were collected. Electrochemical measurements for characterization were recorded using a CHI660b potentiostat (CH Instruments, Inc., Austin, TX). All experiments were performed with a three-electrode system using either the PS-TPEs or PCL-TPEs as the working electrode, a saturated calomel electrode (SCE) as a reference electrode, and larger surface area TPE of the same polymer type as the counter electrode. All solutions were prepared and diluted in 0.1 KNO_3 or 0.05 M phosphate buffer (pH 7.4) prior to measurements (denoted in figure captions). Cyclic voltammetry (CV) was performed to characterize FcTMA+ detection by scanning from 0.0 V to +0.8 V at a scan rate of 100 mV/s. CVs to characterize dopamine detection were scanned from -0.2 V to +0.8 V at a scan rate of 100 mV/s. CVs to characterize O_2 detection were scanned from -0.9 V to +0.9 V at a scan rate of 100 mV/s. CVs to characterize H_2O_2 detection were scanned from -0.4 V to +0.8 V at a scan rate of 100 mV/s. Replicate measurements for all CVs were recorded in the same solutions with different TPEs.

The sensor module was tested amperometrically in flow with 1 mM H_2O_2. Two syringe pumps (New Era Pump Systems, Inc. and Harvard Apparatus) were connected to a T-junction manual valve which was then connected to the inlet for the sensor module. One syringe contained 0.05 M phosphate buffer (pH 7.4) and the other contained 1 mM H_2O_2 in 0.05 M phosphate buffer

(pH 7.4). Flow rate for both pumps was set to 1.0 mL/min. The valve was switched back and forth from one pump to the other (stopping flow for the pump for which the valve was closed). Potential was held at +0.6 V vs. an Ag|AgCl reference for amperometry experiments with H_2O_2.

2.3.6 Tissue sectioning and histochemistry

Tissue sections were prepared from 1-3 mm sections of colon and submerged in 4% agarose. The tissue was in agarose for a total of 9 min: 5 min on a room temperature shaker, and 4 min at 4°C to ensure polymerization. Once the agarose was hardened, tissue was cut at a thickness of 50 µm on a vibrating microtome (VT1000S; Leica microsystems, Wetzlar, Germany).

For lectin histochemistry and immunohistochemistry, sections were washed in 1x PBS for 10 minutes at 4°C and were then incubated in 0.1M glycine for 30 min at 4°C, followed by three, 5-min PBS washes. Next, tissue was incubated in 0.5% sodium borohydride at 4°C for 15 min, followed by three, 5 min PBS washes. Sections were blocked in PBS with 5% normal goat serum (NGS; Lampire Biological, Pipersville, PA), 1% hydrogen peroxide, and 0.3% Triton X (TX) for 1 h at 4°C with a change of solution at 30 min. Following blocking, sections were placed into primary antisera with PBS containing 5% NGS and 0.3% TX for 3 days. Primary antibodies used were anti-c-kit (ACK2; Novus Biologicals) at 1:250, Ulex Europaeus Agglutinin I conjugated to Rhodamine (UEA-1; Vector Labs) at a concentration of 0.125µg/mL, anti-claudin-1 (Invitrogen) 1:200, anti-peripherin (Sigma-Aldrich) 1:300, anti-Collagen I (Novus Biologicals) 1:500 and anti-MUC-2 (Novus Biologicals) at 3 µg/mL. Following primary antibody addition, sections were washed at room temperature in PBS with 1% NGS and 0.32% TX four times at 15-min intervals. Sections with anti-peripherin and anti-claudin-1 primary antibodies were incubated for 2 h at room temperature in PBS containing 0.02% TX and Alexa fluor 594 conjugated to secondary antibodies specific to the species of the primary antibodies at a 1:500 dilution. Sections originally incubated

with anti-MUC2, anti-collagen I, anti-ACK2 primary antibodies were incubated for 2 h in biotinylated secondary antiserum (anti-rabbit 1:2500 or anti-rat, 1:1000; Jackson ImmunoResearch, West Grove, PA) specific to the species of the primary antibodies and were constituted in PBS with 0.32% TX. Sections were washed four times at 15-min intervals in PBS with 0.02% TX before being placed in their tertiary conjugated antibody (AF 594) constituted in PBS with 0.32% TX for 1 h at room temperature. Sections were then washed in PBS, mounted on slides, and cover slipped with an aqueous mounting medium (Aqua-Poly/Mount, Polysciences, Warrington, PA).

2.3.7 Tissue imaging and analysis

Images were taken using a Zeiss LSM800 upright confocal laser scanning microscope and a 20x (W Plan-Apochromat 20X/1.0 DIC Vis-ir ∞ /0.17) objective or Olympus BX61 equipped for epifluorescence imaging. All image analyses were performed using Fiji (v1.0; NIH). To quantify the relative fluorescence intensity of 10kDa dextran fluorescein penetration into the tissue, 12 lines were drawn from the luminal surface to the bottom of the crypts and a plot profile of the fluorescence intensity (gray value) across each line was generated; the data from all 12 lines was averaged to produce a representative measure of dextran fluorescein penetration (Figure 3(D)). Plots of the relative fluorescence of each tissue were compared to relate the permeability to the respective treatment regime, where a higher gray value correlated to more dextran fluorescein within the tissue (Figure 3(D)). To compare treatment groups to control, a one-way ANOVA was performed.

To analyze mucin 2 immunoreactivity (MUC2-IR), max intensity Z-projections were performed through the center 30 µm of each image stack. Regions of interest (ROI) were defined as 60 x 75µm sections of the apical half a crypt. Three crypts were analyzed per sample. Mean

grey value of MUC2-IR was analyzed after performing a Gaussian blur and watershed to eliminate false signal and clearly define cells.

2.4 Results and Discussion

2.4.1 Tissue Health and Barrier Integrity in the Gut Microfluidic Device

We first sought to verify that the device and experimental setup did not compromise tissue health. Following previous protocol,[41] colon explants were kept in the device for 72 h ex vivo without antibiotics and with low dissolved oxygen in the mucosal media and ambient oxygen in the serosal media, producing a gradient across the tissue. A key feature of the experimental design in the current study was eliminating the use of nicardipine in the media. Nicardipine is an L-type calcium channel blocker that is commonly used in ex vivo preparations to prevent muscle contractions. Calcium channels play vital roles in several cellular physiological functions by allowing controlled transport of calcium across the plasma membrane.[94] By eliminating the need for nicardipine in our device media, we have eliminated a possible variable of physiological disruption and ensured a more accurate physiological environment.

Colon explants maintained patterned crypts and proper arrangement of submucosal and muscular layers (Figure 3(A)). A specific type of epithelial cell, known as goblet cells, are responsible for producing and secreting mucus in the colon. Goblet cell mucopolysaccharides were identified via Ulex Europaeus Agglutinin I (UEA-1) conjugated to Rhodamine. Peripherin is a type III intermediate filament protein largely expressed on peripheral neurons and was therefore used to label enteric neurons. Mast cells are important cells of the innate immune system and were labeled using an antibody known as ACK2 that recognizes c-kit receptors found on the surface of mast cells. Immunohistochemistry (IHC) showed maintenance of neural (peripherin), epithelial (UEA-1), and immune (ACK2) cell populations in control tissue after 72 h in the device (Figure

3(C-E)). The mucosal barrier of the colon is composed of two layers-an inner layer firmly attached to epithelial cells and a loose outer layer. To ensure that constant flow over the tissue did not remove the mucous layer, tissue was fixed in 0.5% CPC in 4% PFA to preserve the inner mucus layer by maintaining the glycosaminoglycans in the extracellular space.[95] UEA-1 labeling of mucopolysaccharides confirmed maintenance of the inner mucosal layer after 72 h in the device (Figure 3(D)). We previously confirmed that luminal and serosal flows remained independent over 72 h by including fluorescein in only luminal media; only luminal effluents were found to have a measurable amount of fluorescence, confirming that the barrier was still intact.[41] Figure 3(B) shows relative fluorescence of the luminal and serosal effluents, respectively, for the last 2 h of the experiment where the luminal media contained 10 kDa MW dextran fluorescein. The relative fluorescence units (RFUs) were determined using a plate reader (PerkinElmer, USA), where the RFU value of a blank sample (serosal media that was not used in a device) was subtracted. The data plotted is an average of three replicates. Only measurable fluorescence was detected in the luminal channel, confirming that the barrier was still intact after 72 h in the device.

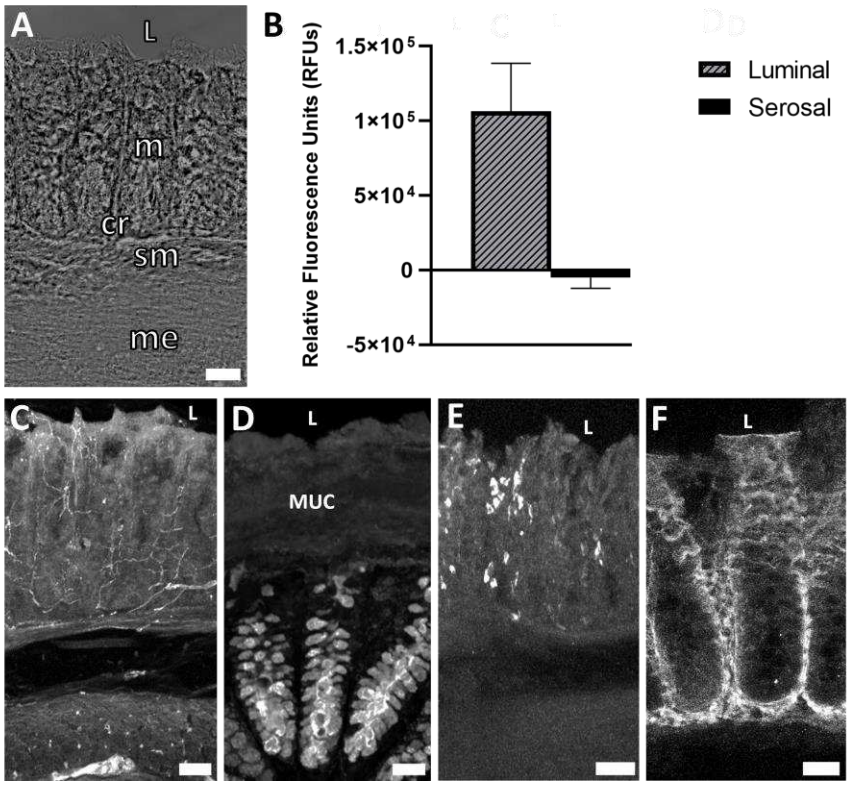

Figure 2.3. Device maintained tissue health and barrier function without nicardipine over 72 h. (A) Brightfield image showing maintenance of colon morphology. **(B)** Relative fluorescence of 10kDa dextran fluorescein in the luminal and serosal effluents from the device from the last 2 h of the experiment. **(C)** Peripherin labeled nerve fibers in crypts, mucosal plexus, and myenteric plexus. **(D)** Maintenance of epithelial cells and inner mucosal layer indicated by UEA-1^{+} material. **(E)** Maintenance of immune cells indicated by $ACK2^{+}$ mast cells in lamina propria. **(F)** Maintenance of tight junctions indicated by claudin-1 immunoreactivity. L=lumen, MUC=mucus layer, m=mucosa, sm=submucosa, me=muscularis externa, cr=crypt, scale bars are 50μm for **(A), (C), & (E)**, scale bar is 25 μm for **(D) & (F).**

2.4.2 Effect of Collagenase on Barrier Permeability

We next sought to determine if tissue treated with collagenase could serve as a model for leaky gut and determine its impact on barrier permeability. A key physiological hallmark of leaky gut is increased epithelial permeability indicated by increased passage of luminal molecules across epithelial cells into underlying lamina propria.[96] To investigate this, 10 kDa molecular weight dextran fluorescein was included in the luminal media for the last 2 h of the experiment. Dextran fluorescein does not covalently attach to anything within the tissue but can freely diffuse. Analysis

of epithelial and mucosal tissues revealed some diffusion of dextran fluorescein into the epithelial layer of all tissue explants, with collagenase-treated tissue showing greater fluorescence intensity into the underlying mucosa (Figure 4(B-C)). The relative fluorescence of each tissue was measured using Fiji (v1.0; NIH), where a higher gray value correlated to more diffusion of dextran fluorescein into the tissue; the average gray value from each treatment group (n=3) is shown in Figure 4(D), where the fluorescence values from the first 140 μm starting from the luminal edge of the tissue toward the crypt base were averaged and shown as a single bar per treatment group. Not all tissue sections were equal in crypt length, so 140 μm was chosen as a depth that would give a meaningful amount of dextran fluorescein penetration into the crypts for all tissue sections. The high collagenase treatment group showed the highest gray levels, and the control group had the lowest. From these results, we concluded that collagenase increased permeability of the gut barrier.

Another physiological indication of increased epithelial permeability is alterations in tight junction proteins. Tight junctions function to prevent passage of molecules and ions between epithelial cells. Claudins are a specific type of tight junction protein that can be classified as sealing/tight or pore-forming. In leaky gut, the expression of sealing claudins have been shown to decrease.[97] We examined claudin-1, which is broadly expressed in the intestinal epithelium and thought to have an essential role in tight junction integrity.[98, 99] Explants that were exposed to collagenase had decreased claudin-1 immunoreactivity compared to control (Figure 4(H-J)) indicative of impaired barrier integrity.

To further explore the effects of collagenase on barrier integrity, type 1 collagen (COL1), one of the most abundant types of collagen in the extracellular matrix (ECM) was assessed by immunohistochemistry. Collagenase enzymes play a large role in ECM remodeling. Increased

collagenase enzyme activity and uncontrolled remodeling of the ECM is distinctive in fibrotic and inflammatory bowel diseases.[100, 101] In healthy intestinal mucosa, collagen exhibits a wavy pattern referred to as "crimping" with fibers oriented in the vertical direction.[102] Increases in collagen tortuosity (twistedness) in vascular collagen is associated with increased remodeling and increased fragility of the ECM.[103, 104] Explants that were exposed to collagenase (Figure 4(F-G)) had decreased crimping and increased COL1 tortuosity, suggesting that collagenase treatment maladaptively impacted COL1 in colon mucosa. Proper functioning of the ECM is essential to

intestinal barrier integrity and our results demonstrate that collagenase disrupts COL1 which may have serious consequences to barrier integrity.

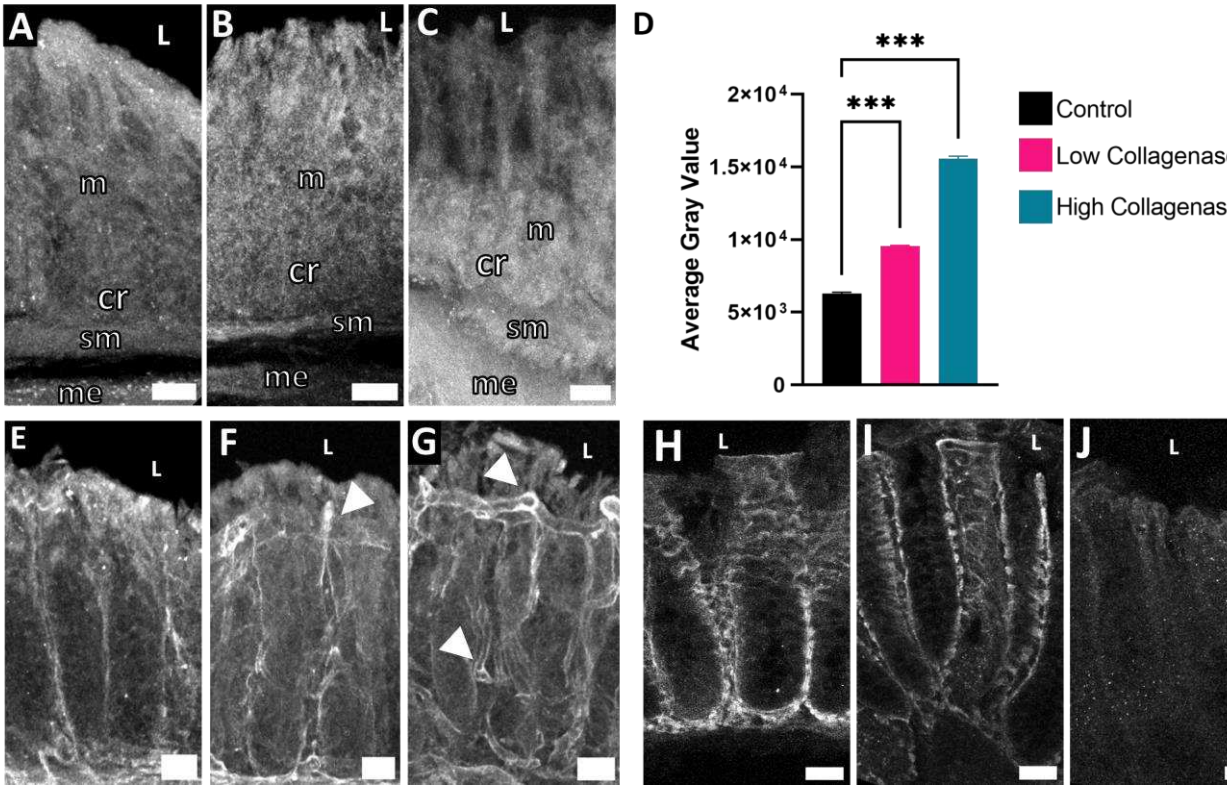

Figure 2.4. Collagenase exposure altered dextran fluorescein penetration and type 1 collagen morphology indicative of increased barrier permeability. (A) Tissue exposed to media containing no collagenase had minimal dextran fluorescein penetration into the mucosa. **(B)** Tissue exposed to low levels of collagenase had increased dextran fluorescein penetration into the mucosa. **(C)** Tissue exposed to high levels of collagenase had increased dextran fluorescein into the mucosa and into the submucosa. **(D)** Average fluorescence intensity of 10 kDa dextran fluorescein penetration into the first 140 µm of the tissue moving from luminal edge towards serosa across treatment groups. **(E)** Type 1 collagen immunoreactivity (COL1-IR) showed distinct vertical crimping pattern with no tortuosity in media with no collagenase. **(F)** Exposure to low levels of collagenase exhibited some COL1-IR tortuosity. **(G)** Exposure to high levels of collagenase increased COL1-IR tortuosity and decreased vertical crimping. Arrows indicate tortuous COL1**. (H)** Tissue not exposed to collagenase exhibits clear claudin-1 immunoreactivity around epithelial cells indicating maintenance of tight junctions. **(I)** Exposure to low levels of collagenase moderately decreased claudin-1 immunoreactivity. **(J)** Exposure to high levels of collagenase dramatically decreased claudin-1 immunoreactivity. L= lumen, m=mucosa, sm=submucosa, cr=crypt, me=muscularis externa, scale bars are 50 µm.

2.4.3 Effect of Collagenase on the Epithelial Cell Lining

Our next objective was to investigate the impact of collagenase on epithelial cells that form the intestinal barrier. Due to their distinctive characteristics and important roles in barrier maintenance we chose to investigate specialized epithelial cells known as goblet cells. Goblet cells produce and secrete mucus and were identified by labeling their mucopolysaccharides using fluorescently labeled Ulex europaeus agglutinin 1 (UEA-1) that recognizes terminal α-linked fucose residues. Goblet cells were further characterized by mucin 2 (MUC2), the most abundant mucin core protein for glycosylation in the colon that is produced and secreted by goblet cells. Collagenase-treated explants showed striking differences in goblet cell morphology, mucus layer thickness, and MUC2 immunoreactivity as a function of collagenase exposure (Figure 5). Healthy goblet cells have a characteristic goblet-like shape with the apical portion of the cell shaped like a cup and the basal portion shaped like a stem. The apical portion is distended as it contains mucin granules that are released into the lumen. Compared to control (Figure 5(A)), collagenase treated goblet cells lost their characteristic "goblet" shape becoming more circular (Figure 5(B)) or devoid of distinct shape (Figure 5(C)). Compared to control (Figure 5(A)), high collagenase treated tissue had a much thinner mucous layer (Figure 5(C)) indicative of an impaired mucosal barrier. Compared to control (Figure 5(D)), apical MUC2-IR decreased by 25% with low collagenase treatment (Figure 5(E)) and decreased by 31% with high collagenase treatment (Figure 5(F)). Alterations to goblet cell shape and MUC2 content is correlated with intestinal barrier disruption.[105] These results suggest that collagenase negatively impacted barrier epithelial cells and mucus production confirming that collagenase is a promising model for leaky gut.

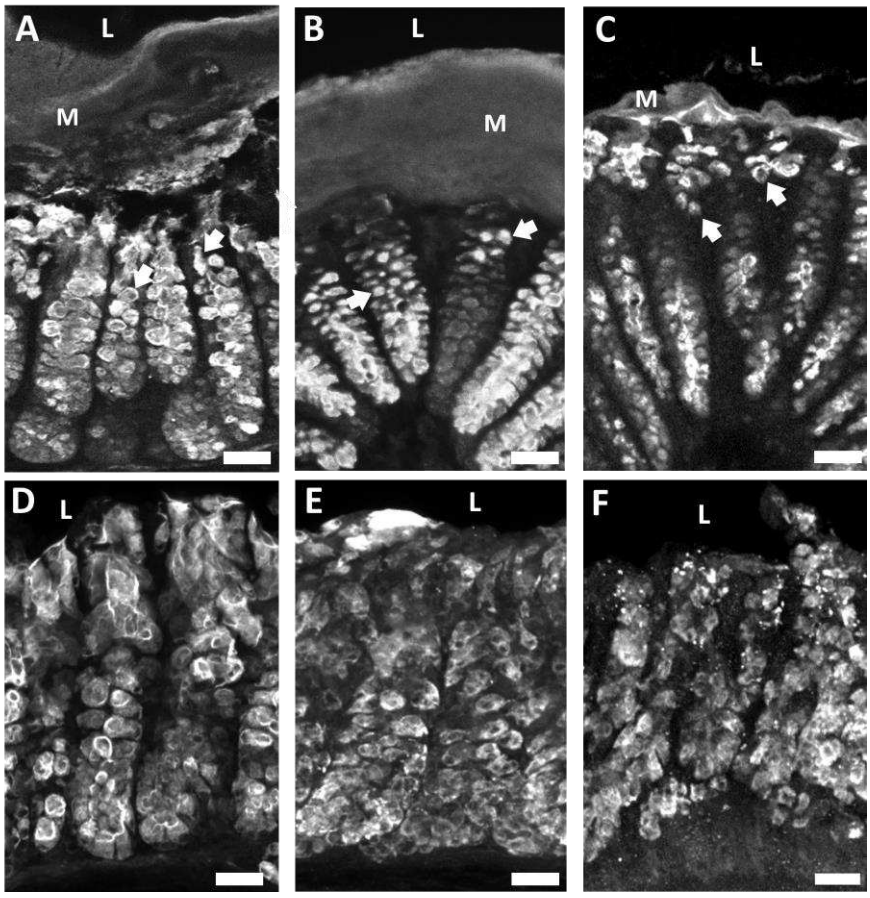

Figure 2.5. Collagenase treatment altered goblet cell morphology and mucus layer thickness as indicated by UEA-1 mucopolysaccharide labeling and decreased mucin 2 immunoreactivity (MUC2-IR). (A) Tissue exposed to media containing no collagenase exhibited healthy goblet cell morphology with "goblet" shaped goblet cells indicated by white arrows. The mucus layer remained intact. **(B)** Goblet cell shape became more circular when exposed to low levels of collagenase and the mucus layer remained intact. **(C)** Goblet cells lost their distinct shape when exposed to high levels of collagenase and the mucus layer decreased in thickness. **(D)** Apical MUC2-IR in tissue not exposed to collagenase. **(E)** Apical MUC2-IR decreased in a dose dependent manner when exposed to low collagenase and **(F)** high collagenase. Arrows indicate alterations in goblet cells morphology, M=mucus layer, L= lumen, scale bars are 25μm.

2.4.4 Electrochemical Characterization of PCL- and PS-based TPEs

Cyclic voltammograms (CVs) of sanded and heat-pressed PCL- and PS-based TPEs (electrode abbreviations: binder followed by treatment, e.g., PSS = polystyrene, sanded) are shown in Figure 6 for both $FcTMA^+$ and Dopamine. All the TPEs show reversible electrochemistry with

$FcTMA^+$; however, both heat-pressed PCL- and PS-based TPEs do not show reversible electrochemistry for dopamine. There is a considerable difference in the current magnitude between the TPEs. The sanded TPEs, as expected, had the highest current responses, with the anodic peak for PSS at 0.45 ± 0.04 mA cm^{-2} and the PCLS slightly lower at 0.35 ± 0.02 mA cm^{-2} (n=3). The heat-pressed TPEs have similar peak current with PSP at 0.17 ± 0.09 mA cm^{-2} and PCLP at 0.21 ± 0.01 mA cm^{-2}.

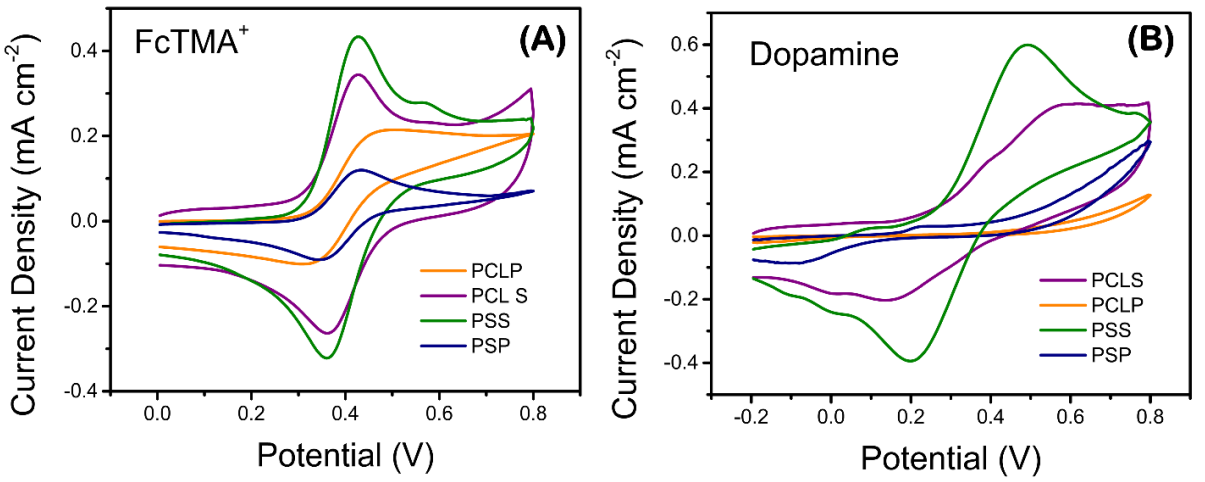

Figure 2.6: Electrochemical Characterization to Compare TPE materials Representative CVs (n=3) of PCL- and PS-based TPEs that are sanded and heat-pressed in **(A)** 1 mM $FcTMA^+$ and **(B)** 1 mM dopamine in 0.1 M KNO_3. Potential was scanned vs. a SCE reference at a scan rate of 100 mV/s for both **(A)** and **(B)**. PCLP = Polycaprolactone heat pressed, PCLS = Polycaprolactone sanded, PSP = polystyrene heat pressed, PSS = polystyrene sanded.

PCLS is significantly more capacitive than PSS (as in the $FcTMA^+$ CVs, Figure 6(A)) and has greater peak separation. In addition, PSS has higher peak current than PCLS (0.58 ± 0.06 versus 0.413 ± 0.006 mA cm^{-2} (n=3), respectively). The reversible electrochemistry exhibits excellent electrocatalytic activity on the unmodified TPEs, as carbon composite electrodes typically require modifications that can be expensive or time-consuming to achieve this type of electrochemistry with dopamine.[106] The PSS CVs are comparable to electrodes with glassy carbon, multiwalled carbon nanotubes, and graphene oxide.[107-111]

2.4.5 Proof-of-Concept Static O_2 Detection and H_2O_2 Detection in Flow with PS-based TPE Sensor Module

Next, the ability of PS-based TPEs to detect O_2 in static measurements was investigated. CVs of oxygen-rich and oxygen-deficient buffer were performed with heat-pressed (Figure 7(A))

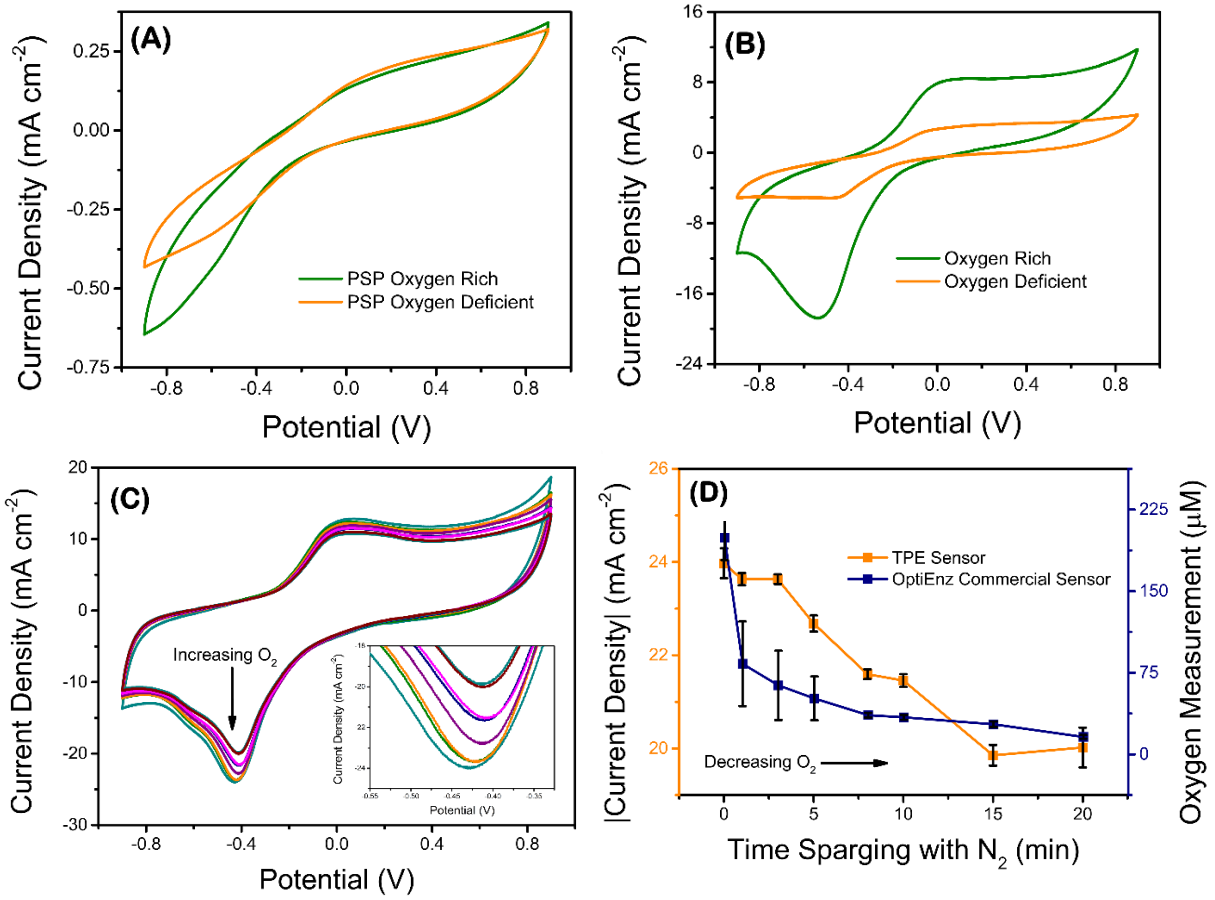

Figure 2.7: H_2O_2 Sensing Within Sensor Module V2 Representative CVs (n=3) of **(A)** heat-pressed and **(B)** sanded PS TPE in 0.05 M phosphate buffer (pH 7.4) with oxygen rich and oxygen deficient conditions. Oxygen rich conditions simply used the phosphate buffer as prepared. Oxygen deficient conditions were produced by sparging with N_2 for 30 min. **(C)** Representative CVs (n=3) of sanded heat-pressed PS TPE in 0.05 M phosphate buffer (pH 7.4) with at varying time points of sparging N_2 from 0-20 min. (Inset) Zoomed in plot of the cathodic peaks of the representative CVs. Potential was scanned vs. a SCE reference at a scan rate of 100 mV/s for **(A-C)**. **(D)** Plot of sensor responses for the (orange) sanded PS TPE sensor and (navy) a commercial OptiEnz Oxygen sensor vs. the time sparged. TPE sensor response is plotted from the absolute value of the corresponding cathodic peak from the CVs. Symbols and error bars represent average and standard deviation of the cathodic peak current of different electrodes/sensors in the same sparged solution (n=3).

and sanded (Figure 7(B)) PS-based electrodes. For PSS TPEs, reversible electrochemistry with an increase in both anodic and cathodic current is seen in phosphate buffer. The cathodic current peak increases 13 ± 2. mA cm^{-2} (n=3) in the oxygen rich buffer. There is a slight change in the cathodic current for PSP, but it does not contain peaks and the current is comparatively almost an order of magnitude lower than PSS.

Figure 7(C) shows CVs of increasing concentration of O_2 using sanded PS-based TPEs, and Figure 7(D) compares the correlation between cathodic peak height from the TPE sensor measurement and the readout of a commercial O_2 sensor vs. sparging time. As the buffer is sparged with N_2, the dissolved O_2 concentration decreases. The current decreases as expected with sparging time until 15 min where the O_2 appears to be fully depleted. These data are consistent with the results from the commercial O_2 sensor, shown in the same plot, and the TPE sensor even has smaller error than the commercial sensor at many of the points. These results show great potential for ability to quantitatively detect O_2 and are consistent with other carbon electrodes that involve more complex modification for O2 detection.[112-116]

To demonstrate the utility with microfluidic devices, the reported sensor module with PS-based TPEs was used to detect H_2O_2 in flow. Figure 8(A) shows a representative amperogram for injections of different H_2O_2 concentrations at a 1.0 mL/min flow rate. Distinct signal responses can be seen for the varying concentration peaks. The relatively high flow rate and length of measurement (over 60 min) without leaks demonstrates the effectiveness of the reversible seal from the magnets. Figure 8(A) also shows the relative stability of the PS-based TPEs over a continuous 60+ min measurement. Even near the end of the measurement, the current still returns

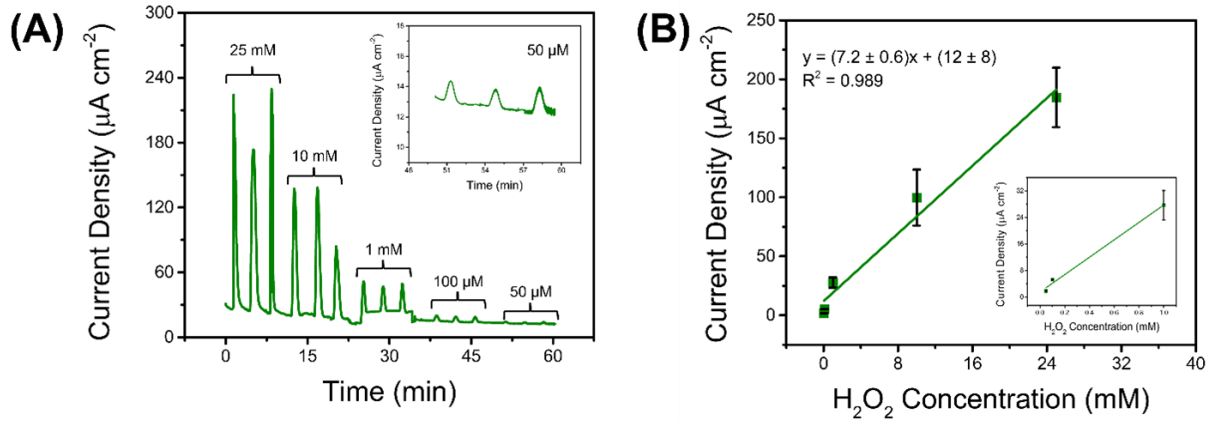

Figure 2.8: H_2O_2 Sensing Within Sensor Module V2 (A) Amperogram showing changes in current density measured the sensor module with sanded PS-based TPEs as three additions each of 25 mM, 10 mM, 1 mM, 100 μM, and (inset) 50 μM H2O2 were measured across 60 min. **(B)** Corresponding plot of peak current density vs. concentration from amperogram with (inset) zoom on lower concentrations. Symbols and error bars represent average and standard deviation of baseline subtracted peak current (n=3). Potential was held at +0.6 V vs. Ag|AgCl reference. Flow rate was 1.0 mL/min.

to the approximate baseline. Figure 8(B) shows the corresponding plot of peak currents from the amperogram showing the linear sensor response. The inconsistencies in peaks, baseline, and current response could be a result of manual valve and pump changing. This proof-of-concept indicates the potential for this system to be used for enzymatic sensing in flow.

2.4.6 Proof-of-Concept Microbiome Analysis within Gut Tissue Device

Results from our previous study[41] confirmed the presence of Gram-positive and Gram-negative bacteria in ex vivo murine colon explants after 72 h in the device and demonstrated that an oxygen gradient is necessary for preservation of a physiologically relevant bacterial community. To identify species within the microbial populations, luminal colon swabs were collected before and after experiments to examine the microbiome of intestinal tissue before ex vivo studies and then sampling tissue microbiome after time ex vivo. Feces were also collected immediately before dissection of tissue to insert in device. DNA was then extracted from the swabs and feces to sequence them for the V4 region of the 16S rRNA gene. Genomic DNA was extracted using MP Biomedicals Fast DNA Spin Kit for Soil (116560-200) according to the manufacturer's protocol. To ensure samples had adequate concentrations of DNA, PCR amplification using 515-806 primers was performed. Following PCR amplification, bead clean-up for DNA purification was performed to ensure samples contained only bacterial DNA. Purified DNA was quantified by Qubit with final concentrations around 2-14ng/μL. Samples were stored at -20ºC and sent to the University of Colorado Anschutz Center for Microbiome Excellence for processing including, library preparation, library quantification, and 16S amplicon sequencing. We are still deciphering all the nuances from the different groups that were compared, but there was no significant difference in the composition of the microbiome from native samples and samples collected after being in the device for 72h (Figure 9). This indicates that the device provides an environment that is reasonably comparable to an in vivo environment.

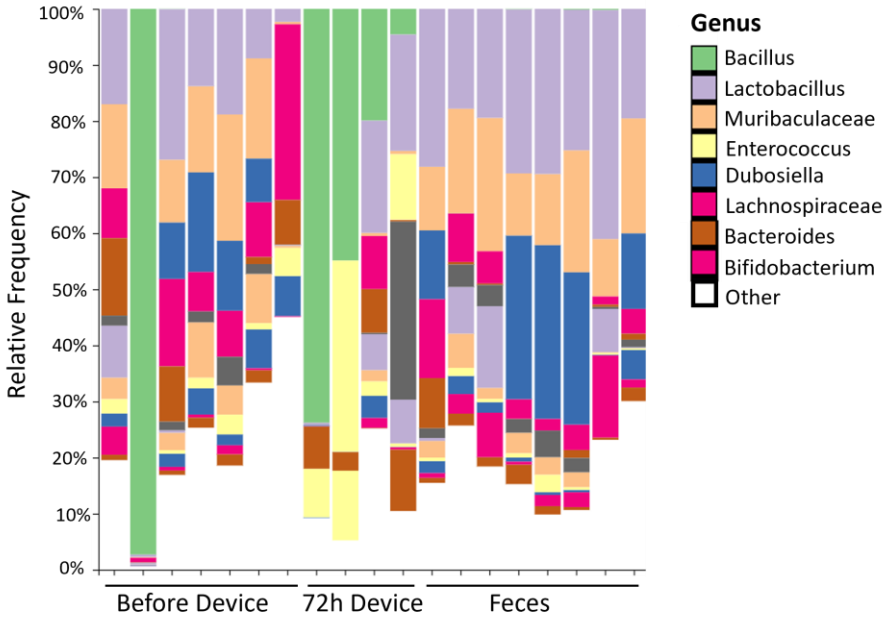

Figure 2.9: Identifying Microbiome Genus through 16s Gene Sequencing Overview of microbial populations obtained via swabs of colon tissue swabs either before placement in the device, after 72 h in the device, or from fecal pellets in the colon immediately after the animal was

2.5 Conclusions and Outlook

The organotypic microfluidic device in the current study preserved intestinal health and morphology indicated by labeling of neurons, epithelial cells, and immune cells comparable to in vivo tissue. Importantly, the device maintained tissue health and barrier function over 72 h without inhibiting muscle contractions with nicardipine. This model provides novel opportunities to examine the intestinal barrier ex vivo to better understand disease states associated with leaky gut. The penetration of fluorescent molecules into the mucosa of collagenase-treated tissue suggests that collagenase increased epithelial barrier permeability. This is supported by the decrease in claudin-1 (tight junction) immunoreactivity suggestive of increased paracellular permeability and alterations to type 1 collagen (COL-1) structure, where collagenase-treated tissue showed increased COL-1 tortuosity and decreased vertical crimping indicative of extracellular matrix fragility. We also observed marked differences in goblet cells, where exposure to collagenase

appears to disrupt the morphology and decrease apical mucin 2 immunoreactivity. Changes in shape and content of goblet cells likely affect the thickness of the mucus layer, further compromising the integrity of the intestinal barrier.

While bacterial collagenase altered epithelial and mucosal barrier structure, it is important to understand how these changes in barrier function may lead to disease states. The results outlined here demonstrate that this system works to recreate the effects of a leaky gut, in terms of physiologic hallmarks such as increased epithelial permeability. While the data doesn't identify the mechanistic causes of leaky gut, it has laid a foundation for future work to expand upon to address the problem from a more causative perspective. Here we have also shown preliminary confirmation that we are maintaining a microbial population within the tissue in our device over 72 h. We will use these sequences to continue identifying microbes present within each sample as we have done previously.[117] Future experiments will be able to investigate the effects of specific microbiome components (e.g., bacteria) that secrete collagenases, such as *Enterococcus faecalis*,[118] within the tissue to gain a more comprehensive understanding of the mechanisms involved in leaky gut. In the longer run, investigations of the impact of leaky gut on colon tissue ex vivo will allow for detailed studies of neuronal and immune cell populations that could lead to a better understanding of the steps leading to problematic pathology.

We have also shown a comparison of the electrochemical properties of TPEs with two different binders (PCL and PS). The sanded PS-based TPEs demonstrated increased electroactivity compared to the other TPEs. The PS-based TPEs were used to detect H_2O_2 and O_2 without any electrode modification. The PS-based TPEs were also integrated into a reversibly sealed fluidic sensor module device in which detection of H_2O_2 demonstrated in flow. The design of the sensor

module allows for simple electrode integration and assembly that can be coupled with a variety of fluidic systems.

Ultimately, we hope to make this system translational to humans to further understanding of intestinal disease processes. Pig intestine is similar to human intestinal tissue in size and structure, so a series of preliminary experiments were performed with pig intestine using the intestinal microfluidic devvice. Compared to mouse intestine, pig intestine is much thicker resulting in substantially stronger muscle contractions. Unfortunately, these contractions pulled the tissue out of the device. When we removed the muscle layer, we were able to keep pig intestine flat and alive for 72 h. However, this is not ideal as many enteric neurons and some immune cells reside in the muscle layers. Long-term goals include improving the mechanisms for clamping stronger, thicker tissue within the device so that similar studies can be performed with completely intact porcine and human tissue explants. We have previously obtained human tissue explants to study,[117] so future iterations of the device could very realistically include human tissue for more translatable studies. Expansion on the data collected using the sensor module will make it more viable for use downstream of the tissue device. The proof-of-concept detecting H_2O_2 with the sensor module will work towards a system for simple enzymatic detection of various biomolecules such as lactate and glucose in complex biological environments by incorporating an additional flow path with an oxidase enzyme. Results from future studies will be essential to enhance understanding of human gut health.

References

1. A. E. Cherwin, H. N. Templeton, A. T. Ehrlich, B. H. Patlin, C. S. Henry and S. A. Tobet, *Lab on a Chip*, 2023, **23**, 4126-4133.
2. A. Roley, K. Clark, A. Richardson, B. Martinez, S. Tobet and C. Henry, *ChemRxiv*, 2021, **1**.
3. C. Stolfi, C. Maresca, G. Monteleone and F. Laudisi, *Biomedicines*, 2022, **10**, 289.
4. A. S. Stewart, S. Pratt-Phillips and L. M. Gonzalez, *Journal of Equine Veterinary Science*, 2017, **52**, 10-22.
5. M. Vancamelbeke and S. Vermeire, *Expert Review of Gastroenterology & Hepatology*, 2017, **11**, 821-834.
6. W. M. Miner-Williams and P. J. Moughan, *Nutrition Research Reviews*, 2016, **29**, 40-59.
7. S. S. Ghosh, J. Wang, P. J. Yannie and S. Ghosh, *Journal of the Endocrine Society*, 2020, **4**.
8. J. M. Wells, O. Rossi, M. Meijerink and P. v. Baarlen, *PNAS*, 2010, **108**, 4607-4614.
9. Y. Guo, X. Chen, P. Gong, G. Li, W. Yao and W. Yang, *International Journal of Molecular Sciences*, 2023, **24**, 4089.
10. S. Yang and M. Yu, *Journal of Inflammation Research*, 2021, **14**, 3171-3183.
11. A. Michielan and R. D'Incà, *Mediators of Inflammation*, 2015, DOI: 10.1155/2015/628157.
12. L. Antoni, S. Nuding, J. Wehkamp and E. F. Stange, *World Journal of Gastroenterology*, 2014, **20**, 1165-1179.
13. S. Jäger, E. F. Stange and J. Wehkamp, *Langenbeck's Archives of Surgery*, 2013, **398**, 1-12.
14. M.C. Houser and M. G. Tansey, *NPJ Parkinson's Dis*, 2017, DOI: 10.1038/s41531-016-0002-0.
15. S. Ryman, A. A. Vakhtin, S. P. Richardson and H. C. Lin, *Journal of Neurology*, 2023, **270**, 746-758.
16. S. Min, N. Than, Y. C. Shin, G. Hu, W. Shin, Y. M. Ambrosini and H. J. Kim, *Scientific Reports*, 2022, **12**.
17. C. Liu, Y. Qu, Y. Luo and N. Fang, *ELECTROPHORESIS*, 2011, **32**, 3308-3318.
18. A. H. C. Ng, U. Uddayasankar and A. R. Wheeler, *Analytical and Bioanalytical Chemistry*, 2010, **397**, 991-1007.
19. T. Ozer, C. McMahon and C. S. Henry, *Annual Review of Analytical Chemistry*, 2020, **13**, 85-109.
20. S. N. Bhatia and D. E. Ingber, *Nature Biotechnology*, 2014, **32**, 760-772.
21. I. C. Samper, S. A. N. Gowers, M. L. Rogers, D. R. K. Murray, S. L. Jewell, C. Pahl, A. J. Strong and M. G. Boutelle, *Lab Chip*, 2019, **19**, 2038-2048.
22. A. Waldbaur, H. Rapp, K. Länge and B. E. Rapp, *Analytical Methods*, 2011, **3**.
23. L. H. Duong and P.-C. Chen, *Biomicrofluidics*, 2019, **13**.
24. S. Takenaga, B. Schneider, E. Erbay, M. Biselli, T. Schnitzler, M. J. Schöning and T. Wagner, *Physica Status Solidi (a)*, 2015, **212**, 1347-1352.
25. M. J. Beauchamp, G. P. Nordin and A. T. Woolley, *Analytical and Bioanalytical Chemistry*, 2017, **409**, 4311-4319.
26. C. S. Carrell, C. P. McCord, R. M. Wydallis and C. S. Henry, *Analytica Chimica Acta*, 2020, **1124**, 78-84.

27. Y. Temiz, R. D. Lovchik, G. V. Kaigala and E. Delamarche, *Microelectronic Engineering*, 2015, **132**, 156-175.
28. C. M. Leung, P. d. Haan, K. Ronaldson-Bouchard, G.-A. Kim, J. Ko, H. S. Rho, Z. Chen, P. Habibovic, N. L. Jeon, S. Takayama, M. L. Shuler, G. Vunjak-Novakovic, O. Frey, E. Verpoorte and Y.-C. Toh, *Nature Reviews Methods Primers*, 2022, **2**.
29. S. K. Srivastava, G. W. Foo, N. Aggarwal and M. W. Chang, *Biotechnology Notes*, 2024, **5**, 8-12.
30. I. C. McLean, L. A. Schwerdtfeger, S. A. Tobet and C. S. Henry, *Lab on a Chip*, 2018, **18**, 1399-1410.
31. A. Damerau and T. Gaber, *International Journal of Molecular Sciences*, 2020, **21**.
32. I. R. Powley, M. Patel, G. Miles, H. Pringle, L. Howells, A. Thomas, C. Kettleborough, J. Bryans, T. Hammonds, M. MacFarlane and C. Pritchard, *British Journal of Cancer*, 2020, **122**, 735-744.
33. P. d. Haan, M. J. C. Santbergen, M. v. d. Zande, H. Bouwmeester, M. W. F. Nielen and E. Verpoorte, *Nature Scientific Reports*, 2021, **11**.
34. H. J. Kim, D. Huh, G. Hamilton and D. E. Ingber, *Lab on a Chip*, 2012, **12**, 2165-2174.
35. K. Kulthong, L. Duivenvoorde, B. Z. Mizera, D. Rijkers, G. t. Dam, G. Oegema, T. Puzyn, H. Bouwmeester and M. v. d. Zande, *RSC Advances*, 2018, **8**, 32440-32453.
36. M. B. Esch, J. H. Sung, J. Yang, C. Yu, J. Yu, J. C. March and M. L. Shuler, *Biomedical Microdevices*, 2012, **14**, 895-906.
37. W. Shin and H. J. Kim, *PNAS*, 2018, **115**, E10539-E10547.
38. K.-Y. Shim, D. Lee, J. Han, N.-T. Nguyen, S. Park and J. H. Sung, *Biomed Microdevices*, 2017, **19**, 1-10.
39. B. Sidar, B. R. Jenkins, S. Huang, J. R. Spence, S. T. Walk and J. N. Wilking, *Lab on a Chip*, 2019, **19**, 3552-3562.
40. H. E. Amirabadi, J. M. Donkers, E. Wierenga, B. Ingenhut, L. Pieters, L. Stevens, T. Donkers, J. Westerhout, R. Masereeuw, I. Bobeldijk-Pastorova, I. Nooijen and E. v. d. Steeg, *Lab on a Chip*, 2022, **22**, 326-342.
41. A. Richardson, L. A. Schwerdtfeger, D. Eaton, I. Mclean, C. S. Henry and S. A. Tobet, *Analytical Methods*, 2020, **12**, 297-303.
42. C. M. Leung, P. d. Haan, K. Ronaldson-Bouchard, G.-A. Kim, J. Ko, H. S. Rho, Z. Chen, P. Habibovic, N. L. Jeon, S. Takayama, M. L. Shuler, G. Vunjak-Novakovic, O. Frey, E. Verpoorte and Y.-C. Toh, *Nature Reviews*, 2022, **2**, 1-29.
43. R. K, *Biosensors Journal*, 2017, **06**.
44. P. Shah, J. V. Fritz, E. Glaab, M. S. Desai, K. Greenhalgh, A. Frachet, M. Niegowska, M. Estes, C. Jäger, C. Seguin-Devaux, F. Zenhausern and P. Wilmes, *Nature Communications*, 2016, **7**.
45. M.-H. Wu, J.-L. Lin, J. Wang, Z. Cui and Z. Cui, *Biomedical Microdevices*, 2009, **11**, 265-273.
46. Z. Lin, T. Cherng-Wen, P. Roy and D. Trau, *Lab on a Chip*, 2009, **9**, 257-262.
47. S. Prill, M. S. Jaeger and C. Duschl, *Biomicrofluidics*, 2014, **8**.
48. Y. Wei, Y. Jiao, D. An, D. Li and Q. Wei, *Sensors*, 2019, **19**.
49. L. Rivas, S. Dulay, S. Miserere, L. Pla, S. B. Marin, J. Parra, E. Eixarch, E. Gratacós, M. Illa, M. Mir and J. Samitier, *Biosensors and Bioelectronics*, 2020, **1**.
50. Y. Triana, G. Ogata, M. Tomisaki, Irkham and Y. Einaga, *Anal Chem*, 2022, **94**, 3948-3955.

51. W. Preidel, J. R. Rao, K. Mund, O. Schunck and E. David, *Sensors and Actuators B: Chemical*, 1995, **28**, 71-74.
52. W. Chen, S. Cai, Q.-Q. Ren, W. Wena and Y.-D. Zhao, *Analyst*, 2012, **137**, 49-58.
53. I. S. Hosu, Q. Wang, A. Vasilescu, S. F. Peteu, V. Raditoiu, S. Railian, V. Zaitsev, K. Turcheniuk, Q. Wang, M. Li, R. Boukherrouba and S. Szunerits, *RSC Advances*, 2015, **5**, 1474-1484.
54. H. Wang, Y. Bu, W. Dai, K. Li, H. Wang and X. Zuo, *Sensors and Actuators B: Chemical*, 2015, **216**, 298-306.
55. K. J. Klunder, Z. Nilsson, J. B. Sambur and C. S. Henry, *J Am Chem Soc*, 2017, **139**, 12623-12631.
56. K. J. Klunder, K. M. Clark, C. McCord, K. E. Berg, S. D. Minteer and C. S. Henry, *Lab on a Chip*, 2019, **19**, 2589-2597.
57. E. Noviana, K. J. Klunder, R. B. Channon and C. S. Henry, *Anal Chem*, 2019, **91**, 2431-2438.
58. K. E. Berg, Y. R. Leroux, P. Hapiot and C. S. Henry, *ChemElectroChem*, 2019, **6**, 4811-4816.
59. L. A. Pradela-Filho, E. Noviana, D. A. G. Araújo, R. M. Takeuchi, A. L. Santos and C. S. Henry, *ACS Sensors*, 2020, **5**, 274-281.
60. K. M. Clark and C. S. Henry, *Electroanalysis*, 2021, **34**, 1869-1876.
61. C. P. McCord, B. Summers and C. S. Henry, *Electrochimica Acta*, 2021, **393**.
62. C. P. McCord, B. Summers and C. S. Henry, *ChemElectroChem*, 2022, **9**.
63. K. E. Berg, K. M. Clark, X. Li, E. M. Carter, J. Volckens and C. S. Henry, *Atmospheric Environment*, 2020, **222**.
64. L. F. d. Lima, A. d. S. M. d. Freitas, A. L. Ferreira, C. C. Maciel, M. Ferreira and W. R. d. Araujo, *Sensors and Actuators Reports*, 2022, **4**.
65. Y. K. Lee, *Energies*, 2019, **12**.
66. Y. Wang, D. Dang, D. Li, J. Hu, X. Zhan and Y.-T. Cheng, *Journal of Power Sources*, 2019, **438**.
67. M. Labet and W. Thielemans, *Chemical Society Reviews*, 2009, **38**, 3484-3504.
68. M. A. Woodruff and D. W. Hutmacher, *Progress in Polymer Science*, 2010, **35**, 1217-1256.
69. E. Malikmammadov, T. E. Tanir, A. Kiziltay, V. Hasirci and N. Hasirci, *Journal of Biomaterials Science, Polymer Edition*, 2018, **29**, 863-893.
70. K. Salminen, P. Grönroos, J. Eskola, E. Nieminen, H. Härmä and S. Kulmala, *Electrochimica Acta*, 2018, **282**, 147-154.
71. D. A. Jose, P. Prakash and P. Baby Chakrapani, in *Micro-and Nano-containers for Smart Applications*, Springer, 2022, pp. 179-195.
72. K. Salminen, P. Grönroos, S. Tuomi and S. Kulmala, *Analytica chimica acta*, 2017, **985**, 54-60.
73. C. Fernandez-Sanchez, E. Pellicer, J. Orozco, C. Jimenez-Jorquera, L. M. Lechuga and E. Mendoza, *Nanotechnology*, 2009, **20**.
74. H. Quan, S.-U. Park and J. Park, *Electrochimica Acta*, 2010, **55**, 2232-2237.
75. J. Orozco, C. Fernandez-Sanchez, E. Mendoza, M. Baeza, F. Cespedes and C. Jimenez-Jorquera, *Analytica Chimica Acta*, 2008, **607**, 176-182.
76. L. Saghatforoush, M. Hasanzadeh and N. Shadjou, *Chinese Chemical Letters*, 2014, **25**, 655-658.

77. W. Liu, J. Xiao, C. Wang, H. Yin, H. Xie and R. Cheng, *Materials Letters*, 2013, **100**, 70-73.
78. A. R. Khaskheli, J. Fischer, J. Barek, V. Vyskocil, Sirajuddin and M. I. Bhanger, *Electrochimica Acta*, 2013, **101**, 238-242.
79. Y. Lu, X. Wang, D. F. Chen and G. Chen, *Electrophoresis*, 2011, **32**, 1906-1912.
80. A. M. Surkov, R. G. Queiroz, R. S. Rinco, A. G. Rios, I. G. Gutz, A. L. Baccaro and L. Angnes, *Talanta*, 2021, **223**, 121780.
81. Z. Rymansaib, P. Iravani, E. Emslie, M. Medvidović-Kosanović, M. Sak-Bosnar, R. Verdejo and F. Marken, *Electroanalysis*, 2016, **28**, 1517-1523.
82. N. Promphet, P. Rattanarat, R. Rangkupan, O. Chailapakul and N. Rodthongkum, *Sensors and Actuators B-Chemical*, 2015, **207**, 526-534.
83. M. Gutiérrez-Capitán, A. Baldi, R. Gómez, V. García, C. Jiménez-Jorquera and C. s. Fernández-Sánchez, *Analytical chemistry*, 2015, **87**, 2152-2160.
84. J. Xu, H. Zhang and G. Chen, *Talanta*, 2007, **73**, 932-937.
85. Y. S. Zhang, J. Aleman, S. R. Shin, T. Kilic, D. Kim, S. A. Mousavi Shaegh, S. Massa, R. Riahi, S. Chae, N. Hu, H. Avci, W. Zhang, A. Silvestri, A. Sanati Nezhad, A. Manbohi, F. De Ferrari, A. Polini, G. Calzone, N. Shaikh, P. Alerasool, E. Budina, J. Kang, N. Bhise, J. Ribas, A. Pourmand, A. Skardal, T. Shupe, C. E. Bishop, M. R. Dokmeci, A. Atala and A. Khademhosseini, *Proc Natl Acad Sci U S A*, 2017, **114**, E2293-E2302.
86. X. Li and C. J. Easley, *Analytical and Bioanalytical Chemistry*, 2018, **410**, 791-800.
87. J. L. Erkal, A. Selimovic, B. C. Gross, S. Y. Lockwood, E. L. Walton, S. McNamara, R. S. Martin and D. M. Spence, *Lab on a chip*, 2014, **14**, 2023-2032.
88. A. S. Duarte, A. Caorreia and A. C. Esteves, *Critical Reviews in Microbiology*, 2016, **42**, 106-126.
89. N. L. Walker and J. E. Dick, *Analytical chemistry*, 2021, **93**, 10065-10074.
90. P. W. Ruch, D. Cericola, M. Hahn, R. Kötz and A. Wokaun, *Journal of Electroanalytical Chemistry*, 2009, **636**, 128-131.
91. S. Park, H. J. Chun, Y. D. Kwon, B. Keum, Y. S. Seo, Y. S. Kim, Y.-T. Jeen, S. H. Um, C. D. Kim, H. S. Ryu, J. H. Lee and Y.-s. Chae, *Gut and Liver*, 2008, **2**, 199-204.
92. K. J. Klunder, Z. Nilsson, J. B. Sambur and C. S. Henry, *J. Am. Chem. Soc.*, 2017, **139**, 12623-12631.
93. S. G. Lemay, D. M. van den Broek, A. J. Storm, D. Krapf, R. M. Smeets, H. A. Heering and C. Dekker, *Analytical chemistry*, 2005, **77**, 1911-1915.
94. D. Cooper and M. Dimri, *Journal*, 2022.
95. N. Prasadarao, S. A. Tobet and F. B. Jungalwala, *The Journal of Histochemistry and Cytochemistry*, 1990, **38**, 1193-1200.
96. D. Hollander, *Current Gastroenterology Reports*, 1999, **1**, 410-416.
97. V. Garcia-Hernandez, M. Quiros and A. Nusrat, *Annals of the New York Academy of Sciences*, 2017, **1397**, 66-79.
98. B. J. Saeedi, D. J. Kao, D. A. Kitzenberg, E. Dobrinskikh, K. D. Schwisow, J. C. Masterson, A. A. Kendrick, C. J. Kelly, A. J. Bayless, D. J. Kominsky, E. L. Campbell, K. A. Kuhn, G. T. Furuta, S. P. Colgan and L. E. Glover, *Molecular Biology of the Cell*, 2015, **26**, 2151-2384.
99. M. Furuse, M. Hata, K. Furuse, Y. Yoshida, A. Haratake, Y. Sugitani, T. Noda, A. Kubo and S. Tsukita, *Journal of Cell Biology*, 2002, **156**, 1099-1111.
100. A. Derkacz, P. Olczyk, K. Olczyk and K. Komosinska-Vassev, *J Clin Med*, 2021, **10**, 1122.

101. T. R. Cox and J. T. Erler, *Dis Model Mech*, 2011, **4**, 165-178.
102. C. Zhu, L. Yin, J. Xu, X. Yang, H. Wang, X. Xiang, H. Liu and K. Liu, *Biomolecules*, 2022, **12**, 1683.
103. H. C. Han, *J Vasc Res*, 2012, **49**, 185-197.
104. J. Xu and G. P. Shi, *Biophys Acta*, 2014, **1842**, 2106-2119.
105. Y. S. Kim and S. B. Ho, *Curr Gastroenterol Rep*, 2010, **12**, 319-330.
106. M. Sajid, N. Baig and K. Alhooshani, *TrAC Trends in Analytical Chemistry*, 2019, **118**, 368-385.
107. R. Aguilar, M. Davila, M. Elizalde, J. Mattusch and R. Wennrich, *Electrochimica acta*, 2004, **49**, 851-859.
108. P.-Y. Chen, R. Vittal, P.-C. Nien and K.-C. Ho, *Biosensors and Bioelectronics*, 2009, **24**, 3504-3509.
109. S. Cheemalapati, S. Palanisamy, V. Mani and S.-M. Chen, *Talanta*, 2013, **117**, 297-304.
110. M. Khan, *Journal of Nanomaterials*, 2017, **2017**.
111. M. Kumar, B. K. Swamy, S. Reddy, W. Zhao, S. Chetana and V. G. Kumar, *Journal of Electroanalytical Chemistry*, 2019, **835**, 96-105.
112. Y. Wei, Y. Jiao, D. An, D. Li, W. Li and Q. Wei, *Sensors*, 2019, **19**, 3995.
113. H.-F. Cui, J.-S. Ye, W.-D. Zhang, J. Wang and F.-S. Sheu, *Journal of Electroanalytical Chemistry*, 2005, **577**, 295-302.
114. C. López-Gándara, F. M. Ramos and A. Cirera, *Journal of Sensors*, 2009, **2009**.
115. S. Jose, R. Rajeev, D. A. Thadathil, A. Varghese and G. Hegde, *Journal of Science: Advanced Materials and Devices*, 2022, 100460.
116. L. Liu, L.-p. Guo, X.-j. Bo, J. Bai and X.-j. Cui, *Analytica chimica acta*, 2010, **673**, 88-94.
117. L. A. Schwerdtfeger, N. J. Nealon, E. P. Ryan and S. A. Tobet, *PLoS One*, 2019, **14**.
118. B. D. Shogan, N. Belogortseva, P. M. Luong, A. Zaborin, S. Lax, C. Bethel, M. Ward, J. P. Muldoon, M. Singer, G. An, K. Umanskiy, V. Konda, B. Shakhsheer, J. Luo, R. Klabbers, L. E. Hancock, J. Gilbert, O. Zaborina and J. C. Alverdy, *Science Translational Medicine*, 2015, **7**.

Chapter 3 – Low-Cost, Noninvasive Monitoring of Heart Failure via a Point-of-Care Microfluidic Device

3.1 Overview

The goal of this chapter is to describe the development of a multiplexed microfluidic electrochemical biosensor for the detection of novel salivary heart failure (HF) biomarkers galectin-3 (Gal-3) and S100A7 from a saliva sample. Preliminary work on this project was published by my colleague Trey Pittman in *Sensors and Actuators B:Chemical*[1] and *Theranostics*.[2] The work presented in this chapter was completed in collaboration with Trey Pittman and Ítalo Bezerra of the Henry Group at Colorado State University.

3.2 Introduction

The leading cause of death worldwide is ischemic heart disease, one of the most common causes of HF.[3, 4] HF is a condition in which the heart cannot pump enough blood to meet the body's needs.[5] In the United States, HF prevalence has increased from ~6 million to ~6.7 million Americans above the age of 20 from 2018-2020.[6] As of right now HF has no cure and so it continues to be a heavy burden on the healthcare system, with estimated costs of $30.7 billion in 2012[7] and projected costs of $69.8 billion by 2030 (~$244 for every adult in the U.S.).[6] This burden is especially felt in rural communities and underrepresented racial and ethnic groups, where hospitalizations[8] and mortality rates[9] continue to increase. This disparity among populations is in part due to the high cost and low accessibility of current HF diagnostic methods, which often require laboratory-based blood tests or sophisticated equipment such as X-rays or an electrocardiogram (EKG).[10] One laboratory-based method used in medical diagnostics is the

Enzyme-Linked Immunosorbent Assay, or ELISA. Traditional laboratory ELISAs have high sensitivity and specificity which make them excellent for diagnostics, but they are costly in terms of time and resources and must be performed by trained personnel.[11] There exists a clear need for a more affordable test for HF that can be made available at the Point-of-Care (POC) in rural and low-income communities.[1]

Electrochemical immunoassays[12-14] function similarly to an ELISA, but mainly base quantification of the target biomarker on the electrochemical detection of a labeled marker such as an enzyme. Electrochemical immunoassays have previously been developed on paper-based[15] and other low-cost materials[16] with high detection sensitivity. My colleagues Trey Pittman and Ítalo Bezerra developed two foundational electrochemical immunoassays to detect HF biomarkers Galectin-3(Gal-3) and S100A7. Gal-3 and S100A7 are novel salivary HF biomarkers initially discovered in serum[17] of HF patients and were later confirmed to be present in their saliva as well.[18-20] Our collaborators, Drs. Xi Zhang and Chamindie Punyadeera of Griffith University in Australia first quantified Gal-3 and S100A7 in the saliva of healthy patients as well as those experiencing systolic HF. They identified a clinically relevant concentration range for each biomarker in HF saliva as well as a critical value above which the patient's survival rate was significantly decreased. For Gal-3, the critical value they determined is 172 ng/mL and for S100A7 it is 689 ng/mL. While these biomarkers have been identified, no POC assays exist for their measurement in rural and/or resource limited settings. The Henry Group has established the electrochemical capillary driven immunoassay (eCaDI) as a fast, accurate, and low-cost diagnostic test for SARS-CoV-2.[16] We aimed to adapt the eCaDI system into a new device for multiplexed detection of the two salivary HF biomarkers. For the success of the POC device described in this chapter, it must be able to clearly distinguish if one or both target biomarkers in a sample are above

or below their respective critical value. Initial validation of the immunoassay was performed in a static configuration, with a limit of detection of detection of 8.97 ng/mL in artificial saliva for Gal-3[1] and 39.0 ng/mL for S100A7. One of the key challenges with advancing this project from a static assay into the microfluidic device was understanding how to process saliva as a sample matrix.

Saliva is an appealing sample matrix for diagnostic devices because it is non-invasive and risk-free to collect.[2] This offers an improvement in the patient's quality of life as they don't need to constantly have blood drawn in order to monitor their disease prognosis. Saliva also requires less preprocessing than blood, which can reduce assay time.[2] Approximately 2000 unique proteins and peptides related to pathologies can be found in saliva;[18, 21-24] of those, roughly 27% of those are also found in blood.[24-26] There are still challenges associated with using saliva as a diagnostic matrix, such as the relatively low abundance of analytes compared to serum and plasma concentrations.[27, 28] Another challenge is the viscosity of saliva, which can vary in a single patient but also varies between patients.[29]

My work on this project was in the optimization of the microfluidic device so that it could successfully process viscous saliva samples while still quantifying the two HF biomarkers within their clinically relevant ranges. This chapter describes the changes made to channel geometries, sample and buffer volumes, and electrode configurations. I also created a new, simpler device to bridge the gap between the static assay and the fully assembled microfluidic device, referred to as the "straight channel device". At every stage in the optimization process electrochemical measurements were collected using either the straight channel device or the full eCaDI to verify the changes maintained appropriate sensitivity and specificity of the immunoassay.

3.3 Materials and Methods

3.3.1 Microfluidic Device Design

The previously developed eCaDI device for SARS-CoV-2 served as a starting point for our system as it uses capillary driven flow to sequentially deliver reagents of the immunoassay to a modified stencil-printed carbon electrode (SPCE) surface. Many changes were necessary to adapt the device to accommodate a saliva sample as opposed to a buffer sample, and two working electrodes (WEs) were needed for the multiplexed detection of both HF biomarkers from a single sample. The device requires two end user steps for the running buffer and the saliva sample, each with its own inlet (Figure 1, circular inlet for buffer and rectangular inlet for saliva). When the saliva sample is input, it rehydrates the detection antibody pad while the running buffer meets and rehydrates the substrate pad.

The fluidic device was designed using CorelDRAW (Corel, Ontario, Canada) and cut using a CO_2 laser cutter (Zing 10000, Epilog Laser) to pattern layers of polyethylene terephthalate (PET) films (9962) and 3M 468 double-sided adhesive (DSA) and the layers were sandwiched together. First, the bottom PET layer containing the functionalized electrode was secured onto the exposed DSA. After preparing both conjugate release pads, the pads were placed within the channels of the device at defined positions, and the cover layer was sealed on top. Devices were stored in the dark until being used for experiments because the TMB substrate is sensitive to light, per the vendor's SDS. Before use, a 17 mm diameter (shown in Figure 1(A)) Whatman 1 chromatography paper waste pad was inserted to the opening at the bottom of the device.

A simple straight channel microfluidic device was developed to optimize initial device conditions in flow without introducing the additional complexities that the fully assembled eCaDI would (e.g., dried reagents in waste pads, multiple flow channels, etc.). This straight channel device (Figure 1(B)) was used such that the previously optimized static assay protocol was performed on the electrode surface up to the detection antibody (D-Ab) step, then the electrode array was assembled into the device and the substrate was delivered and the measurement recorded in flow.

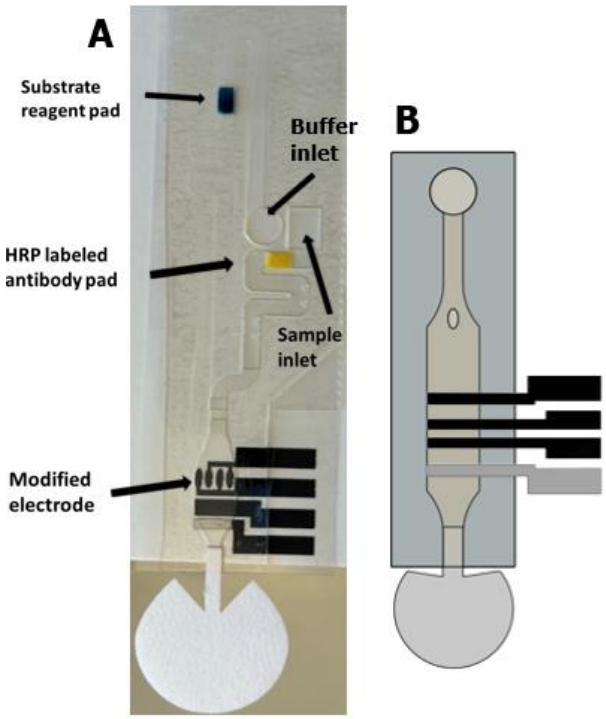

Figure 3.1. The microfluidic eCaDI device. (A) shows the fully assembled device with the reagent pads and waste pad in place. (B) shows a CAD rendering of the straight channel device used for intermediate optimization experiments.

3.3.2 Reagent Preparation and Experimental Flow

Phosphate-buffered saline (PBS) was prepared by dissolving a tablet (Research Products International, USA) in Milli-Q system water (MilliporeSigma, USA). 10 mM (1x) PBS was composed of 140 mM sodium chloride and 2.7 mM potassium chloride at pH 7.4. 100 mM (10x) PBS was composed of 1.4 M sodium chloride and 27 mM potassium chloride at pH 7.4. Capture

antibody was taken from a stock solution (Gal-3 C-Ab stock concentration = 1 mg/mL, S100A7 C-Ab stock concentration = mg/mL) and diluted in 1X PBS. Carboxymethylcellulose sodium salt (SCMC, Sigma Aldrich, USA) was dissolved in Milli-Q water to produce a solution that can mirror the viscosity of saliva, as reported previously.[25] Recombinant human Galectin-3 and S100A7 were both reconstituted in a 0.1% BSA solution in 1X PBS at a concentration of 50 µg/mL for Gal-3 and 500 µg/mL for S100A7 to make their stock solutions. These stock solutions were diluted in 10X PBS for experiments. Horseradish Peroxidase (HRP)-conjugated detection antibody was taken from a stock solution and diluted in 1X PBS (HRP-D-Ab for Gal-3 stock concentration = 0.84 .mg/mL, HRP-D-Ab for S100A7 stock concentration = 0.51 mg/mL). For flow studies, saliva samples were collected from colleagues within our group via passive drool collection and frozen at -20°C until use. Saliva samples were pooled before use in the flow studies.

For electrochemical measurements, a portable bipotentiostat (Palmsens4) was used to apply a 0.0 V potential to both WEs (vs the Ag|AgCl-painted reference electrode, RE) and the current was recorded between the working and the counter electrodes. Microsoft Excel (Microsoft, USA) software was used to identify the peak current from the amperometry data, which was later used for data analysis.

3.3.3 Electrode Fabrication and Modification

Stencils for electrode arrays were designed using computer-aided design (CAD) software Onshape (Onshape, USA) and laser cut out of low-tack adhesive. The stencil was then secured onto PET film and the electrodes were printed using carbon ink (Cl-2057, Engineered Materials Solutions, Inc.). Following printing, the ink was dried at 60°C, and once fully dry the low-tack stencil was carefully removed, leaving just the printed electrodes on the PET film. The reference

electrode was painted over with a thin layer of Ag|AgCl paste (Sigma-Aldrich). Before modification, each electrode array was sprayed three times with 1X PBS and left to dry.

For initial electrode comparison studies, The SPCEs were modified by dropcasting 5 µL of 4 ug/mL HRP-DAb on the working electrode, 2.5 µL per 'bubble' (Figure 1(A, modified electrode)). Electrodes were assembled into straight channel devices and a waste pad was inserted at the bottom. 65 µL of 80× diluted Great Value blue food dye in 1X PBS was added to the device and allowed to fill the bubble cell until reaching the waste pad. The amperometry measurement collection was started as soon as the buffer filled the bubble cell, then 50 µL of TMB solution was input into the device and allowed to flow into the cell and across the electrodes.

For the multiplexed detection assay, the SPCEs were modified by dropcasting 5 µL of 50 ug/mL capture antibody (C-Ab) on the working electrode, 2.5 µL per 'bubble' (Figure 1(A, modified electrode)). The C-Ab was dried on the electrodes in a partially covered petri dish at 37°C. Once dry, 2.5 µL of 1% bovine serum albumin (BSA) in PBS was dropped onto each electrode bubble and incubated for 30 min in a humidity chamber, then left to dry completely (~30 min) at room temperature to prevent non-specific adsorption to the electrode surface. 4 ug/mL of HRP-Dab diluted in 1X PBS was incubated with varying concentrations of its target antigen for 2 h on a rotator at room temperature. 5 µL of this pre-incubated antigen/D-Ab solution was deposited onto its respective working electrode (2.5 µL per 'bubble', Gal-3 was always WE1 and S100A7 was always WE2)

3.4 Results and Discussion

3.4.1 Microfluidic Channel Design Optimization

The evolution of the HF saliva eCaDI from the SARS-CoV-2 eCaDI is pictured in Figure 2, where the first version of the saliva eCaDI (Figure 2(A)) is shown next to the current version

(Figure 2(B)). The first change from the SARS-CoV-2 device was that the single sample and buffer input step was separated into two steps with independent inlets (Figure 2(A)); the saliva sample rehydrates the detection antibody pad, while the running buffer meets rehydrates the substrate pad. For multiplex detection in flow, we needed to restructure the electrode array to minimize crosstalk between the working electrodes (described in detail below, section **3.4.2**). To house the full electrode array, we created a "bubble cell" to increase the channel volume over the electrodes. The first design of the bubble cell is shown on the straight channel device (Figure 1(B). Optimization of the electrode array allowed us to decrease the bubble cell size to the design seen in Figure 2(B). The buffer channel volume is used to wash unbound material from the electrode surface before the substrate crosses over. Initial electrochemical measurements showed very high blank signals that were indistinguishable from positive samples, indicating this wash volume was insufficient to remove unbound material from our electrodes. The wash volume was increased by incorporating a serpentine channel (shown in Figure 2(B)) directly below the substrate pad, increasing the volume of wash buffer from 60 to 95 μL.

We observed that the viscous sample solution prevented flow from the detection antibody pad from evenly distributing within the bubble cell (the dye in the pad allows us to see the color distribution within the bubble cell). If the antibody-antigen complex does not evenly distribute across the working electrode surfaces, the resulting data could be biased toward a falsely negative result. To improve the uniformity of flow and distribution of electrodes we incorporated another short serpentine into the sample inlet channel (Figure 2(B)). The turns within the serpentine cause the dye to more evenly spread throughout the channel—suggesting that the antibodies and antigen from the sample will do the same.

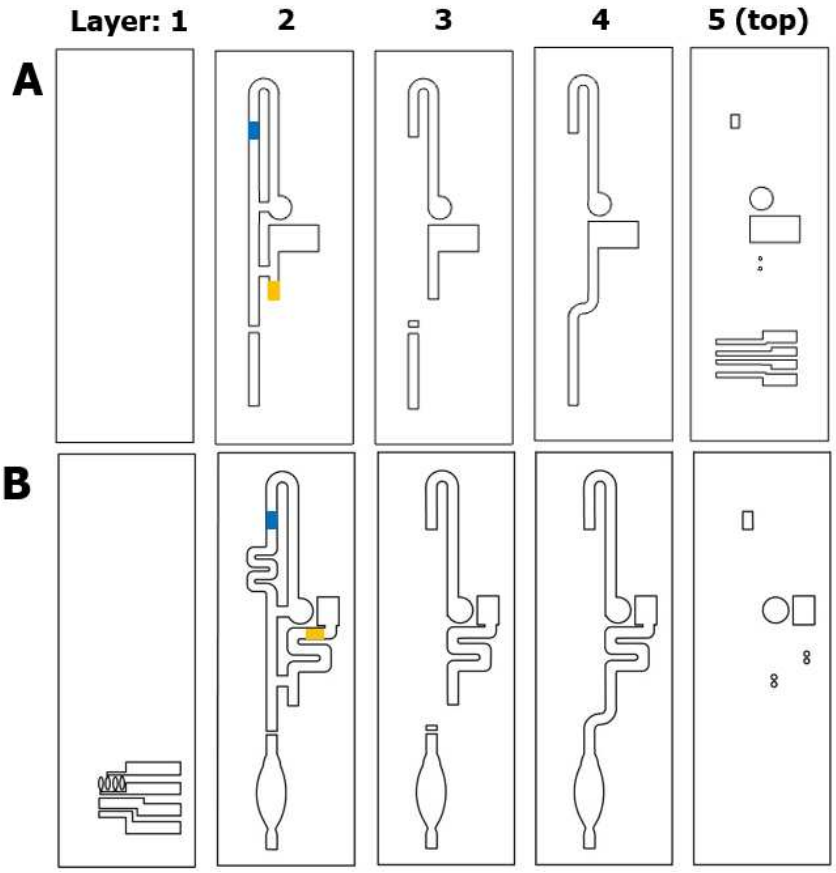

Figure 3.2. Microfluidic Device Design Evolution. (A) shows the first version of the saliva eCaDI, and (B) shows the most recent version. Layers 1-5 indicate alternating PET and DSA layers, with the bottom PET layer as layer 1. Blue and yellow rectangles in layer 2 represent the placement of the substrate and D-Ab pads, respectively. Each layer is a 115 mm x 38 mm rectangle.

3.4.2 Electrode Design Optimization

One of the first objectives in creating a flow device that can be used for multiplexed detection of two unique proteins was designing a compact electrode array that would minimize crosstalk between the working electrodes. New designs were created to put the working electrodes in parallel rather than in series. The first design created was to move the rectangular series electrodes onto opposing sides of the bubble cell (Figure 3(B)). Due to the flexible nature of the materials used to construct the device, this design folded in on itself as soon as the potentiostat clips were connected, quickly ruling it out. The ellipse or bubble shaped WE designs were inspired

by DropSens commercial electrodes (shown in Figure 3(G)). Designs with four bubbles (Figure 3(D)-(F)) were hypothesized to be more effective than the two bubble or two bar designs at providing consistent results in the event that flow in the bubble cell is nonuniform.

Figure 3 shows six different electrode arrays that were tested, including the series electrode configuration that was used for the static assay optimizations (Figure 3(A)) and a commercial 2-WE array. Figure 3(B)-(F) show five different parallel electrode arrays that were tested; the designs pictured in 3(C) and 3(E) were found to be the most compact and easy to manufacture, so they were chosen for further optimization studies.

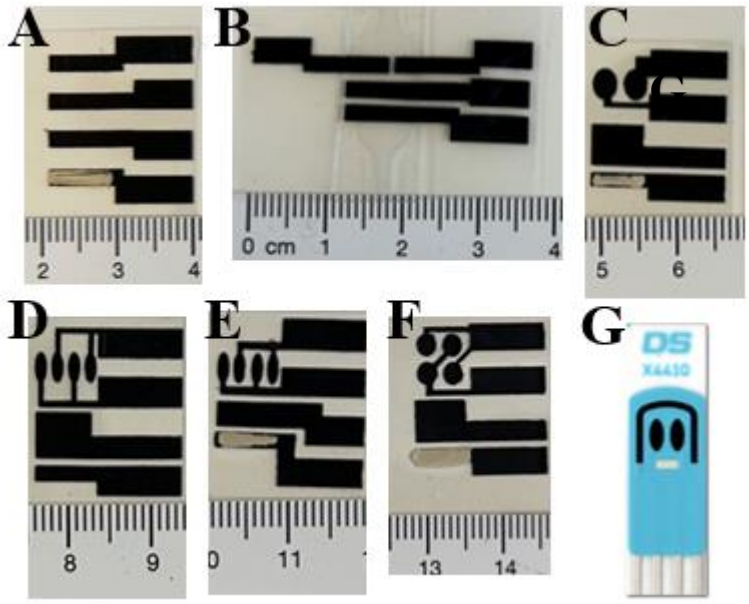

Figure 3.3. Surveyed Electrode Arrays. (A) shows the series electrode configuration that was used for the static electrochemical immunoassays (B)-(F) show parallel electrode configurations that were compared for flow assays. (G) Shows an electrode array by DropSens with two WEs that inspired some of the designs. Ruler shown is in cm.

Figure 4 shows an electrode array comparison where the top two electrode designs (Figure 3(C) and 3(E)) were compared to the series electrode design that was used for the static assay (Figure 3(A)). Either zero or one working electrode was modified on a given array with HRP-conjugated D-Ab and was assembled into a straight channel device as shown in Figure 1(B). As

expected, the series configuration showed the most crosstalk at WE2 when only WE1 was modified. Surprisingly, despite both WEs having identical geometric surface area, the signal generated at WE2 for the 2-bubble array (Figure 4(A)) was considerably higher than that generated at WE1. For this reason, we decided to proceed with further optimization of the device using the 4-electrode array shown in Figure 3(E) and Figure 4(B) which showed more consistency between the WEs.

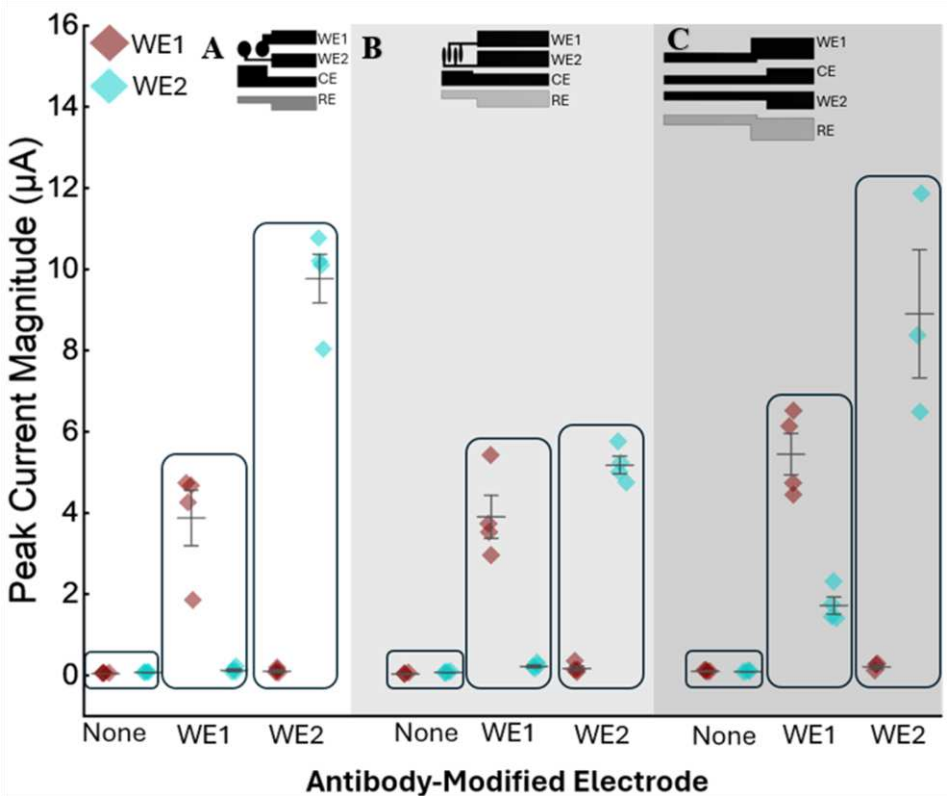

Figure 3.4. Electrode Array Comparison in Flow. (A) shows a 2-bubble array in parallel, (B) shows a 4-bubble, interdigitated array in parallel, (C) shows the series array used for static optimization. For (A) and (B) the geometric surface area of WE1 is equal to that of WE2.

3.4.3 Flow Study in the Full eCaDI

As previously mentioned, the viscous nature of saliva affected how it was able to flow in the capillary device and optimization of the device design was necessary to optimize uniformity of flow and the time it took for a full assay to be completed on the eCaDI (from the time the saliva

sample was input to the time the measurement would be recorded). A flow study was conducted to compare how two SCMC solutions (0.25% and 0.50%) to frozen pooled saliva diluted in two solutions of differing ionic strengths (1X or 5X PBS). Stock antigen solutions are a 1X PBS solution, but previous data from the static assay optimization showed that 5X PBS led to better signal separation between Gal-3 concentrations than 1X PBS,[1] so these two ionic strengths were compared in flow. Figure 5 shows that at lower ionic strengths the SCMC had a more striking effect on the viscosity of the solution and increased the assay time significantly, but at higher ionic strengths all the flow times for all solutions were similar. These results are consistent with literature suggesting that higher concentrations of sodium chloride in an SCMC solution decreases its viscosity.[30] This is likely because in the presence of low molecular weight ions, the ionized –COO groups on CMC chain are electrostatically shielded and the CMC chains then adapt a less expanded structure. The viscosities were thus reduced by the small ions, such as sodium cation and chloride anion.[30]

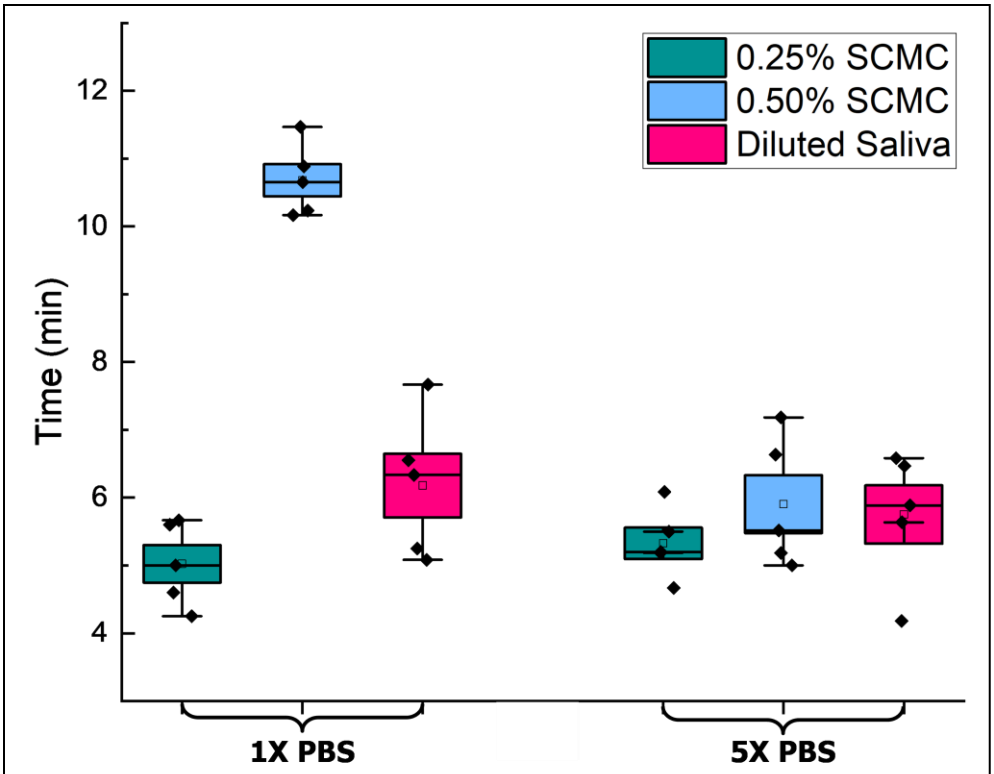

Figure 3.5. Flow Study. 0.25% SCMC, 0.50% SCMC, and frozen pooled saliva samples were diluted in either a 1X or 5X PBS buffer solution and used as the sample input on a full eCaDI device. Time on the y axis reflects the time between sample addition and when the measurement would be recorded (when the TMB crosses the working electrode surface).

3.4.4 Primary Validation of Multiplexed Assay

Once an optimal electrode configuration was determined (4-bubble interdigitated WE array), we began the preliminary validation of the multiplexed assay. Early experiments used only a single immunoassay with a 0.1% BSA blocker solution on the unmodified working electrode (e.g. anti-Gal-3 C-Ab on WE1, BSA on WE2), but the final assay configuration will have the opposite target's C-Ab on the other WE. The straight channel device was used for this first multiplexed detection study, where all devices' WE1 were modified with anti-Gal-3 C-Ab and all devices' WE2 were modified with anti-S100A7 C-Ab. The sample solutions were prepared such that one antigen was present at its critical concentration, and the other antigen concentration was varied from between a low, critical, and high concentration, the exact values are listed in Table 1.

Control samples were prepared with HRP-D-Ab but no antigen. Figure 6 shows the results from this multiplexed study. For both Gal-3 and S100A7 the blank average peak currents were lower than the positive samples. Gal-3 shows excellent signal separation between low and critical values, and all positive samples produced a higher current than the control (no antigen) sample. Measurements of the current with critical Gal-3 concentration and high S100A7 concentration showed a slightly decreased peak current magnitude for the critical Gal-3, compared to the other measurements with lower S100A7 concentrations. This signal may be limited by the amount of TMB present at each working electrode surface during data collection. S100A7 shows a clear difference in peak current magnitude at the high concentration compared to the lower concentrations. The average peak current magnitude for the critical S100A7 value is higher than the average peak current for the blank and low concentrations, but there is still considerable overlap between the error bars. More time has been spent optimizing the Gal-3 assay, so with comparable time spent on the S100A7 assay we expect the signal separation to improve and the error bars to decrease.

These results show great promise as a preliminary validation of the multiplexed system to build upon in future experiments. The peak current magnitude is relatively high compared to data we've seen with the SARS-CoV-2 electrochemical immunoassays,[16] so there may be room for improvement in signal separation at the lower antigen concentrations if we decrease the concentration of antibody (C-Ab, D-Ab, or both) and investigate other potential blockers for the electrode surface.

Table 1. Antigen Concentrations for Multiplexed Detection Experiment. Concentrations of Gal-3 and S100A7 used for the multiplexed detection. Values were chosen based on pre-determined critical values and concentration ranges provided by the Punyadeera Group.

Concentration	[Gal-3] (ng/mL)	[S100A7] (ng/mL)
Blank	0	0
Low	65	348
Critical	172	689
High	306	2600

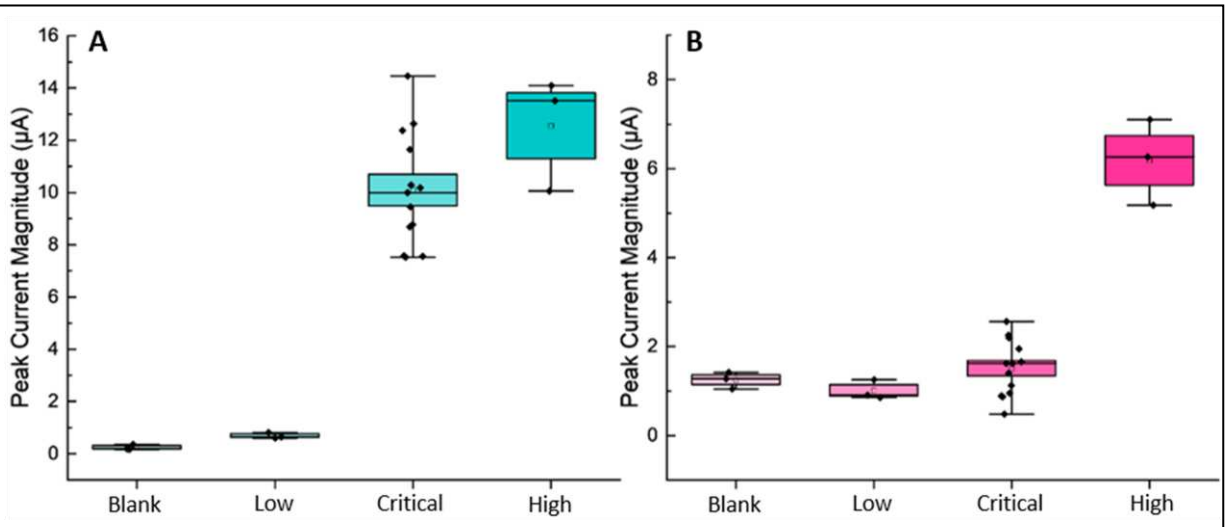

Figure 3.6. Multiplexed Detection in Straight Channel Device. (A) Peak current magnitude in flow for blank, low, critical, and high concentrations of Gal-3 are displayed. (B) Peak current magnitude in flow for blank, low, critical, and high concentrations of S100A7 are displayed. n=3 for low and high concentrations, n=6 for blank concentrations, n=13 for critical concentrations.

3.5 Conclusions and Outlook

The work described in this chapter has described the evolution of a static electrochemical immunoassay for the detection of HF biomarkers in saliva into a microfluidic device capable of multiplexed detection in flow. Optimization was done on many aspects of the device, from sample volumes to channel geometry to reagent concentrations. Preliminary data with the device demonstrated minimal crosstalk between WEs, and the ability to distinguish concentrations of two

HF biomarkers, Gal-3 and S100A7, in spiked buffer solutions. Current work aims to further optimize the S100A7 assay so that we can get clearer signal separation between the low and critical concentrations. A key next step is establishing the device's quantification capability in pooled saliva and addressing any complications that arise; flow study data and previous static assay calibration curves suggest that little optimization will be necessary when moving to the saliva matrix. Long-term goals include completing a human sample study with known HF patients' saliva. Successful correlation of the devices' results with clinical samples would vault this POC device into a marketable, usable product. This device could be distributed to clinics across the country and world, even in more resource-limited areas where residents lack access to sophisticated medical infrastructure. This device has the potential to be truly life-changing for millions of people who suffer from HF.

References

1. T. W. Pittman, X. Zhang, C. Punyadeera and C. S. Henry, *Sensors and Actuators B: Chemical*, 2024, **400**.
2. T. W. Pittman, D. B. Decsi, C. Punyadeera and C. S. Henry, *Theranostics*, 2023, **13**, 1091-1108.
3. J. S. Rana, S. S. Khan, D. M. Lloyd-Jones and S. Sidney, *J Gen Intern Med*, 2021, **36**, 2517-2518.
4. P. Severino, A. D'Amato, M. Pucci, F. Infusino, L. I. Birtolo, M. V. Mariani, C. Lavalle, V. Maestrini, M. Mancone and F. Fedele, *International journal of molecular sciences*, 2020, **21**, 3167.
5. L. National Heart, and Blood Institute (NHLBI), What is Heart Failure?, https://www.nhlbi.nih.gov/health/heart-failure#:~:text=Heart%20failure%2C%20also%20known%20as,too%20weak%20to%20pump%20properly.).
6. C. W. Tsao, A. W. Aday, Z. I. Almarzooq, C. A. M. Anderson, P. Arora, C. L. Avery, C. M. Baker-Smith, A. Z. Beaton, A. K. Boehme, A. E. Buxton, Y. Commodore-Mensah, M. S. V. Elkind, K. R. Evenson, C. Eze-Nliam, S. Fugar, G. Generoso, D. G. Heard, S. Hiremath, J. E. Ho, R. Kalani, D. S. Kazi, D. Ko, D. A. Levine, J. Liu, J. Ma, J. W. Magnani, E. D. Michos, M. E. Mussolino, S. D. Navaneethan, N. I. Parikh, R. Poudel, M. Rezk-Hanna, G. A. Roth, N. S. Shah, M.-P. St-Onge, E. L. Thacker, S. S. Virani, J. H. Voeks, N.-Y. Wang, N. D. Wong, S. S. Wong, K. Yaffe and S. S. Martin, *Circulation*, 2023, **147**, e93-e621.
7. P. A. Heidenreich, N. M. Albert, L. A. Allen, D. A. Bluemke, J. Butler, G. C. Fonarow, J. S. Ikonomidis, O. Khavjou, M. A. Konstam, T. M. Maddox, G. Nichol, M. Pham, I. L. Piña and J. G. Trogdon, *Circulation, Heart Failure*, 2013, **6**, 606-619.
8. K. A. A. Clark, S. W. Reinhardt, F. Chouairi, P. E. Miller, B. Kay, M. Fuery, A. Guha, T. Ahmad and N. R. Desai, *Journal of Cardiac Failure*, 2022, **28**, 171-180.
9. A. S. Bhatt, K. S. Jering, M. Vaduganathan, B. L. Claggett, J. W. Cunningham, N. Rosenthal, J. Signorovitch, J. J. Thune, O. Vardeny and S. D. Solomon, *JACC Heart Failure*, 2021, **9**, 65-73.
10. M. King, J. Kingery and B. Casey, *American Family Physician*, 2012, **85**, 1161-1168.
11. K. Cox, V. Devanarayan, A. Kriauciunas, J. Manetta, C. Montrose and S. Sittampalam, *Eli Lilly and Company and the National Center for Advancing Translational Sciences*, 2014.
12. F. S. Felix and L. Angnes, *Biosensors & Bioelectronics*, 2018, **102**, 470-478.
13. B. V. Chikkaveeraiah, A. A. Bhirde, N. Y. Morgan, H. S. Eden and X. Chen, *ACS Nano*, 2012, **6**, 6546-6561.
14. A. Warsinke, A. Benkert and F. W. Scheller, *Fresenius' Journal of Analytical Chemistry*, 2000, **366**, 622-634.
15. K. S. Prasad, X. Cao, N. Gao, Q. Jin, S. T. Sanjay, G. Henao-Pabon and X. Li, *Sensors and Actuators B: Chemical*, 2020, **305**.
16. K. M. Clark, M. S. Schenkel, T. W. Pittman, I. C. Samper, L. B. R. Anderson, W. Khamcharoen, S. Elmegerhi, R. Perera, W. Siangproh, A. J. Kennan, B. J. Geiss, D. S. Dandy and C. S. Henry, *ACS Measurement Science Au*, 2022, **2**, 584-594.

17. B. Zaborska, M. Sikora-Frąc, K. Smarż, E. Pilichowska-Paszkiet, A. Budaj, D. Sitkiewicz and G. Sygitowicz, *International Journal of Molecular Sciences*, 2023, **24**.
18. X. Zhang, Y. Wan, R. Chata, A. Brazzale, J. J. Atherton, K. Kostner, G. Dimeski and C. Punyadeera, *Journal of Clinical Pathology*, 2016, **69**, 1100-1104.
19. X. Zhang, T. Walsh, J. J. Atherton, K. Kostner, B. Schulz and C. Punyadeera, *Theranostics*, 2017, **7**, 4350-4358.
20. X. Zhang, D. Broszczak, K. Kostner, K. B. Guppy-Coles, J. J. Atherton and C. Punyadeera, *Biomolecules*, 2019, **9**.
21. Z. Khurshid, S. Zohaib, S. Najeeb, M. S. Zafar, P. D. Slowey and K. Almas, *International Journal of Molecular Sciences*, 2016, **17**.
22. C. X. Sun, N. Bennett, P. Tran, K. D. Tang, Y. Lim, I. Frazer, L. Samaranayake and C. Punyadeera, *Diagnostics (Basel, Switzerland)*, 2017, **7**.
23. L. Azzi, V. Maurino, A. Baj, M. Dani, A. d'Aiuto, M. Fasano, M. Lualdi, F. Sessa and T. Alberio, *Journal of Dental Research*, 2021, **100**, 115-123.
24. J. A. Loo, W. Yan, P. Ramachandran and D. T. Wong, *Journal of Dental Research*, 2010, **89**, 1016-1023.
25. J. Noiphung, M. P. Nguyen, C. Punyadeera, Y. Wan, W. Laiwattanapaisal and C. S. Henry, *Theranostics*, 2018, **8**, 3797-3807.
26. K. D. Tang, K. Baeten, L. Kenny, I. H. Frazer, G. Scheper and C. Punyadeera, *Cancers*, 2019, **11**.
27. R. Mohamed, J.-L. Campbell, J. Cooper-White, G. Dimeski and C. Punyadeera, *Clinical and Translational Medicine*, 2012, **1**.
28. X. Zhang, N. Karunathilaka, S. Senanayake, V. N. Subramaniam, W. Chan, K. Kostner, J. Fraser, J. J. Atherton and C. Punyadeera, *Clinical Research in Cardiology*, 2020, **109**, 685-692.
29. S. Govindaraj, M. J. Daniel, S. S. Vasudevan and J. V. Kumaran, *Dentistry and Medical Research*, 2019, **7**, 56-59.
30. X. H. Yang and W. L. Zhu, *Cellulose*, 2007, **14**, 409-417.

Chapter 4 - Low-Cost Capillary Flow Microfluidic Devices for Rapid Analysis of Blood Phenotypes Associated with Sickle Cell Disease and Hemostasis

4.1 Overview

The goal of this chapter is to describe the development of two separate capillary-flow driven microfluidic devices that utilize whole blood samples: one for phenotyping Sickle Cell Disease (SCD) and the other for monitoring hemostasis (clotting). The work presented in this chapter was completed in collaboration with Drs. Eudorah Vital and Wilbur Lam at Georgia Tech and Emory University, Dr. David Bark at Washington University in St. Louis, and Trey Pittman in the Henry Group at Colorado State University.

4.2 Introduction

Whole blood is a challenging sample matrix to work with when designing a fluidic assay because it is a non-Newtonian, two-phase liquid; the plasma is an aqueous solution containing various molecules including salts and proteins, while the cellular phase contains red blood cells (RBCs), white blood cells (WBCs), and platelets.[1] Rheological properties of whole blood can vary based on the physical properties of each phase, with the RBCs' properties having a significant influence compared to the rest of the components.[2] Extrinsic factors, such as shear rate and temperature, as well as intrinsic factors, such as hematocrit and RBC deformability, affect the viscosity of whole blood.[1, 3] This chapter focuses on development of microfluidic devices capable of probing different rheological properties of whole blood related to SCD and clotting using capillary flows instead of traditional pressure driven flow. The goal for this portion of my thesis

project was to reduce the complexity of the microfluidic devices required for making these complex measurements.

RBCs of SCD patients lose their deformability, resulting in RBCs of varying rigidity, and therefore varying the severity of SCD complications.[1] SCD is commonly screened for at birth in developed countries,[4] and many diagnostic tests exist[5-7]. Electrophoresis is considered a gold standard method for detecting hemoglobin variants,[6] but it is very expensive and requires trained personnel. Some paper-based SCD diagnostics such as the HemeChip are low-cost and somewhat portable, but require lysis of the sample and other handling steps.[8] Symptom and pain variability between SCD patients and also within the same patient but different episodes is very common and makes it difficult for a single treatment approach to work for all patients.[4, 9] Screening and diagnosis of SCD has been well established, but there is still a need for effective means of monitoring the disease as classification of sickle patients and their episodes is not straightforward.[7, 10] As more SCD therapies become clinically available there is a clear need for a low-cost, point-of-care (POC) diagnostic device that can rapidly and accurately identify a patient's SCD phenotype so that an informed treatment approach can be taken.[5, 11, 12]

To mimic SCD, three reagents are typically used, calcium chloride ($CaCl_2$), sodium metabisulfite ($Na_2S_2O_5$), and adenosine diphosphate (ADP). Adding $CaCl_2$ adds free Ca^{2+} ions into citrated blood and causes the coagulation process to initiate and be investigated under controlled conditions.[13] $Na_2S_2O_5$ reduces the oxygen tension in the blood, inducing polymerization of the hemoglobin S (HbS) that causes the sickle cell shape of the RBCs to form.[7] ADP can activate platelets and cause thrombus formation.[14] At present, assays involving these three reagents are typically done in a microtiter plate and are slow and expensive.[15] Our team sought to develop an integrated device to simplify the assay where whole blood samples are individually mixed with

the reagents in the device, and then their impact on rheological properties by their flow in a nitrocellulose membrane (NCM). The reaction between the blood and the reagent affects the RBCs' ability to migrate within the NCM .[16] By comparing the migration of the blood with each different reagent, clinicians are able to gain an understanding of the underlying cause of a SCD patient's pain (e.g., low O_2, platelets, etc.) and administer appropriate treatment. A sample of whole blood would be added to the device where it reacts with reagent pads containing one of the reagents listed above dried in the pad, and the migration pattern of the blood components within a NCM downstream of the reagent pad would illustrate the phenotype of the sample's SCD state.

Blood clotting is another element of blood that affects rheology. Hemostasis is the process by which blood forms a clot or a thrombus to stop flow, and it involves a cascade of reactions between blood platelets, proteins and various coagulation factors.[13] In the event of an injury, coagulation rapidly limits blood loss from a damaged vessel. Inhibition of coagulation using anticoagulants such as heparin or warfarin,[17] is required to reduce the risk for stroke, pulmonary embolism, heart attack, and other life-threatening cardiovascular diseases. Constant monitoring of long-term anticoagulation efficacy is critical for these patients.[13, 17] If the anticoagulant drug level is too low, the risk of blood clot formation is high. Conversely, if the drug level is too high, severe bleeding (hemorrhage) can occur. Monitoring anticoagulation therapy is usually performed by trained specialists in a hospital or laboratory setting, resulting in expensive, slow testing.[13]

Von Willebrand factor (VWF) and platelets are essential for primary hemostasis.[18] Clinical evaluation of platelet agglutination to assess primary hemostasis function is done through light transmission aggregometry.[19-21] This requires specialized equipment, large sample volumes of blood, and trained personnel to perform, making it inaccessible to those in resource-limited and rural communities. Another technique, the Multiplate® platelet impedance technique uses whole

blood to assess platelet function via platelet aggregation[21] and the effects of anti-platelet drugs.[22-24] The Platelet Function Analyzer (PFA-100®) is considered a gold standard for measuring platelet adhesion and aggregation under high shear conditions, is less laborious and is a useful tool for VWD diagnosis and treatment monitoring.[25] All of these methods require trained personnel in a centralized facility, leaving a still unmet need for a POC test that can assess hemostasis.

The second device described in this chapter is called the Paper-based Clotting Analysis Test, or PCAT. We worked with Dr. David Bark at Washington University in St. Louis to create a low-cost, capillary flow device that could subject whole blood to relatively high flow rates (~50 μL/min) for sustained durations (~5-10 min) to force the blood to undergo primary hemostasis and form a thrombus at the site of a stenosis within the device. The device is meant to use a geometric change via a stenosis to cause VWF extension, lead to shear-induced platelet activation and aggregation and would aid in reducing the time to result for clotting analysis.[26]

4.3 Materials and Methods

4.3.1 Microfluidic Device Design

The SCD capillary flow device (Figure 1) was designed using Onshape (Onshape, USA) and cut using a CO_2 laser cutter (Zing 10000, Epilog Laser) to pattern polyethylene terephthalate (PET) film (9984) and 3M 468 double-sided adhesives (DSA). The top PET layer has vent holes to improve uniformity of flow in the device as discussed in the results and discussion. A Whatman Grade 4 Qualitative (W4Q) filter paper (MilliporeSigma, USA) reagent pad was hand cut to 3 mm x 5 mm, and HF75 (MilliporeSigma, USA) nitrocellulose membrane (NCM) was hand cut to 5 mm x 40 mm. A single input of blood flows into the channel and through the paper reagent pad, where it reacts with a compound dried within the pad.

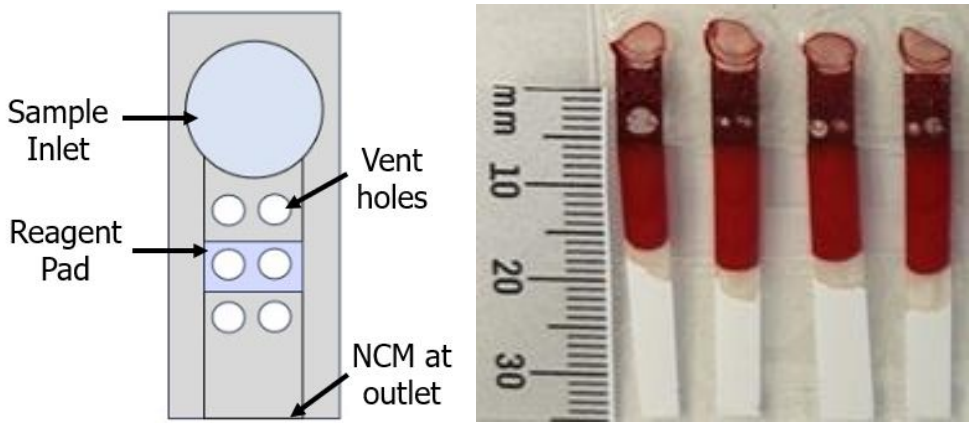

Figure 4.1. Single-channel SCD microfluidic device. Left is a schematic of the single-channel SCD phenotyping device showing the sample inlet, vent holes, reagent pad, and outlet where the NCM is inserted. **Right** is an image of several devices where plasma and blood components can be seen separated in the NCM.

The PCAT capillary flow device was designed using Onshape and cut using a CO_2 laser cutter to pattern polyethylene terephthalate (PET) films (9984) and 3M 467 and 468 double-sided adhesives (DSA). PET film and DSA were used to generate specific channel heights among different device designs. The stenosis(es) within the device was formed as shown in Figure 2. A stenosis was generated by either manipulating channel width (horizontal, shown in Figure 2 as **H**)

or height (vertical, shown in Figure 2 as **V**), or by using the pores of either Whatman Grade 1 (11 µm pore size) or Whatman Grade 4 (20-25 µm pore size) paper (Figure 2, denoted as **P**). More details on these devices and their properties are provided in the results and discussion.

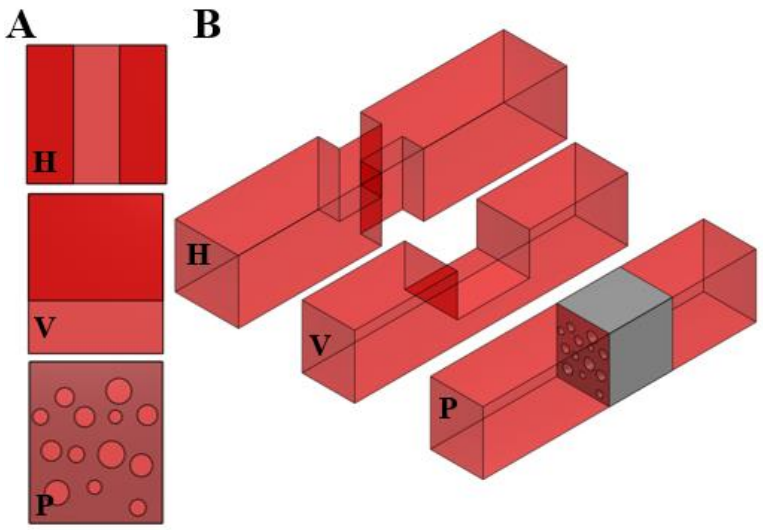

Figure 4.2. PCAT Device Stenosis Schematic. (A) shows the front view of a channel with a horizontal (**H**), vertical (**V**) or pore-based (**P**) stenosis, where the lighter colored region shows the narrower region of the channel where flow passes through the stenosis. (B) shows the three stenosis designs from a 3D, isometric view. The paper pad shown for the pore-based stenosis has been simplified to just show the pores from the front size, but pores do exist throughout the paper material.

4.3.2 Reagent Preparation and Experimental Flow

Phosphate-buffered saline (PBS) was prepared by dissolving a tablet (Research Products International, USA) in Milli-Q system water (MilliporeSigma, USA). 10 mM (1x) PBS was composed of 140 mM sodium chloride and 2.7 mM potassium chloride at pH 7.4. 100 mM (10x) PBS was composed of 1.4 M sodium chloride and 27 mM potassium chloride at pH 7.4. 5X PBS was made by diluting 10X PBS in Milli-Q system water. Healthy human blood was provided by our collaborator Dr. Eudorah Vital and stored at 4°C under IRB approval from Emory University; before using it for an experiment it was removed from the refrigerator and allowed to reach room temperature, then the tube was gently inverted several times to ensure the components were

distributed throughout. HF75 Nitrocellulose was provided by Dr. Eudorah Vital and was stored at 4°C with desiccant; before using it for an experiment it was taken out of the refrigerator and allowed to reach room temperature before being removed from the sealed pouch. A 5 M $CaCl_2$ stock solution was prepared by dissolving 0.735 g of calcium chloride dihydrate (Millipore Sigma, USA) in 1X PBS, and all other concentrations were diluted from this stock solution in 1X PBS. 2% $Na_2S_2O_5$ solution was made by dissolving 0.02 g of $Na_2S_2O_5$ (provided by Dr. Vital) in 1 mL of 0.01 M $CaCl_2$ in 1X PBS.

Eriochrome Black T (EBT) indicator solution was made by dissolving 0.20 g of EBT (Sigma-Aldrich, USA) in 15 mL of Milli-Q system water. A 0.05 M Ethylenediaminetetraacetic acid (EDTA) solution was prepared by dissolving 0.095 g of EDTA in Milli-Q system water. 1 µL of the EBT solution was diluted in 100 µL of the 0.05 M EDTA to product a blue-colored solution. Malachite green indicator solution was made by diluting 50 µL of stock malachite green solution (Sigma-Aldrich, USA) in 950 µL of Milli-Q system water.

For blood experiments, a 3D printed triangular prism guide (dimensions = 56.4 mm x 60 mm x 50 mm x 20.5 mm tall) was placed on the benchtop, with double-sided tape on the top face. A sheet of white printer paper (to give a clean background for photos and videos) was placed on top of the guide, with double-sided tape on top of the sheet. A clean sheet of PET film was placed onto the white paper, with two ~10 mm wide strips of DSA spaced approximately 20 mm apart on the top of the transparency. Assembled devices were secured onto the PET film with the bottom of the device (where the NCM is inserted) at the bottom of the first DSA strip, and the bottom half of the NCM strip secured onto the second DSA strip.

For photo analysis, ImageJ software (NIH) was used. To calculate Mean Grey Ratio for colorimetric tests, images were inverted, converted to 8-bit greyscale, and the ellipse tool was used

to create a small area toward the center of the reagent spot. The mean gray value was taken for the spotted area as well as a region outside of the spot of the same size area. The ratio of the two values (reagent spot/background) is the "mean gray ratio," and helps account for slight differences in lighting/background between images. To calculate distance, the scale was set using a ruler that was included in the frame when the image was taken. A straight line was drawn from the edge of the NCM to the end of either the blood or plasma in the NCM, and the measurement tool was used to find the length of the line drawn. To calculate area, the scale was set as above, and the polygon tool was used to draw a shape around the perimeter of the blood or plasma on the NCM. The polygon tool was then used to draw a shape around the perimeter of the NCM. The area percentage was calculated by dividing the area of either blood or plasma by the area of the NCM, multiplied by 100%.

4.4 Results and Discussion

4.4.1 Colorimetric Validation of SCD Assay Reagents

Before we could start constructing devices containing clotting reagents for testing blood behavior associated with SCD, we first had to verify the reagents remained viable after being dried in our paper reagent pads. We identified colorimetric indicators that would react with two of the reagents: Eriochrome Black T (EBT) to react with $CaCl_2$ to cause a blue-to-pink color change, and Malachite green[27] to react with $Na_2S_2O_5$ to cause a teal-to-colorless change. Figure 3(A) shows the first colorimetric test performed with liquid reagents, with the presence of $CaCl_2$ causing the solution to turn from blue to pink in color. This test was repeated in paper reagent pads and the color change was qualitatively confirmed by naked eye. Figure 3(B) shows the results of the colorimetric test done to ensure the sodium metabisulfite remained viable after drying overnight in a 37°C oven. The formation of a colorless product upon reaction with the Malachite green reagent demonstrates the effectiveness of the dried $Na_2S_2O_5$.

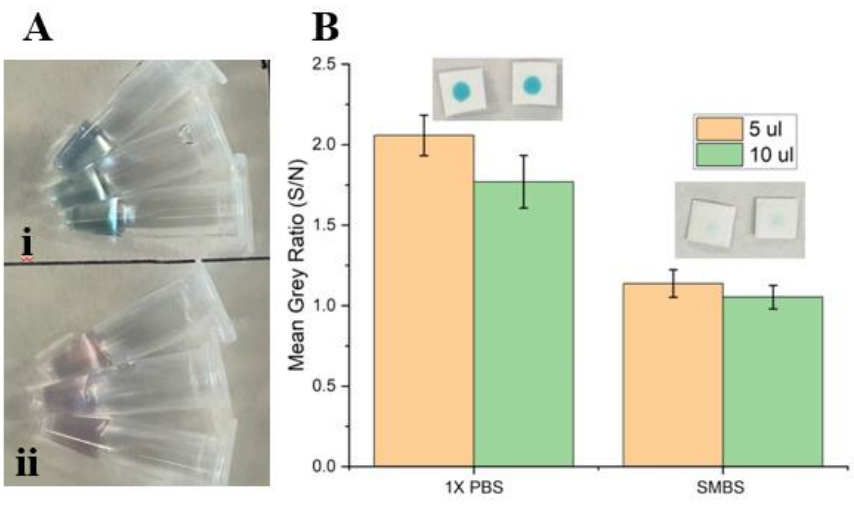

Figure 4.3. SCD Colorimetric Validation. (A) Colorimetric test for $CaCl_2$ reagent using EBT solution. (i) shows EBT + Milli-Q system water, (ii) shows EBT + 1.0 M $CaCl_2$ in Milli-Q system water. (B) 1X PBS or 2% $Na_2S_2O_5$ in 1X PBS dried onto W4Q pads were rehydrated with 0.05% Malachite Green. ImageJ was used to identify a mean grey ratio of the spot color relative to the background paper color. Representative images of each group are above the data. SMBS = Sodium Metabisulfite.

4.4.2 SCD Device Top Layer Vent Optimization

One of the first challenges we faced when creating the SCD device was nonuniformity of flow within the channels. For example, some samples blood would preferentially flow along one side of the channel (Figure 4(A)) until they reached the NCM, causing them to enter the NCM at an angle, while others began to flow unevenly after reaching the NCM (Figure 4(B)). These devices flowed much slower than devices where blood was evenly distributed in the channel and the front entered the NCM all at once. We found that running experiments with the device at an angle where the inlet was higher than the NCM improved the uniformity of flow for all devices, so I designed and 3D printed a triangular prism with the top face at a 20° angle from the table surface that all devices were secured to for future experiments. However, this solution was only partially successful in preventing nonuniform flow.

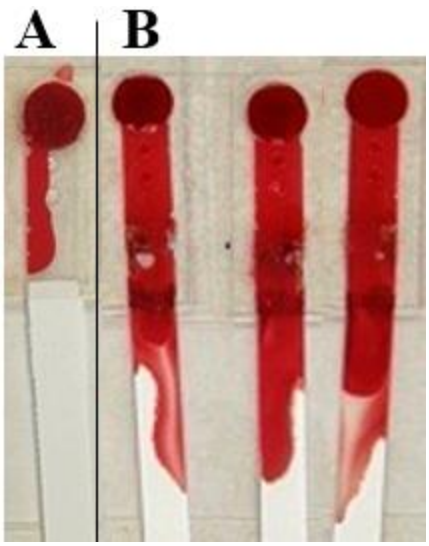

Figure 4.4. Imperfect flow in SCD devices. (A) shows a device where blood flowed unevenly within the channel, and (B) shows three devices where blood and plasma flowed unevenly within the NCM.

We hypothesized that the viscous blood could be trapping air bubbles that directed flow to one side of the membrane. To test this hypothesis, we added vent holes to enable air bubbles to escape through the top of the device instead of blocking flow. We conducted flow studies to test

this hypothesis and identify optimal vent hole placement for the top layer of the device using healthy blood with 1X PBS dried in the reagent pads, as that was the control condition for all SCD blood device tests. Figure 5 shows the different variations of top layer vents that we compared. For the vents shown in Figure 5(A)-(C), numerous flow issues were observed. In some cases, blood flowed outside the device from the reagent pad vent in 5(B), or the top of the inserted NCM partially or completely blocked the vents in 5(B) and (C) causing flow to unevenly enter the NCM by flowing around the vent. The most consistent results were observed for the vents in Figure 5(D) and (E). These designs were tested further to compare the flow of healthy blood with 0 M or 0.25 M $CaCl_2$ in 1X PBS dried in the reagent pad.

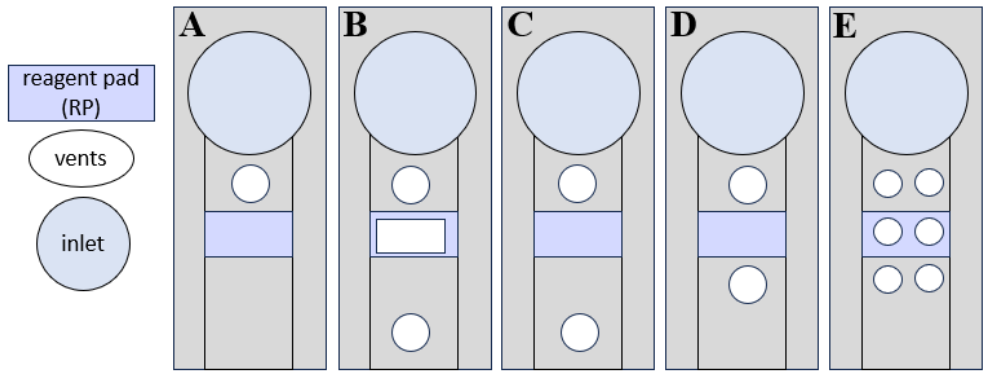

Figure 4.5. SCD Top Layer Vent Designs. (A) shows a design with one vent before the reagent pad (RP). (B) shows one vent before the RP, one large vent over the RP, and one near the NCM. (C) has one vent before the RP and one near the NCM, but no vent over the RP. (D) has two vent holes surrounding the RP. (E) has six vent holes, two before the RP, two over the RP, and two after the RP.

Figure 6 shows the percentage of NCM covered by blood and plasma for each vent configuration in Figure 5(D) and (E), referred to as "two" or "Lego®", respectively. While observing the flow during the experiment, flow in devices with the Lego® vent visually seemed to have more uniform flow in more devices. Similar capillary flow devices have shown that air bubbles can make flow nonuniform or stop it altogether,[28] so the six-vent design likely is the most effective at removing trapped air in our device. That, along with slightly smaller error bars compared to the two-vent design led us to move forward with the Lego® top layer for future device optimization.

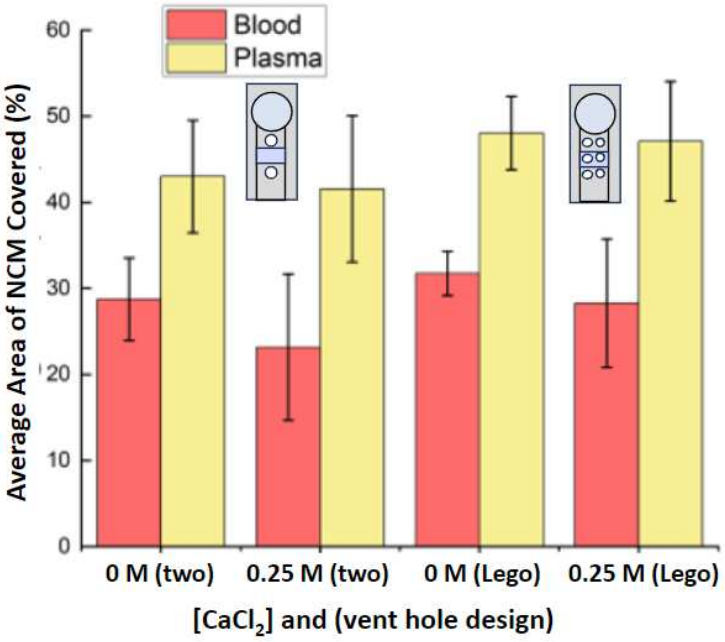

Figure 4.6. SCD Top Layer Vent Comparison. Two top layer vent designs were compared using 0M PBS (control) or 0.25M $CaCl_2$ in 1X PBS dried in the reagent pads. (two) = two vent holes, one above and one below the reagent pad,

4.4.3 Primary Validation of SCD Device with Healthy Blood

Once we confirmed that the reagents remained viable in the paper pads after being dried completely, we received healthy blood from Dr. Vital for testing in the devices. While the reagents are meant to exacerbate problems with sickle blood, we still expected to see a difference in the migration ability of healthy blood between control and treatment conditions. Figure 7(A) shows a comparison between 1X PBS and 0.25 M $CaCl_2$, where the plasma and blood in devices with $CaCl_2$ flowed a shorter distance. For the next experiment using $Na_2S_2O_5$ we measured the percent area of the NCM that was covered by blood and plasma to see if this was a more consistent way to analyze the data (previous distance measurements were inconsistent between team members if the flow wasn't completely uniform). Figure 7(B) shows a comparison between 1X PBS and 2% $Na_2S_2O_5$, where the plasma and blood in devices with $Na_2S_2O_5$ flowed a shorter distance and covered less area in the NCM for both doses (5 µL and 10 µL) of $Na_2S_2O_5$.

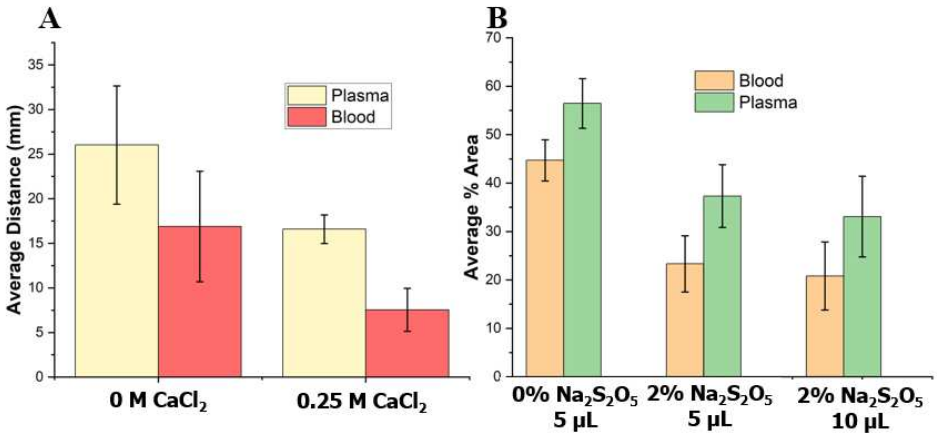

Figure 4.7. Validation of SCD devices with Healthy Blood. (A) Devices containing reagent pads with either 0 M CaCl2 or 0.25 M CaCl2 in 1X PBS were compared using healthy blood, and the average distance traveled of plasma and blood is shown. (B) Devices containing reagent pads with either 5- or 10 µL of 2% $Na_2S_2O_5$ in 1X PBS were compared using healthy blood, and the percent area covered in the NCM for plasma and blood is shown.

4.4.4 Preliminary Validation of SCD Device with Sickle Blood

Once we confirmed that the reagents remained viable in the paper pads after being dried completely and that the devices performed consistently with healthy blood, we mailed devices to our collaborators for testing with both healthy and sickle blood. Figure 8 shows the results of the sodium metabisulfite devices comparing the total distance traveled of both healthy and sickle blood. The results consistently showed a dose-dependent correlation with sodium metabisulfite (Figure 8). The migration paths of both sickle and healthy blood cells were reduced with higher volumes of sodium metabisulfite present in the reagent pad. While the error bars appear to overlap, there is a promising trend that the sickle blood travels a shorter distance than the healthy blood. The sickle blood also traveled more slowly than healthy blood in these devices. This is expected, because the low oxygen environment with the metabisulfite reagent will cause the sickle blood cells to become more rigid in their sickle shape and aggregate together, making it more difficult for the sickle blood to migrate through the NCM.

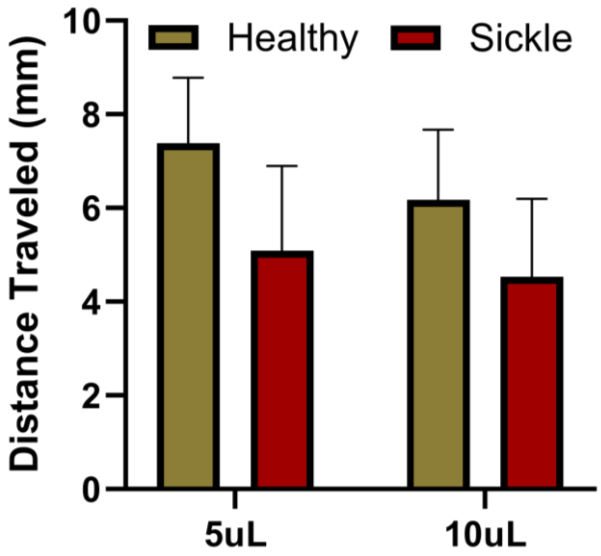

Figure 4.8. Preliminary Validation of Sodium Metabisulfite Reagent with Sickle and Healthy Blood. Devices containing reagent pads with either 5- or 10 µL of 2% $Na_2S_2O_5$ in 1X PBS were compared with both healthy and sickle cell blood, and the average total distance traveled in the NCM is shown.

4.4.5 First Steps Toward Multiplexing the SCD Device

While single channel devices were undergoing evaluation, we began initial steps toward multiplexing the SCD device. This included adapting a single channel device into a two-channel device, with the channel mirrored across the inlet circle (Figure 9A). We used healthy blood and 1X PBS dried in reagent pads and measured the resulting percent area covered by plasma and blood. We expected all NCM to have equal coverage of plasma and blood because all reagent pads were prepared identically, and we expected the blood to flow equally into both channels. The results are shown in Figure 9(B), where one side of the device was denoted as "side 1" and the other as "side 2" for comparing, and the data on the far right shows the values for all NCM strips. The results are very similar across all devices and NCM strips, indicating this two-channel device is a step in a positive direction towards the eventual 4-channel multiplexed device. The same design of two channels mirrored across from one another will be used to design the four-channel device, with it appearing like a four-way intersection on a road. Symmetry in the two-channel device worked to equally distribute blood to both channels, so we will make the four-channel device symmetrical too. The same small inlet hole will also be used for the four-channel device design, as it serves as a guide for the pipet tip that prevents bias toward any one channel when adding the blood sample. Similar studies to the one conducted to generate the data shown in Figure

9 will be conducted using the four-channel device to validate equal distribution of the sample before we begin to incorporate the different chemical reagents in the reagent pads.

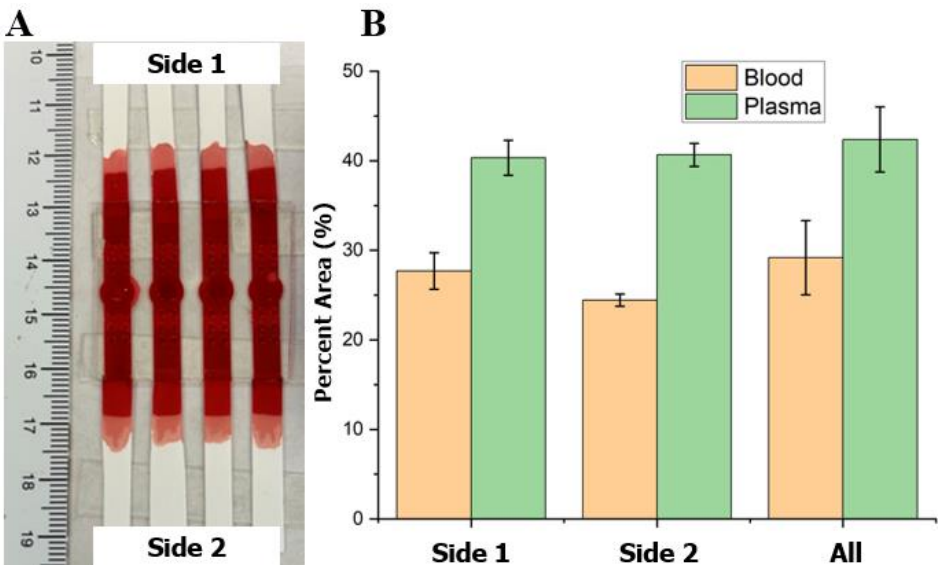

Figure 4.9. Two-Channel SCD Device. (A) shows healthy blood used to test the first multi-channel SCD device. (B) shows the percent area coverage of plasma and blood for both sides of the device, as well as all the data for all strips combined.

4.4.6 PCAT Device Design Evolution

The design of the PCAT device evolved tremendously throughout the course of my time on the project. Key device criteria to induce primary hemostasis included fast flow rates (~50 μL/min), sustained flow for >5 min, and a stenosis or narrowing of the channel to serve as the site where a thrombus would most likely form. The figures below show the progression of the design based on things we learned from previous iterations as well as things we learned from more meetings with our collaborators. The designs versions shown in Figure 10 show the first attempts at getting blood to flow through long capillary channels with the target velocities. Figure 10(A) included a horizontal stenosis (as shown in Figure 2, denoted as **H**) and a paper pump, but we quickly realized that the paper clogs rapidly and stops flow altogether. Figure 10(B) shows two designs with a horizontal stenosis, but instead of a paper pump to continuously pull blood from the inlet we included a reservoir at the end of the channel. The designs in Figure 10(B) flowed very rapidly (50 μL flowed in < 30 s) but the channel dimensions prevented us from being able to load a large volume of blood and sustain flow; 10(C) used the same channel width as the narrow

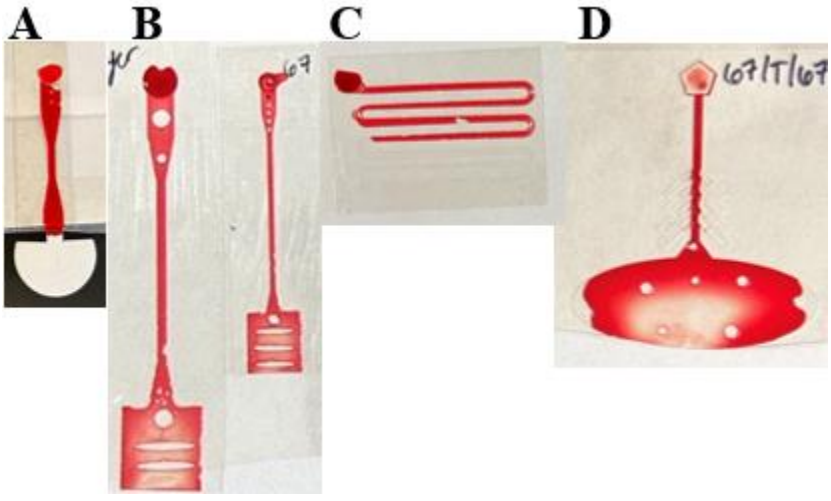

Figure 4.10. First Design Concepts of the PCAT Device. (A) shows a horizontal stenosis with a paper waste pad at the outlet. (B) shows a horizontal stenosis with a reservoir at the end of the channel. (C) shows a long, winding channel with blood stopped partway through the device. (D) shows a vertical, branched channel with a round reservoir at the end of the channel.

region in 10(B) but attempted to create a long, winding channel to increase flow time. This design was unsuccessful because the capillary pressure eventually became too high for the blood to flow through the full device. Figure 10(D) shows a device that included some features from 10(B) but included branches and a rounded reservoir. The reservoir in 10(D) was large enough that the top layer collapsed inward toward the bottom, so we added small pieces of DSA to prop up the reservoir in some spots (seen as clear dots throughout the blood in the reservoir).

While the devices shown in Figure 10 reached the necessary flow rate, they did not sustain flow for long enough. Figure 11 shows various designs we explored that had a larger reservoir, once again to sustain more blood flowing for longer times. Figure 11(A) shows a shorter channel after the inlet with a very large reservoir relative to the channel size. Figure 11(B) shows a longer channel before a medium sized reservoir, with the channel branching out and converging several times before it meets the reservoir. The designs in Figure 11(A) and (B) were created with a single layer of DSA, so essentially the full device was a narrowed region but there were no changes to the channel height. Figure 11(C) was a smaller version that was created and tested at the same time as that in 11(B). The flow was very fast, but the device could not hold sufficient volume to sustain flow for more than 30 s. Figure 11(D) combined the ideas from 11(A) and 11(B) but moved the branch to the area where the channel and reservoir meet. The very large reservoir in 11(D) greatly increased the volume of blood we could flow through the device compared to 11(B) and 11(C), but the large geometric size caused the top layer to collapse over the reservoir again similar to Figure 10(D).

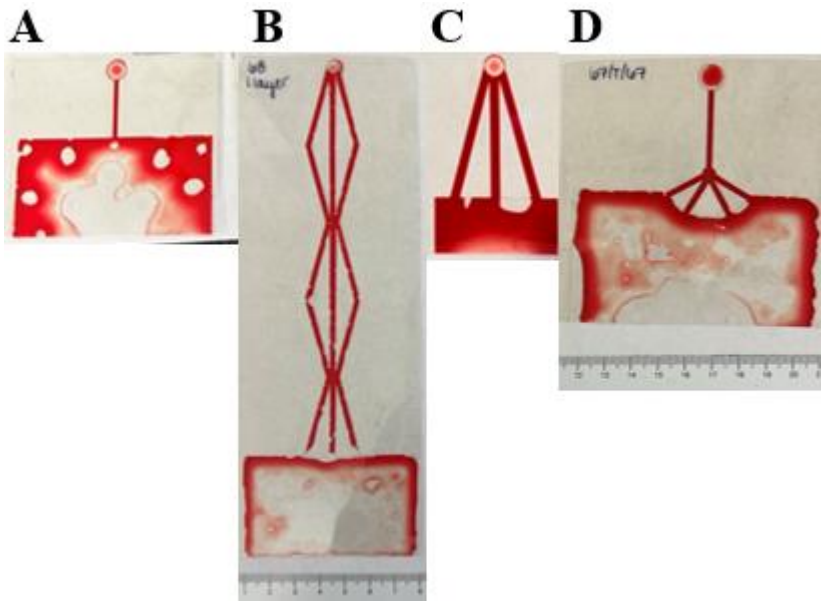

Figure 4.11. Reservoir-Focused Design Concepts of the PCAT Device. (A) shows short channel with a relatively large reservoir. (B) shows a long channel that branches and converges with a medium-sized reservoir at the end of the channel. (C) shows short device with three channels branching directly from the inlet and meeting at a reservoir. (D) shows a long channel that branches right at the point it meets the large reservoir at the end of the channel.

Figure 12 shows PCAT design concepts with reservoirs that are significantly larger than the channels, and with more sophisticated vent designs over the reservoirs. We learned that the vents from the designs in Figure 10(B) and 10(D) the open areas prevent blood from flowing there, so we used that to our advantage to create 'pseudo-channels' within the reservoir areas. We observed similar flow to the branching in Figure 11(B) with these 'pseudo-channels,' often causing the flow to be sustained for much longer in devices where the reservoir had the vents compared to those that did not. Figure 12 also shows the first devices incorporating a vertical stenosis, where the layers of the device were aligned to cause a decrease in channel height from 225 μm to 75 μm over a very short distance (<1 mm) before opening back up to 225 μm. In each design there is a stenosis at the end of the branch at the point each branch meets the reservoir. Figures 12(A) and 12(B) are nearly identical designs, with the difference being the angle at which the channels branch off from the inlet channel to meet the reservoir. Figure 12(C) simplified the three branches from

12(A) and 12(B) into two, with the curved edges at the entrance to the reservoir to increase the length of the initial edge that the blood contacted. Figures 12(D) and 12(E) are the same in concept but differ in size and frequency of the reservoir and its respective vents. Figures 12(D) and 12(E) build off of the two-branch idea from 12(C) but change it to a 45° angle at the split rather than 90°. The device in Figure 12(D) is larger than that in 12(E), where we tried to load a higher volume of blood to see if flow would continue for a longer duration.

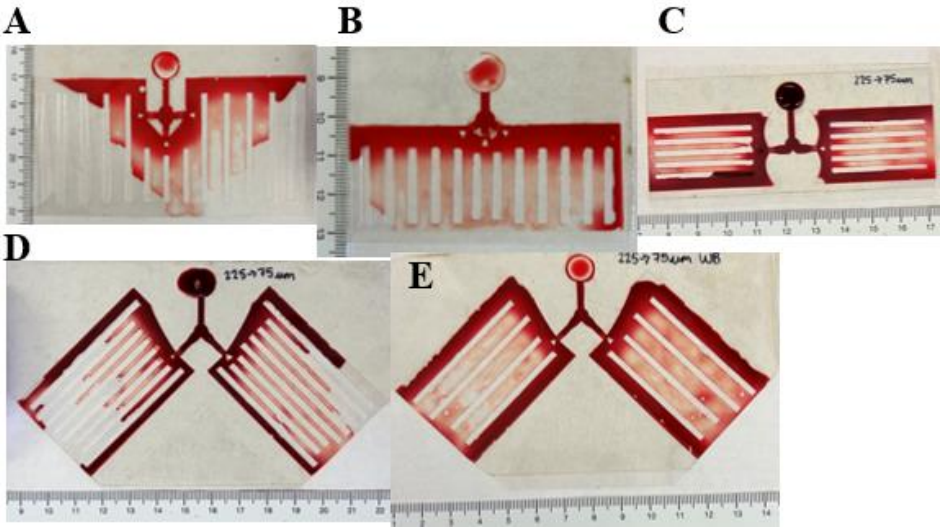

Figure 4.12. Vented Reservoir Design Concepts of the PCAT Device. (A) shows a short channel with two branches that connect to the main channel at 90° angles, with a stenosis just before each branch meets the reservoir. (B) shows a short channel with two branches that connect to the main channel at 45° angles, with a stenosis just before each branch meets the reservoir. (C) shows a short channel that splits into two branches at 90° angles, with a stenosis just before each branch meets the reservoir. (D) and (E) show a short channel that splits into two branches at 45° angles, with a stenosis just before each branch meets the reservoir.

Figure 13 shows the final few iterations of the PCAT design, with the most recent design shown in Figure 13(C). Figure 13(A) revisited some of the success we found in the branching design and combined it with the vents over the reservoir, with the vertical stenosis right after the inlet and before the branch points. This design flowed very quickly, but again just couldn't hold enough volume to sustain flow for longer than ~60 s. Figure 13(B) tried to utilize the branching-converging concept in a more streamlined way with fewer separation between the branching

points. For the design in Figure 13(B) each branch had a stenosis again, located halfway down the chain link shape of the first two branches. Again, this design flowed very quickly but could not hold much sample volume. The rounded curves to the channels in Figure 13(B) showed more uniform flow than previous design iterations, where sometimes the sharp points in branches would stop flow altogether for unknown reasons. The design in Figure 13(C) maintained the rounded channels and the branching-converging concept, but also considered the footprint of the device itself and aimed to minimize the materials wasted when the device was laser cut out of a larger sheet. The chain link design from Figure 13(B) was coiled into a spiral-like design to make the overall device more compact, but we kept a large, vented reservoir to allow for large sample volumes. The device in Figure 13(C) can sustain flow of 350 μL of blood for 6-8 min with the vertical stenosis dimensions of 225 μm to 75 μm. The same design as shown in Figure 13(C) was created but instead of a vertical stenosis created by the layers of PET and DSA, we incorporated Whatman paper pads where the pores of the paper created stenoses within the channel. The total channel height before and after the paper was 250 μm, and this configuration also sustained flow of 350 μL of blood for over 6 min. These values meet the key criteria we were aiming for when designing the device, so until we receive clotting data from our collaborator no further design changes will be made to the PCAT device.

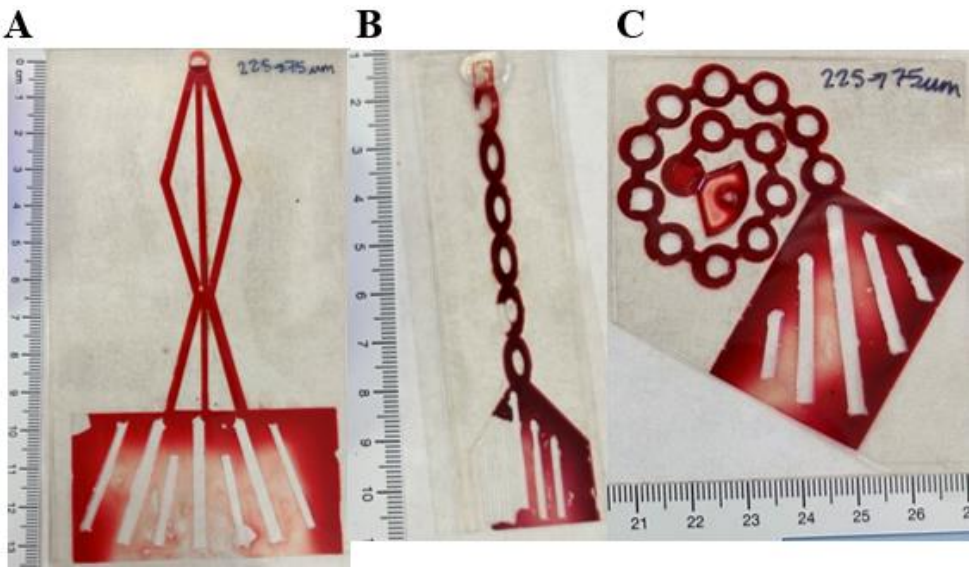

Figure 4.13. Final Design Concepts of the PCAT Device. (A) shows branching and converging channels with a large, vented reservoir, with the stenosis at the inlet of the device just before the branch points. (B) shows a branching and converging channel in a chain link-like design before the reservoir. (C) shows a spiral-shaped device with rounded branching and converging channels leading to a large, vented reservoir.

4.5 Conclusions and Future Outlook

Both devices described in this chapter can successfully process whole blood samples without the need for complicated pre-processing or external pump systems. Initial validation of both devices has been completed with promising results. For the SCD project, we first confirmed that the reagents remain viable after being dried in reagent pads. We then demonstrated that there is a difference in migration behavior of healthy blood and plasma in control (1X PBS) vs. treatment ($CaCl_2$, $Na_2S_2O_5$) conditions. Preliminary data from collaborators suggests there is a difference in migration behavior of healthy vs. sickle cell blood and plasma in control (1X PBS) and treatment ($CaCl_2$, $Na_2S_2O_5$) conditions. We have also shown preliminary work towards a multichannel device with promising results. Next steps for this project include finishing the data analysis on the $CaCl_2$ and ADP devices that were sent to our collaborators to identify if any further changes need to be made to the design. If the results are satisfactory, we can work toward refining the multiplexed

system into four different channels, each with a uniquely treated reagent pad with the optimal concentration of reagent dried onto it (1X PBS control, $CaCl_2$, $Na_2S_2O_5$, and ADP). This multiplexed system would provide a more wholistic view of a patient's SCD phenotype, so a clinician could make a well-informed decision about the most appropriate treatment approach for that individual.

For the PCAT project, we have shown extensive design evolution with various approaches to create a stenosis. Initial validation in our lab confirms we can generate fast flow for over 6 minutes, but until the device is tested with fresh blood containing viable platelets we cannot confirm if primary hemostasis is occurring and a clot is forming. We have recently sent devices with both the vertical stenosis and the Whatman paper stenosis to our collaborators. Once we understand how the pore stenoses compare we can move forward with the most consistent and reliable design and make any necessary changes to the device itself. Our collaborator will compare the PCAT devices using healthy blood with and without a platelet inhibitor, and we expect the uninhibited blood to form a larger thrombus faster than the inhibited blood.

References

1. E. Nader, S. Skinner, M. Romana, R. Fort, N. Lemonne, N. Guillot, A. Gauthier, S. Antoine-Jonville, C. Renoux, M.-D. Hardy-Dessources, E. Stauffer, P. Joly, Y. Bertrand and P. Connes, *Frontiers in Physiology*, 2019, **10**.
2. G. A. M. Pop, D. J. Duncker, M. Gardien, P. Vranckx, S. Versluis, D. Hasan and C. J. Slager, *Netherlands Heart Journal*, 2002, **10**, 512-516.
3. G. D. Sloop, G. Pop, J. J. Weidman and J. A. S. Cyr, *Cureus*, 2024, **16**.
4. D. C. Rees, V. A. M. Brousse and J. N. Brewin, *Blood Reviews*, 2022, **56**.
5. I. Kawooya, E. Kayongo, D. Munube, R. Mijumbi-Deve, S. Elliott, B. Vandermeer and N. Sewankambo, *The Cochrane Database of Systematic Reviews*, 2022, **2022**.
6. W. A. Arishi, H. A. Alhadrami and M. Zourob, *Micromachines (Basel)*, 2021, **12**.
7. Y. Alapan, A. Fraiwan, E. Kucukal, M. N. Hasan, R. Ung, M. Kim, I. Odame, J. A. Little and U. A. Gurkan, *Expert Review of Medical Devices*, 2016, **13**, 1073-1093.
8. M. N. Hasan, A. Fraiwan, R. An, Y. Alapan, R. Ung, A. Akkus, J. Z. Xu, A. J. Rezac, N. J. Komich, M. S. Creary, T. Oginni, G. M. Olanipekun, F. Hassan-Hanga, B. W. Jibir, S. Gambo, A. K. Verma, P. K. Bharti, S. Riolueang, T. Ngimhung, T. Suksangpleng, P. Thota, G. Werner, R. Shanmugam, A. Das, V. Viprakasit, C. M. Piccone, J. A. Little, S. K. Obaro and U. A. Gurkan, *Analyst*, 2020, **145**, 2525-2542.
9. M. Samir K. Ballas, P. Susan Lieff, M. Lennette J. Benjamin, M. Carlton D. Dampier, M. Matthew M. Heeney, M. Carolyn Hoppe, M. Cage S. Johnson, M. Zora R. Rogers, M. Kim Smith-Whitley, M. Winfred C. Wang and M. Marilyn J. Telen, *Am J Hematol*, 2010, **85**, 6-13.
10. A. Aich, Y. Lamarre, D. P. Sacomani, S. Kashima, D. T. Covas and L. G. d. l. Torre, *Frontiers in Molecular Biosciences*, 2021, **7**.
11. M. J. Telen, P. Malik and G. M. Vercellotti, *Nature Reviews, Drug Discovery*, 2019, **18**, 139-158.
12. M. Azul, E. F. Vital, W. A. Lam, D. K. Wood and J. D. Beckman, *Translational Research*, 2022, **246**.
13. H. Li, D. Han, G. M. Paulettib and A. J. Steckl, *Lab on a Chip*, 2014, **14**.
14. P. Tomasz Brzoska, M. Ravi Vats, B. Maritza Ann Jimenez, M. Egemen Tutuncuoglu, P. Margaret F. Bennewitz, M. Mark T Gladwin and P. Prithu Sundd, *Blood*, 2017, **130**.
15. C. S. Chimbatata, M. R. Chisale, A. B. Kayira, F. W. Sinyiza, B. C. Mbakaya, P. U. Kaseka, P. Kamudumuli and T.-S. J. Wu, *BMJ Paediatrics Open*, 2021, **5**.
16. M. A. Hegener, D. H. Hua Li, A. J. Steckl and G. M. Pauletti, *Biomedical Microdevices*, 2017, **19**.
17. J. A. Johnson and L. H. Cavallari, *Trends in Cardiovascular Medicine*, 2015, **25**, 33-41.
18. Y. Nakajima, K. Yada, K. Ogiwara, S. Furukawa, N. Shimonishi, M. Shima and K. Nogami, *Pediatrics International*, 2021, **63**, 160-167.
19. B. B. Dawood, G. C. Lowe, M. Lordkipanidzé, D. Bem, M. E. Daly, M. Makris, A. Mumford, J. T. Wilde and S. P. Watson, *Blood*, 2012, **120**, 5041-5049.
20. M. Cattaneo, C. P. M. Hayward, K. A. Moffat, M. T. Pugliano, Y. Liu and A. D. Michelson, *Journal of Thrombosis and Haemostasis*, 2009, **7**.
21. V. Vararche, C. Desconclois, T. Boutekedjiret, M. Dreyfus and V. Proulle, *Journal of Thrombosis and Haemostasis*, 2011, **9**, 1645-1647.

22. D. Sibbing, S. Schulz, S. Braun, T. Morath, J. Stegherr, J. Mehilli, A. Schömig, N. v. Beckerath and A. Kastrati, *Journal of Thrombosis and Haemostasis*, 2010, **8**, 250-256.
23. T. F. Althoff, M. Fischer, E. Langer, S. Ziemer and G. Baumann, *Thrombosis Research*, 2010, **125**, e190-e196.
24. S. B. Pedersen, E. L. Grove, H. L. Nielsen, J. Mortensen, S. D. Kristensen and A.-M. Hvas, *Platelets*, 2009, **20**, 415-420.
25. S. K. Kundu, E. J. Heilmann, R. Sio, C. Garcia, R. M. Davidson and R. A. Ostgaard, *Seminars in Thrombosis and Hemostasis*, 1995, **21**, 106-112.
26. C. E. Sing and A. Alexander-Katz, *Biophysical Journal*, 2010, **98**, L35-L37.
27. C. Krongchai, J. Jakmunee and S. Kittiwachana, *Food Analytical Methods*, 2020, **13**, 1717-1725.
28. P. Kaewarsa, M. S. Schenkel, K. L. Rahn, W. Laiwattanapaisal and C. S. Henry, *Analyst*, 2024, **149**, 2034-2044.

Chapter 5: Conclusions and Future Directions

This dissertation encompasses the development and optimization of microfluidic devices for studying physiological processes and diagnosing medical conditions. It introduces pump-driven fluidic devices for modeling the gut barrier, maintaining tissue health and morphology over 72 hours, and integrating electrochemical sensors for monitoring of molecules related to tissue health. Additionally, it details the development of several low-cost, point-of-care capillary flow microfluidic devices: one for detection of heart failure biomarkers in saliva, and two for processing whole blood. The blood capillary flow devices are for Sickle Cell Disease (SCD) phenotyping and primary hemostasis evaluation. Future directions include expanding gut barrier studies to include human tissue models, validating heart failure biomarker detection devices with clinical samples, and refining SCD phenotyping and hemostasis monitoring devices for clinical application.

5.1 Conclusions

5.1.1 Pump-Driven Fluidic Devices for Studying the Gut Barrier

The organotypic microfluidic device described in Chapter Two utilized syringe pump-driven flow to successfully preserve the health and morphology of murine colon tissue explants over 72 h. Preservation of tissue health was indicated by labeling of neurons, epithelial cells, and immune cells comparable to in vivo tissue. Importantly, the device maintained health and barrier function without inhibiting muscle contractions with nicardipine, which was previously required to keep tissue secured in the device.[1] The model in Chapter Two provides novel opportunities to examine the intestinal barrier ex vivo to better understand disease states associated with leaky gut. Collagenase, an enzyme produced by commensal bacteria within the gut included in luminal

media to affect the integrity of the gut barrier. Epithelial barrier permeability was correlated to the penetration of fluorescent molecules into the mucosa of collagenase-treated tissue. Tight junction immunoreactivity (IR) was investigated by claudin-1 labeling, and decreased IR in collagenase-treated tissue suggests increased paracellular permeability. Impact of collagenase on the extracellular matrix (ECM) stability and fragility was explored through labeling of type 1 collagen (COL-1) in the ECM. The altered structure of COL-1 in the ECM of collagenase-treated tissue demonstrated increased ECM fragility due to increased COL-1 tortuosity and decreased vertical crimping. We also closely examined goblet cells, where exposure to collagenase appeared to disrupt the natural morphology and decrease apical mucin 2 IR. Changes in shape and content of goblet cells likely affects the thickness of the mucus layer, further compromising the integrity of the intestinal barrier and its ability to protect the body from harm. We also show preliminary confirmation that we are maintaining a microbial population within the tissue in our device over 72 h.

Chapter Two also shows a comparison of the electrochemical properties of thermoplastic electrodes (TPEs) with two different binders, polycaprolactone (PCL) and polystyrene (PS). Sanded PS-based TPEs demonstrated increased electroactivity compared to the other TPEs, which was shown in voltammetry and amperometry data. The PS-based TPEs were used to detect H_2O_2 and O_2 without any electrode modification after manufacturing. The PS-based TPEs were also integrated into a reversibly sealed fluidic sensor module device in which detection of H_2O_2 demonstrated in flow. The design of the sensor module allows for simple electrode integration and assembly that can be coupled with a variety of fluidic systems such as the gut microfluidic device.

5.1.2 Capillary Flow Device for Heart Failure Prognostic Monitoring

The work described in Chapter Three has described the progression of incorporating a static electrochemical immunoassay for the detection of Heart Failure (HF) biomarkers in saliva into a capillary flow microfluidic device capable of multiplexed detection. Optimization was done on many aspects of the device, from sample volumes to channel geometry to reagent concentrations and drying conditions. Special consideration was taken to optimize flow with a viscous sample medium so the device could process saliva consistently. Optimization of the electrode array was thoroughly investigated and preliminary data with the device demonstrated minimal crosstalk between WEs. We also demonstrated the device's capability of distinguishing concentrations of two salivary HF biomarkers, Galectin-3 (Gal-3) and S100A7, in spiked buffer solutions under flow conditions. A manuscript describing this work is in preparation and will target a top tier journal in analytical chemistry (likely *Biosensors and Bioelectronics*) with me as a co-first author.

5.1.3 Low-Cost, Capillary Flow Devices for Processing Whole Blood

The two capillary-flow devices described in Chapter Four successfully processed whole blood samples without the need for complicated pre-processing or external pump systems. Initial validation of both devices has been completed with promising results. For the Sickle Cell Disease (SCD) device, we first confirmed that the calcium chloride ($CaCl_2$) and sodium metabisulfite ($Na_2S_2O_5$) reagents remain viable after being dried in reagent pads via colorimetric assays. We then demonstrated that there is a difference in migration behavior of healthy blood and plasma in control (1X PBS) vs. treatment ($CaCl_2$, $Na_2S_2O_5$) conditions. Preliminary data from collaborators showed a difference in migration behavior of healthy vs. sickle cell blood and plasma in control (1X PBS) and treatment ($CaCl_2$, $Na_2S_2O_5$) conditions. For both reagents, sickle

blood traveled more slowly and a shorter distance overall in the nitrocellulose membrane (NCM) compared to healthy blood.

For the PCAT project, we have shown extensive design evolution with various approaches to create a stenosis. Stenosis structure was tested by changing channel width and height, and by incorporating a paper pad with defined pore sizes. Impact of channel geometry, branching, venting, and reservoir configuration were all investigated to understand how blood flows in capillary flow microfluidic devices. Initial validation in our device showed we can generate fast flow for over 6 minutes with both a stenosis by height and by pore size.

5.2 Future Directions

5.2.1 The Future of Gut Barrier Studies

The results outlined in Chapter Two demonstrate that the system works to recreate the effects of a leaky gut, in terms of physiologic hallmarks such as increased epithelial permeability. While the data doesn't identify the mechanistic causes of leaky gut, it has laid a foundation for future work to expand upon to address the problem from a more causative perspective. Further experiments are necessary to understand how these changes in barrier function may lead to disease states. Current literature connects three major components behind the mechanisms of leaky gut: phenotype, barrier changes, and dysbiosis of the gut microbiome.[2] Much more data must be collected to further elucidate the microbiome within the tissue under various conditions in our device (e.g., with and without collagenase, over varying time scales, etc.). Once gene sequences are obtained they can be used to continue identifying microbes present within each sample as we have done previously.[3] Future experiments will work to investigate the effects of specific microbiome components (e.g., bacteria) that secrete collagenases, such as *Enterococcus faecalis,*[4-7] within the tissue to gain a more comprehensive

understanding of the mechanisms involved in leaky gut. In the longer run, investigations of the impact of leaky gut on colon tissue ex vivo will allow for detailed studies of neuronal and immune cell populations that could lead to a better understanding of the steps leading to problematic pathology.

Ultimately, we hope to make this system translational to humans to further understanding of intestinal disease processes. Pig intestine is similar to human intestinal tissue in size and structure, so a series of preliminary experiments were performed with pig intestine using the intestinal microfluidic device. Compared to mouse intestine, pig intestine is much thicker resulting in substantially stronger muscle contractions. Unfortunately, these contractions pulled the tissue out of our device with the current protocol. Other researchers held porcine tissue in a microfluidic device by removing the muscle layer,[8] and by removing the outermost muscle layer we were also able to keep pig intestine flat and viable for 72 h. However, this is not ideal as many enteric neurons and some immune cells reside in the muscle layers.[9-11] Long-term goals include improving the mechanisms for clamping stronger, thicker tissue within the device so that similar studies can be performed with completely intact porcine and human tissue explants. We have previously obtained human tissue explants to study,[3] so future iterations of the device could very realistically include human tissue for more translatable studies. Expansion of the data collected using the sensor module will make it more viable for use downstream of the tissue device. The unique oxygen gradient that exists in the intestinal tract in vivo is critical for nutrient absorption, barrier function, and immune responses,[12] and the microbiome plays a key role in establishing and maintaining this gradient.[12, 13] Expanding on the capability for O_2 sensing with the sensor module could provide valuable insight into the health of the tissue and maintenance of the microbiome during an experiment, before we open up the device and swab the tissue to

identify the microbiome at the end of an experiment. The proof-of-concept detecting H_2O_2 with the sensor module also shows great promise for providing critical information while an experiment is ongoing. H_2O_2 in the colon has been shown to play a causative role in the pathogenesis of ulcerative colitis, a chronic inflammatory bowel disease that is particularly challenging to treat.[14] Detection of H_2O_2 will also work towards a system for simple enzymatic detection of various biomolecules such as lactate and glucose in complex biological environments by incorporating an additional flow path with an oxidase enzyme. Results from future studies will be essential to enhance understanding of human gut health.

5.2.2 Expansion and Validation of the Heart Failure Capillary Flow Device for Use at the Point of Care

Current work to build on the capillary flow device described in Chapter Three aims to further optimize the S100A7 assay so that we can get clearer signal separation between the low and critical concentrations. A key next step is establishing the device's quantification capability in pooled saliva and addressing any complications that arise; flow study data and previous static assay calibration curves suggest that little optimization will be necessary when progressing to a saliva matrix. Long-term goals include working with our collaborators to conduct a human sample study with known HF patients' saliva. Successful correlation of the devices' results with clinical samples would vault this POC device into a marketable, usable product. This device could be distributed to clinics across the country and world, even in more resource-limited areas where residents lack access to sophisticated medical infrastructure. This device has the potential to be truly life-changing for millions of people who suffer from HF.

5.2.3 Steps Toward Validation and Expansion of Capillary Flow Devices for Sickle Cell Disease Phenotyping and Hemostasis Monitoring

Chapter Four demonstrated promising preliminary work towards a multichannel SCD phenotyping device with promising results. Next steps for this project include finishing the data analysis on the $CaCl_2$ and ADP devices that were sent to our collaborators to identify if any further changes need to be made to the design. If the results are satisfactory, we can work toward refining the multiplexed system into four different channels, each with a uniquely treated reagent pad with the optimal concentration of reagent dried onto it (1X PBS control, $CaCl_2$, $Na_2S_2O_5$, and ADP). This multiplexed system would provide a more wholistic view of a patient's SCD phenotype, so a clinician could make a well-informed decision about the most appropriate treatment approach for that individual.

Chapter Four also showed promising preliminary results for the PCAT device, and we are awaiting results from collaborators on device performance with freshly drawn blood. We have recently sent devices with both the vertical stenosis and the Whatman paper stenosis, and data pertaining to how blood containing viable platelets flows will be critical to informing future device design decisions. Initial clot visualization will be done with a naked eye or a traditional brightfield microscope. If a clot is still not able to be distinguished this way, we can alternatively use a confocal microscope and fluorescent labeling to identify and measure the location and size of the thrombus formed. One option is to use Alexa-fluor 488 fluorescently conjugated to fibrinogen,[15] and another option is to use a commercial kit such as the BD BioCoat Angiogenesis System[16] to fluorescently dye the cells to identify the thrombus location. Once we understand how the pore stenoses compare we can move forward with the most consistent and reliable design and make any necessary changes to the device itself. Our collaborator will compare the

PCAT devices using healthy blood with and without a platelet inhibitor, and we expect the uninhibited blood to form a larger thrombus faster than the inhibited blood. Long-term goals for the PCAT project involve development of a device to monitor secondary hemostasis, which occurs when the fibrinogen in a thrombus converts to fibrin and the platelet plug stabilizes.[17, 18] Current clinical tests to monitor secondary hemostasis utilize cell-free plasma and do not provide information on clot formation,[19] while assays that use whole blood require expensive equipment and trained personnel, and are not accessible to those in resource-limited communities.[20-22]

References

1. A. Richardson, L. A. Schwerdtfeger, D. Eaton, I. Mclean, C. S. Henry and S. A. Tobet, *Analytical Methods*, 2020, **12**, 297-303.
2. M. Camilleri, *Gut*, 2019, **68**, 1516-1526.
3. L. A. Schwerdtfeger, N. J. Nealon, E. P. Ryan and S. A. Tobet, *PLoS One*, 2019, **14**.
4. B. D. Shogan, N. Belogortseva, P. M. Luong, A. Zaborin, S. Lax, C. Bethel, M. Ward, J. P. Muldoon, M. Singer, G. An, K. Umanskiy, V. Konda, B. Shakhsheer, J. Luo, R. Klabbers, L. E. Hancock, J. Gilbert, O. Zaborina and J. C. Alverdy, *Science Translational Medicine*, 2015, **7**.
5. M. P. Barnett, W. C. McNabb, A. L. Cookson, S. Zhu, M. Davy, B. Knoch, K. Nones, A. J. Hodgkinson and N. C. Roy, *BMC Immunology*, 2010, **11**.
6. L. Antoni, S. Nuding, J. Wehkamp and E. F. Stange, *World Journal of Gastroenterology*, 2014, **20**, 1165-1179.
7. S. Ocvirk, I. G. Sava, I. Lengfelder, I. Lagkouvardos, N. Steck, J. H. Roh, S. Tchaptchet, Y. Bao, J. J. Hansen, J. Huebner, I. M. Carroll, B. E. Murray, R. B. Sartor and D. Haller, *PLoS Pathogens*, 2015, **11**.
8. H. E. Amirabadi, J. M. Donkers, E. Wierenga, B. Ingenhut, L. Pieters, L. Stevens, T. Donkers, J. Westerhout, R. Masereeuw, I. Bobeldijk-Pastorova, I. Nooijen and E. v. d. Steeg, *Lab on a Chip*, 2022, **22**, 326-342.
9. N. J. Spencer and H. Hu, *Nature Reviews Gastroenterology & Hepatology*, 2020, **17**, 338-351.
10. N. J. Spencer, M. Kyloh, D. A. Wattchow, A. Thomas, T. C. Sia, S. J. Brookes and S. J. Nicholas, *American Journal of Physiology-Gastrointestinal and Liver Physiology*, 2012, **302**, G34-43.
11. J. B. Furness, *Journal of the Autonomic Nervous System*, 2000, **81**, 87-96.
12. R. Singhal and Y. M. Shah, *Journal of Biological Chemistry*, 2020, **295**, 10493-10505.
13. G. P. Donaldson, S. M. Lee and S. K. Mazmanian, *Nature Reviews Microbiology*, 2017, **14**, 20-32.
14. J. Pravda, *World Journal of Gastroenterology*, 2022, **28**, 4263-4298.
15. E. T. O'Brien, M. R. Falvo, D. Millard and R. Superfine, *PNAS*, 2008, **105**, 19438-19443.
16. E. Hadjipanayi, P.-H. Kuhn, P. Moog, A.-T. Bauer, H. Kuekrek, L. Mirzoyan, A. Hummel, K. Kirchhoff, B. Salgin, S. Isenburg, U. Dornseifer, M. Ninkovic, H.-G. Machens and A. F. Schilling, *PLoS One*, 2015, **10**.
17. S. Palta, R. Saroa and A. Palta, *Indian Journal of Anaesthesia*, 2014, **58**, 515-523.
18. J. W. M. Heemskerk, E. M. Bevers and T. Lindhout, *Thrombosis and Haemostasis*, 2002, **88**, 186-193.
19. D. M. Adcock and R. C. Gosselin, *International Journal of Laboratory Hematology*, 2017, **39**, 37-40.
20. A. Wikkelsø, J. Wetterslev, A. M. Møller and A. Afshari, *Anaesthesia*, 2017, **72**, 519-531.
21. N. H. Tokuda, C. Richards, E. Lockhart and K. P. Crookston, *American Journal of Clinical Pathology*, 2018, **150**.
22. J. B. Brill, M. Brenner, J. Duchesne, D. Roberts, P. Ferrada, T. Horer, D. Kauvar, M. Khan, A. Kirkpatrick, C. Ordonez, B. Perreira, A. Priouzram and B. A. Cotton, *Shock*, 2021, **56**, 52-61.

Appendix A – Supporting Information for Chapter 2: Microfluidic organotypic device to test intestinal mucosal barrier permeability ex vivo

Figure A.1. Separation of effluents to show barrier is maintained. After modifying the device to include the Nitex mesh, preliminary experiments were conducted to verify that the barrier was still intact over time. To ensure luminal and serosal effluents were separate and that barrier integrity was maintained, preliminary experiments used luminal media containing 0.1% fluorescein (Thermo Fisher Scientific, Waltham, WA) for 50 h. The fluorescence of the effluent on both sides of the device was analyzed using a UV-Vis spectrophotometer (Thermo Fisher Scientific, Waltham, WA) set to measure absorbance at 491 nm to examine the barrier integrity at multiple time points over a ~50 h experiment. We found only the luminal effluents to have a measurable amount of absorbance, confirming that the luminal and serosal flows remained independent, and therefore the barrier was still intact.

Video A.V.1. Loading tissue into device. Shows the sequence of steps necessary to load and secure tissue in place in the microfluidic device.

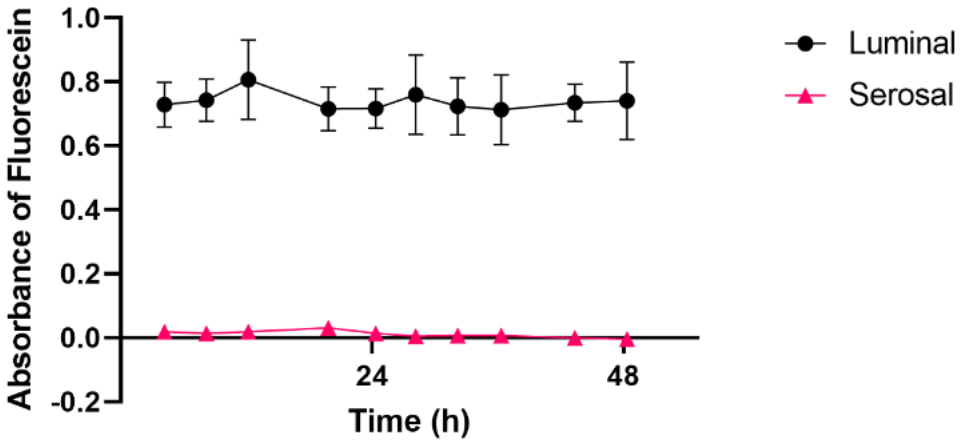

Figure A.1. Separation of effluents to show barrier is maintained. The fluorescence of the effluent on both sides of the device was analyzed using a UV-Vis spectrophotometer (Thermo Fisher Scientific, Waltham, WA) set to measure absorbance at 491 nm to examine the barrier integrity at multiple time points over a ~50 h experiment.

Video A.V.1. Loading Tissue into Device. Fileted colon tissue was placed luminal side up in the device. A 50 µm pore Nitex mesh (Genesee Scientific, San Diego, CA) was secured at the bottom of the middle layer with quick-setting epoxy (J-B Weld, Marietta, Georgia, USA) to support the tissue. The luminal side of the tissue had an additional piece of mesh glued onto it so that the full

perimeter of the tissue was securely held in place. This mesh had a 2mm diameter hole in the center to allow the media to reach the tissue that wasn't in contact with any glue.

Video A.V.1.mp4